Supercritical Water Desalination: Thermodynamic Characterization and Economic Analysis

A dissertation presented to
the faculty of
the Russ College of Engineering and Technology of Ohio University

In partial fulfillment
of the requirements for the degree
Doctor of Philosophy

Chad M. Able

August 2020

This dissertation titled

Supercritical Water Desalination: Thermodynamic Characterization and Economic Analysis

by

CHAD M. ABLE

has been approved for

the Department of Chemical and Biomolecular Engineering

and the Russ College of Engineering and Technology by

Jason P. Trembly

Professor of Mechanical Engineering

Mei Wei

Dean, Russ College of Engineering and Technology

ABSTRACT

ABLE, CHAD M., Ph.D., August 2020, Chemical Engineering

Supercritical Water Desalination: Thermodynamic Characterization and Economic Analysis

Director of Dissertation: Jason P. Trembly

The treatment of produced water (hereafter referred to as brine) from oil/gas reservoirs will prove a significant cost burden for producers; the U.S. produced 21 billion barrels of this waste in 2019 alone. Reinjection is the traditional management method; however, the availability of injection disposal is dependent on the location of the well, and is potentially unavailable when the well is remote. Average disposal costs can reach up to $\$8.00 \cdot bbl^{-1}$, with costs increasing with brine salinity. A portion of this study discusses a novel technique employed to treat high salinity brines, called supercritical water desalination (SCWD). This technique utilized favorable characteristics of water near the pseudocritical point to separate dissolved solids. Two scenarios were considered in a techno-economic analysis; one which removed all dissolved solids from the brine (termed “zero liquid discharge” (ZLD), the other concentrated brine to reduce liquid waste volume. For high salinities, this technique was shown to be economically feasible with costs ranging from \$3.49 to $\$17.28 \cdot bbl^{-1}$ in an expanded sensitivity analysis. Additionally, this study considered the thermodynamic characteristics of a binary system of $CaCl_2$-H_2O to assist in brine modeling efforts for future studies. A series of correlations were presented to describe the critical line, vapor-liquid equilibria, specific volume and enthalpy for $CaCl_2$-H_2O. The correlations were augmented by additional

specific heat data obtained at pseudocritical condition, allowing for further tuning of the specific enthalpy correlation.

DEDICATION

To my wonderful wife, Cindy

ACKNOWLEDGMENTS

To my advisor, Jason Trembly – your guidance throughout my tenure at the Institute for Sustainable Energy and the Environment (ISEE) was essential for my professional development, and you were always successful at pushing me to do better in my work. I cannot thank you enough for your support.

To my committee members, Natalie Kruse, Sumit Sharma, Marc Singer and Guy Riefler – I thank you for your constant feedback in the development of this work. I know that I asked a lot of you all, and I am very grateful for all of your feedback and constructive criticism.

To my colleague, Hamed Bateni – your assistance and feedback in the earliest stages of my graduate career was instrumental in my success. I certainly would not be where I am today without your support, and I wish you the best of luck in your future endeavors, wherever they may take you.

To my colleague, David Ogden – I am forever grateful for your assistance and patience with the development, repair and use of the desalination and calorimetric apparatus. Much of this work would not be possible without your willingness to provide feedback even after transitioning to industry.

To my colleague, Andrew Bailey – you were invaluable at performing the necessary experiments for this work, and your inventiveness and mechanical know how made very difficult and demanding experimental work more effective than it would have otherwise been. I wish you the best of luck in your final semesters at Ohio University.

To my former advisor, Paul Chan – your guidance was essential in my earliest academic efforts, and I am very grateful that you steered me towards a graduate career. I am forever in your debt, and I hope that the University of Missouri still treats you well.

To my friend, Clayton Lenhardt – I could not have made it as far as I have without your support. We have served as one another's relief valve for frustrations experienced throughout our respective careers, and I hope it has meant as much to you as it has to me. Thank you.

Last, to the rest of my fellow colleagues at ISEE – including Eli Fox, Dominic Steinberg, Michael Spencer, Akbar Saba, Dr. Sam Velraj, Dr. Wen Fan and Dr. Ravinder Garlapalli – you have provided uncountable instances of assistance to this work and to my professional development, and I will be forever grateful for my time spent at Ohio University because of you.

TABLE OF CONTENTS

Page

LIST OF TABLES

Page

LIST OF FIGURES

Page

CHAPTER 1: INTRODUCTION

Brine from U.S. oil and gas reservoirs is a significant economic and environmental burden [1], with over 21 billion barrels ($3.3 \cdot 10^9$ m^3) generated in 2019 [2]. Brine contains numerous components, including radioactive components (referred to hereafter as naturally occurring radioactive material, or NORM) and organic material, and have a high level of total dissolved solids (TDS). The components and relative concentrations in brine vary [3]. Due to high TDS, the treatment methods are limited – thus, the typical method of handling brine involves re-injection into Class II salt water disposal (SWD) wells [4], [5]. Ohio currently has over 220 Class II SWDs [6]. These Ohio SWDs process nearly 25 million barrels of produced water annually. When managed properly SWDs are safe; however, transporting produced water waste is a tremendous cost to the industry totaling $11 billion in 2013 [7]. Due to these high costs, the produced water treatment market is projected to see tremendous growth reaching $3.8 billion annually by 2025 [8].

These growing costs have driven research into treatment options to allow increased beneficial reuse of brine. However, removal of large quantities of TDS is particularly difficult; conventional methods for the removal of solids are only appropriate for water with salinities below 70,000 $mg \cdot L^{-1}$ [9]–[11], and alternative methods are both limited in scope and largely untested in an industrial setting [12]. Existing methods for brine concentration and salt production are costly to develop and energetically expensive [13], making research into alternative methods for desalination of brine necessary. Supercritical water desalination (SCWD) is an alternative desalination technique for high salinity brine remediation [1], [13]–[19]. The shift in the dielectric constant at the critical point allows for ease of separation of polar components (salts) in the brine; SCWD takes advantage of this solubility shift, allowing for the easier separation of salts from a clean water stream [1], [15], [20]. However, application of this method requires high temperatures and pressures. Additionally, the high presence of chlorides can contribute to plugging and corrosion challenges [1], [13], [15], [17].

Previous SCWD technology utilized external heating [15], [18], [21], causing scalability and plugging issues. Research at Ohio University has employed the use of direct electrical heating, called Joule-heating [17], taking advantage of brine's high electrical conductivity potentially increasing operational reliability and allowing for a much smaller vessel size, reducing capital costs associated with highly corrosion-resistant materials [1], [17]. Overall costs associated with the new Joule-heated SCWD method includes upfront pretreatment [18], [19] to remove NORM and hardness components, thermal recovery equipment, and desalination via Joule-heated SCWD. Initial economic assessments determined this method is viable, and comparable to existing methods of treatment [18]; however, these assessments did not include experimental data.

Simulation of SCWD processes [1], [15]–[17] has been previously completed using thermodynamic models for seafloor applications [22], [23]. These models were developed for a mixture of NaCl-H_2O [22]–[26] and perform well for a brine flow composed purely of NaCl. However, brine produced from wells in the Marcellus shale region [1], [3], [17] contain large amounts of divalent cations (Ca^{2+}, Ba^{2+}, Sr^{2+}, and Mg^{2+}) as well as multi-valent cations (CO_3^{2-}, SO_4^{2-}, HCO_3^{-}). These 2-1 electrolytes (two chlorides per one cation) are not easily predicted by models developed for NaCl-H_2O [1], [17]. Existing equations of state for $CaCl_2$-H_2O at high temperatures are limited to volumetric property assessments [27], [28]; thus, a series of correlations and an equation of state developed for energetics calculations would be invaluable to brine remediation research.

1.2 Objectives

Given the knowledge gaps regarding the feasibility of SCWD and overall thermodynamic data regarding hypersaline brines at these conditions, the objectives of this dissertation were as follows:

- Objective 1: Develop a new techno-economic model for SCWD via Joule-heating, using experimental data and comparing multiple methods of operation.
- Objective 2: Construct and operate a calorimeter built for hypersaline brines at high temperatures and pressures around the critical point of water, gathering new specific heat data for $CaCl_2$-H_2O at pseudocritical pressures.
- Objective 3: Use existing thermodynamic data and new specific heat data to furnish a new equation of state for $CaCl_2$-H_2O at high temperatures.

CHAPTER 2: LITERATURE REVIEW

2.1 Properties of Supercritical Water

As a pure fluid, water is a common solvent due to its abundance and polar properties. The critical point of water (that is, the point at which liquid and vapor become a single phase) occurs at 647.096 K and 22.064 MPa. As a supercritical fluid, water becomes non-polar in nature due to a shift in the dielectric constant and ion product [20]. This stark shift around the critical point is evident in Figure 1; this shift continues as pressure increases beyond the critical pressure, following the pseudocritical line [29].

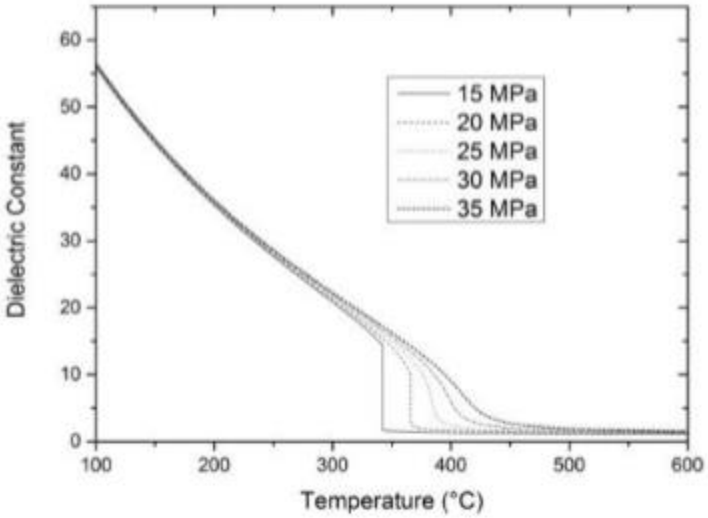

Figure 1: Dielectric constant of water near the critical point [20].

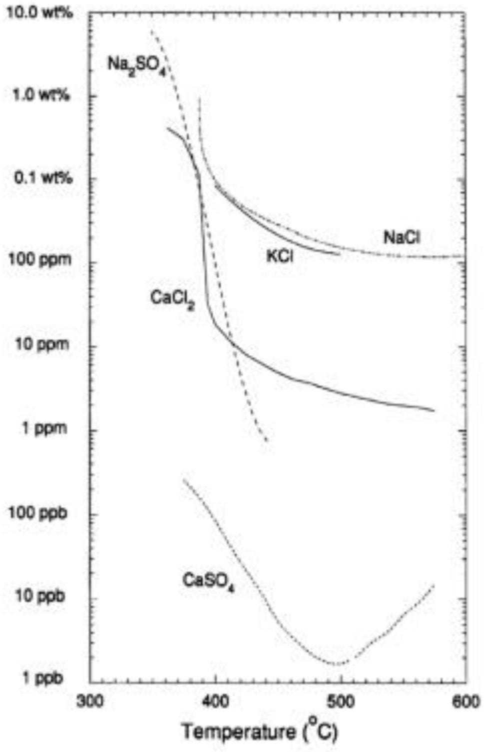

Figure 2: The solubilities of various salts in water at 25 MPa. [20]

The dielectric constant shift significantly reduces the solubility of ionic compounds such as inorganic salts, as shown in Figure 2 [20]. Given the prevalence of chloride salts in brine [3], this property may be used to generate a water product containing a low dissolved solid content from brine. The characteristics of brine are discussed in Section 2.3.

In addition, water exhibits the general properties of supercritical fluids, including a smoother density and specific heat gradient. These phenomena allow the solvent properties of water to be favorably modified via shifts in temperature and pressure beyond the critical point [29].

2.2 Properties of Brine at Supercritical Water Conditions

The critical point for a pure component can be extended into a critical line for a mixture of components, as shown for NaCl-H_2O in Figure 3 [23]. Additionally, phase diagrams for NaCl-H_2O have also been generated at temperatures near the critical point of water [23], as shown in Figure 4. Near the critical point of water, there is a narrow band of temperatures and pressures where a vapor-liquid equilibrium (VLE) envelope exists. This VLE envelope may be utilized to generate a fluid containing a low content of dissolved solids, as demonstrated in previous studies [1], [17], and a concentrated brine.

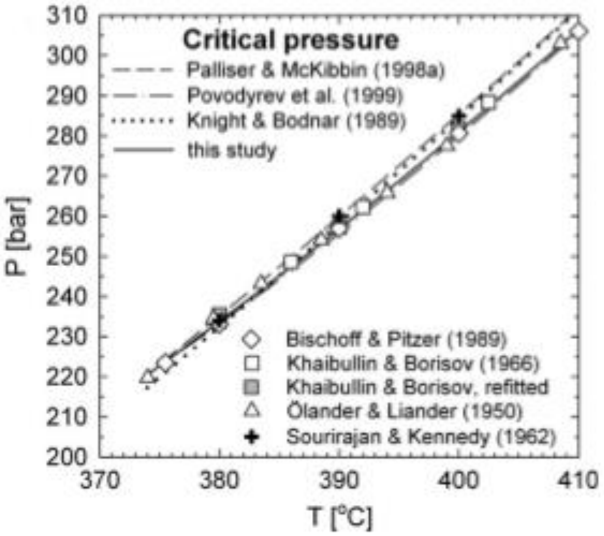

Figure 3: NaCl-H_2O critical pressure (in bar) with temperature [23].

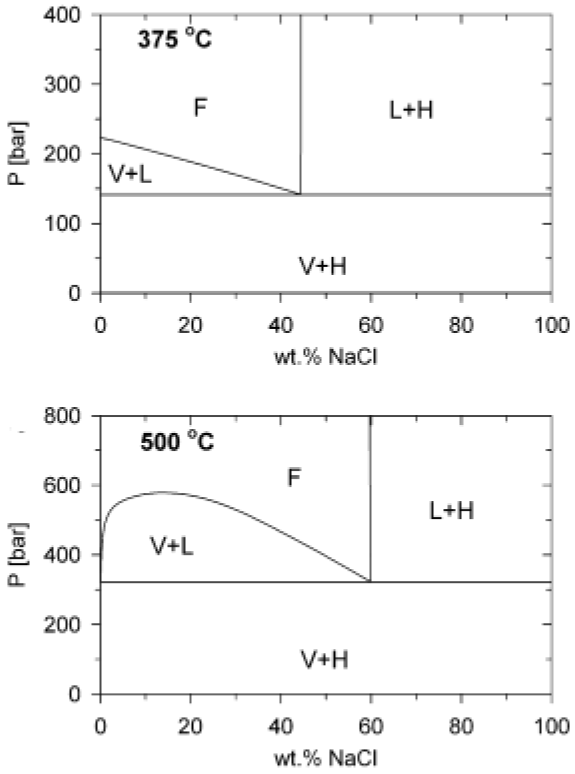

Figure 4: Phase diagrams for NaCl-H_2O at 375°C (top) and 500°C (bottom) [23]. Vapor and liquid are shown, as well as supercritical fluid (shown as F) and halite (as H).

However, thermodynamic characteristics of these brines at high temperatures and pressures are not well known. Driesner has furnished useful correlations for NaCl-H_2O [22], [23]; however, the most prominent brines from the Marcellus shale region feature large quantities of other cations in addition to sodium [1], [3]. Equations of state for single salts in water [24]–[28] are derived primarily from phase equilibrium data [30]–[34], making it difficult to assess the calorimetric properties needed for an accurate assessment of energetics [22].

The usefulness of these equations [24]–[28] and correlations [22], [23] is limited by the sparsity of data in these regions past the critical point of water. NaCl-H_2O mixtures are extremely prominent in the literature [22], [23]. However, only a few data sets exist for $CaCl_2$-H_2O at relevant thermodynamic parameters near the critical point of water. These data are summarized in Table 1.

Table 1: Summary of data on the properties of aqueous calcium chloride.

Property	**Temperature Range (°C)**	**Pressure Range (bar)**	**X (mass fraction)**	**Reference**
VLE, P_c, x_c	380-500	160-800	9 x 10^{-4} – 0.346	[34]
VLE, P_c, x_c, ρ_c	400-600	270-1325	4 x 10^{-3} – 0.447	[32], [35]
C_p	30-330	170	6 x 10^{-3} – 0.252	[36], [37]
ΔH_{dil}	300-400	107-406	9 x 10^{-4} – 3 x 10^{-3}	[38]
ΔH_{dil}, φ	170-250	72-366	9 x 10^{-4} – 0.348	[39]
ρ	25-250	70-420	3 x 10^{-2} – 0.406	[33]
ρ	25-300	100-787	2 x 10^{-3} – 2 x 10^{-2}	[40]
ρ	350-370	168-220	2 x 10^{-2} – 0.264	[41]
ρ	50-325	1-407	5 x 10^{-3} – 0.416	[42]
ρ	50-200	20	5 x 10^{-2} – 0.417	[43]
ρ, C_P	25	1	1 x 10^{-3} – 4 x 10^{-2}	[44]
ρ	10-200	10-681	0.100 – 0.400	[45]
ρ	25-90	1	0.100 – 0.513	[46]
ρ	5-35	1	0.250	[47]
ρ, ρ_s	25-125	1-594	2 x 10^{-2} – 0.400	[48]
ρ, η	25	1	2 x 10^{-3} – 0.466	[49]
ρ	10-75	1	5 x 10^{-2} – 0.217	[50]
ρ, β	5-35	1	4 x 10^{-2} – 0.453	[51]
ρ	25-45	1	5 x 10^{-2} – 0.359	[52]
ρ, μ, σ	15-55	1	6 x 10^{-2} – 0.400	[53]
ρ, C_P	24-99	1	3 x 10^{-3} – 0.100	[54]
ρ	50-200	20.3	6 x 10^{-3} – 0.100	[55]
ρ, v_s	25	1	1 x 10^{-3} – 0.100	[56]
ρ, C_P	25	1	5 x 10^{-3} – 0.418	[57]
ρ, β	25	1	4 x 10^{-3} – 0.451	[58]

Table 1 shows most data exists for densities at higher temperatures; data for specific heat and vapor-liquid equilibrium are sparse. In addition, few data exist for attributes such as compressibility (β), sound velocity (v_s), viscosity (μ), and conductivity (σ) at lower temperatures and pressures. Thus, the primary method of regressing these data sets into functioning equations of state is to use density data at high temperature conditions [27], [28]. Similar to Anderko's Helmholtz energy formalism [25], these equations of state are derived in the Helmholtz energy term first. Gibbs energy formalisms are readily available for lower temperature and pressure conditions [59]; however, at higher temperatures a Gibbs formalism fails to capture very low dilutions due to critically divergent behavior for the pure solvent [60]. Briefly, they are generally of the form:

$$a^{res} = a - a^{ig},$$

where *res* denotes a residual (or excess) quantity and *ig* denotes a corresponding ideal gas quantity. These models treat electrolytes as fully associated [25]–[28]; implying the ions readily form ion pairs and clusters rather than remaining disassociated, a consequence of the rapidly declining dielectric constant [20]. For NaCl, other associated approaches have been shown to be successful for low concentration behavior [61], [62]; however, no such equations exist for $CaCl_2$. More recent equations [63] have modeled a solid phase in conjunction with VLE for NaCl by utilizing Driesner correlations [22], [23]. However, these correlations and corresponding equations of state are also missing for $CaCl_2$-H_2O.

2.3 Characteristics of Brine and the Economics of Treatment Methods

The salinity and composition of brine is mainly dependent on the source (i.e. reservoir) and to some extent type of extraction methodology employed [3]. Figure 5 presents the salinity ranges for brines generated by oil/gas wells. Table 2 shows the cationic and anionic breakdown of unconventional brines, given their prominence in discussion around natural gas resources in the greater Ohio area. Although the cations have the largest variance, the most prominent anion is chloride [1], [3].

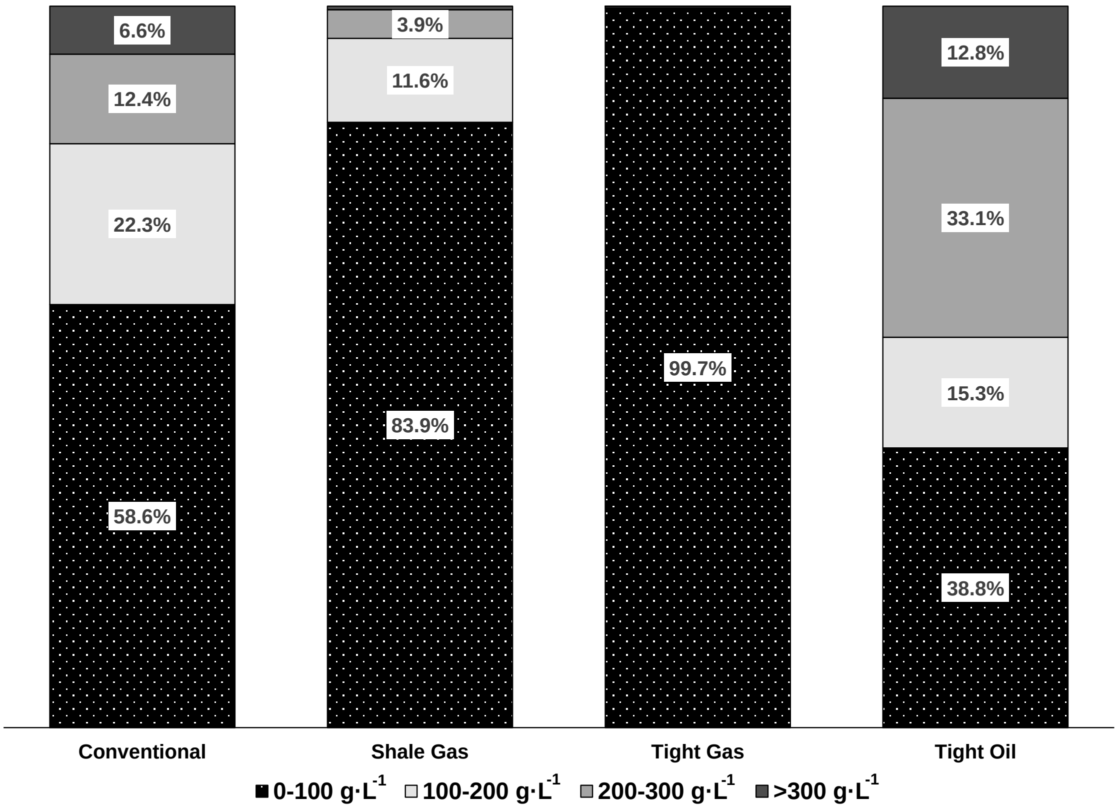

Figure 5: Salinity ranges for different sources of brine [1], [3].

Table 2: Aqueous ions present in brine generated by unconventional gas reservoirs [1], [3].

Cations				
Na^+	13.1	-	117,000	$mg \cdot L^{-1}$
Ca^{2+}	1.95	-	162,324	$mg \cdot L^{-1}$
Mg^{2+}	0.1	-	5,560	$mg \cdot L^{-1}$
K^+	0.07	-	4,080	$mg \cdot L^{-1}$
Ba^{2+}	0.05	-	22,400	$mg \cdot L^{-1}$
Sr^{2+}	0.07	-	15,400	$mg \cdot L^{-1}$
Anions				
Cl^-	1	-	196,000	$mg \cdot L^{-1}$
SO_4^{2-}	0.1	-	3,580	$mg \cdot L^{-1}$
HCO_3^-	0.01	-	13,880	$mg \cdot L^{-1}$

Due to varying salinities, methods for effective treatment of brine are also varied. For very low salinities (less than or equal to that of seawater, 35 $g \cdot L^{-1}$) the most appropriate method for brine concentration is reverse osmosis (RO), due to the very low energetic requirements [9]–[11], [64]; only pressure is needed and multiple passes can be used to concentrate the brine to approximately 70 $g \cdot L^{-1}$. However, at this stage the treatment options become more limited. Mechanical vapor compression [12], [65], multi-stage flash [13], [66] and multi-effect distillation [13] are all potentially viable thermal technologies for further concentration of brine. However, none of these techniques are ZLD-capable. Furthermore, the large vessel sizes and multiple stages needed for effective brine concentration limit the economic viability of these techniques [13]. Experimental validation of these methods is also limited. A comparison of alternative desalination technologies and the highest validated salinity for each technique is shown in Table 3.

Table 3**:** A comparison of various desalination techniques in terms of energetics and experimentally validated and projected salinities.

Technology	Specific Energy Input (kWh/m^3)			Highest Salinity (g·L^{-1})	Maximum Projected Salinity (g·L^{-1})	ZLD Potential
	Electrical	Thermal	Total			
Mechanical Vapor Compression (MVC)	13.6-32.1	0-671.0	13.6-700.0	55	200	No
Multi-Effect Distillation (MED)	2.0-4.0	30.0-200.0	34.0-204.0	35	200	No
Multi-Stage Flash (MSF)	2.5-5.0	15.8-23.5	19.6-27.3	35	200	No
Membrane Distillation (MD)	0	49.6-680.0	49.6-680.0	35	180	No
Forward Osmosis (FO)	5.0-8.0	275.0-600.0	283.0-605.0	73	350	No

Although projected salinities are quite high [12], experimentally validated salinities for these technologies are roughly that of seawater. Forward osmosis (FO) has potential as a high-salinity membrane technique, but it requires a sacrificial draw stream that requires additional treatment [67]. Membrane distillation (MD) has shown some potential with 180 g·L^{-1} flows in the case of air-gap membrane distillation [68]. However, the flow rate is limited and the potential for fouling increases dramatically with salinity and in the presence of organics.

ZLD–capable techniques are more limited. Evaporation ponds are a useful and inexpensive method for leaving no liquid waste [13]. However, this technology fails to recover the clean water and requires a large area of land. In addition, the solid sludge that remains must be treated in order to reuse the pond. The most commonly used available technology for high salinity brine is a crystallizer [69]; this process requires multiple stages with vacuum pressures and becomes much more energetically expensive to perform ZLD versus a concentrated brine product.

This work investigates SCWD [1], [13]–[19] as experimental work has demonstrated this technique is capable of treating water containing up to 180 $g \cdot L^{-1}$ [17]; in addition, the use of high temperatures and pressures allow a downstream flash vessel to further concentrate the brine to ZLD conditions [1]. However, corrosion resistant materials are required to withstand these high temperatures and pressures. With external heating methods, the required vessel sizes are too large to be economically feasible [13], [15], [17]. The Joule-heating technique proposed and validated by Ohio University (as shown in Figure 6) [1], [17] takes advantage of the inherent conductivity of brine, allowing for direct internal heating via an electrode inside of the desalination vessel. This technique allows for much smaller vessel sizes, even for large flow rates [17]. By reducing the size of the vessel, this process may allow for economically feasible treatment of a variety of brines. Previous economic models have demonstrated this outcome [18], [19] but did not account for a specific method or include experimental data.

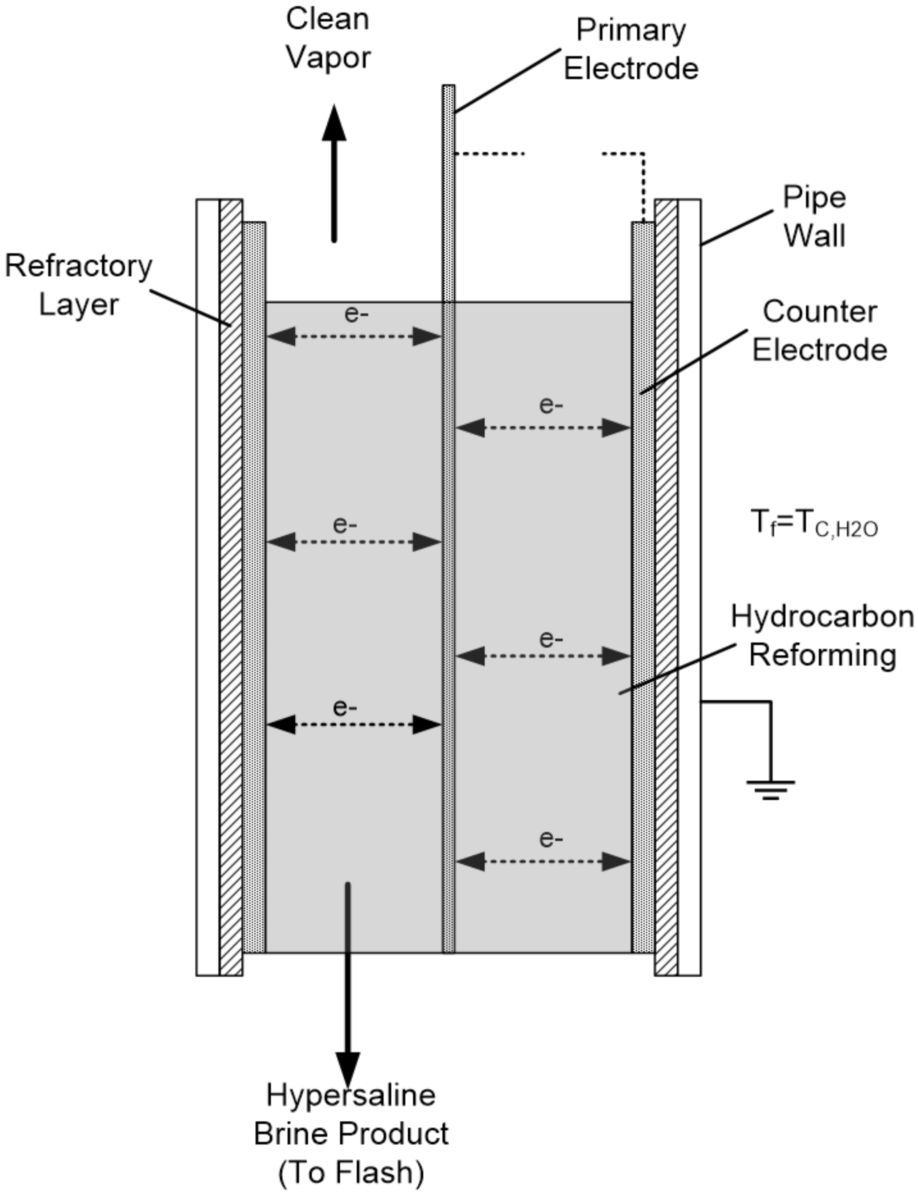

Figure 6: The Joule-heating desalination process for supercritical water desalination.

2.4 Calorimetric Methods for Specific Heat Determination of High-Temperature Brines

For the data in Section 2.2, the caloric data fall under two general categories: heat of dilution [38], [39], [70], [71] and specific heat [36], [37], [72]–[74]. Heat of dilution data [38], [39], [70], [71] are gathered using a flow calorimeter at isothermal conditions by mixing a high-concentration stock solution with water to generate the desired concentration. The heat difference (in this case, heat lost) produces the enthalpy of dilution; that is, a heat generated or lost by a shift in concentration at constant T and P. By collecting data at different temperatures at constant pressure, specific heat data can also be determined by drawing tie lines between the enthalpy differences at these temperatures. However, calculating specific heat data [36], [37] in this manner can lead to large errors, even with small errors in heats of dilution.

Another method involving flow calorimetry [37], [42], [72]–[74] modulates the temperature between two points of measurement with constant pressure and concentration to directly calculate specific heat. Because of the difference in temperature, the Cp is at an average temperature between the two points. This leads to a somewhat lower accuracy than that of the previously discussed heat of dilution data, but can be used to directly calculate enthalpy's dependence on temperature. Maintaining a temperature differential of around 2-4 K is appropriate [73]. Estimation of heat losses using this method is necessary for accurate measurement of heat capacity data, as discussed further in Appendix G.

CHAPTER 3: METHODOLOGIES

3.1 Aspen Process Model

The SCWD process was simulated with Aspen Plus v.10 (Aspen Technologies) software using the electrolyte non-random two liquid (ELECNRTL) model to estimate fluid thermodynamic properties. Aspen Plus is a robust modeling software for a variety of process components; however, due to the specialized equipment used in this system, a variety of vendor quotes were also used in cost estimation [75]. Aspen's ELECNRTL model is valid for mixed electrolytes at any concentration; this model does possess a high degree of error near water's critical point [18]. The Aspen simulation was used to estimate material and energy balances for the process, except for the desalinator which was supplemented with operational data made available by Ogden [17]. Desalinator power requirements were simulated based upon prior experimental results using FORTRAN code in a user-defined operation block [1], [17]. The specific water recovery was a user-defined input which defined the ratio of vapor to liquid mass flow rate driven by desalinator power consumption. In addition, simulation stream temperatures exiting the desalinator (estimated by ELECNRTL) were corrected based on experimental data [17].

The inlet brine salinity of 176.3 $g \cdot L^{-1}$ was selected based upon previous prototype testing with field-derived brine from the Utica Shale [1]. Details of the brine composition are provided in Table 4. Additional compositions are provided which are used in a sensitivity analysis. The presence of divalent cations in the default brine were expected to escalate treatment cost associated with additional chemical pretreatment. Thus, three compositions were considered which reduced the impact of key divalent ions; Composition A excluded Sr^{2+}, Composition B excluded Mg^{2+} and Composition C had a higher Na^+ content weighting, thereby reducing the concentration of all other ions. All three compositions were normalized to contain identical TDS levels; this is also shown in Table 4.

Table 4: The default brine salinity used in the Aspen process model and alternative salinities considered.

Constituent Salt ($mg \cdot L^{-1}$)	Default Concentration	Comp. A	Comp. B	Comp. C
Na^+	35,115	35,847	37,896	52,673
Sr^{2+}	1,988	0	2,145	968
Ca^{2+}	25,167	25.692	27,160	12,260
K^+	421	430	454	205
Mg^{2+}	3302	3,371	0	1,609
Cl^-	110,298	110,953	108,636	108,577
Total	176,292	176,292	176,292	176,292

Process flow diagrams for both cases are shown in Figure 7. Prior to chemical treatment, sand filtration and UV systems were used to remove suspended solids and bacteria; this was not modeled in Aspen. This work is described in prior work from Ohio University [75], [76]. A combination of mixing tanks and hydrocyclones were used for chemical precipitation in both the ZLD and brine concentration cases; in the ZLD case, three tanks/hydrocyclones were necessary to remove strontium (as $SrSO_4$), magnesium (as $Mg(OH)_2$) and calcium (as $CaCO_3$) before treatment in the desalinator. This was to avoid equipment scaling [18], [19] or generation of a hazardous bulk salt product [18]. The water chemistry for the three reactions are as given [75], [76]:

$$\mathrm{Sr^{2+}(aq) + SO_4^{2-}(aq) \leftrightarrow SrSO_4(s)} \quad (1)$$

$$\mathrm{Mg^{2+}(aq) + 2OH^-\ (aq) \leftrightarrow Mg(OH)_2(s)} \quad (2)$$

$$\mathrm{Ca^{2+}(aq) + CO_3^{2-}(aq) \leftrightarrow CaCO_3\ (s)} \quad (3)$$

Due to the low carbonate and sulfate content found in Utica Shale brines, upfront removal of these scaling cations was not considered. However, such pre-treatments would need to be considered for treatment of brine generated by other reservoirs.

In the brine concentration case, only magnesium was removed (as $Mg(OH)_2$) to meet drilling fluid standards [77], [78]. NORM removal was considered in the ZLD case, to avoid radioactive material in the final salt product. The NORM removal unit reduced the radioactive concentration in the brine (measured in picocuries per liter, or $pCi \cdot L^{-1}$) [79]. The waste products discussed here were given additional attention in Appendix A. A high pressure pump was used to increase fluid pressure between 230 and 280 bar; a single heat exchanger was used in the ZLD case, whereas two heat exchangers were used for heat recovery in the brine concentration case. All high temperature equipment (heat exchangers, desalinator and flash vessels) were crafted from Hastelloy C-276 alloy for corrosion protection; this has been shown to be successful in experiments [1], [17] as well as in isolated corrosion tests [80]. No other materials were considered for the high temperature components, as stainless and carbon steel are not suitable in this corrosive environment. The preheater and flash vessel blocks were used in tandem to estimate energy requirements for the desalinator electrode; the flash vessel was used to estimate recovery ratios, while the aforementioned FORTRAN code was used to account for brine heat of vaporization [17]. The liquid effluent was charged to an additional heat exchanger to recover thermal energy in the brine concentration case; in the ZLD case, two flash vessels in series (operating at 10 and 1 bar, respectively) were used to remove the remaining water to generate solid salt [1], [15]. In the ZLD case, all vapor streams (desalinator plus downstream flash vessels) were mixed before entering the cooling water heat exchanger (labeled COOL in Figure 7); this heat exchanger was solely used to liquefy the desalinator vapor outlet in the brine concentration case.

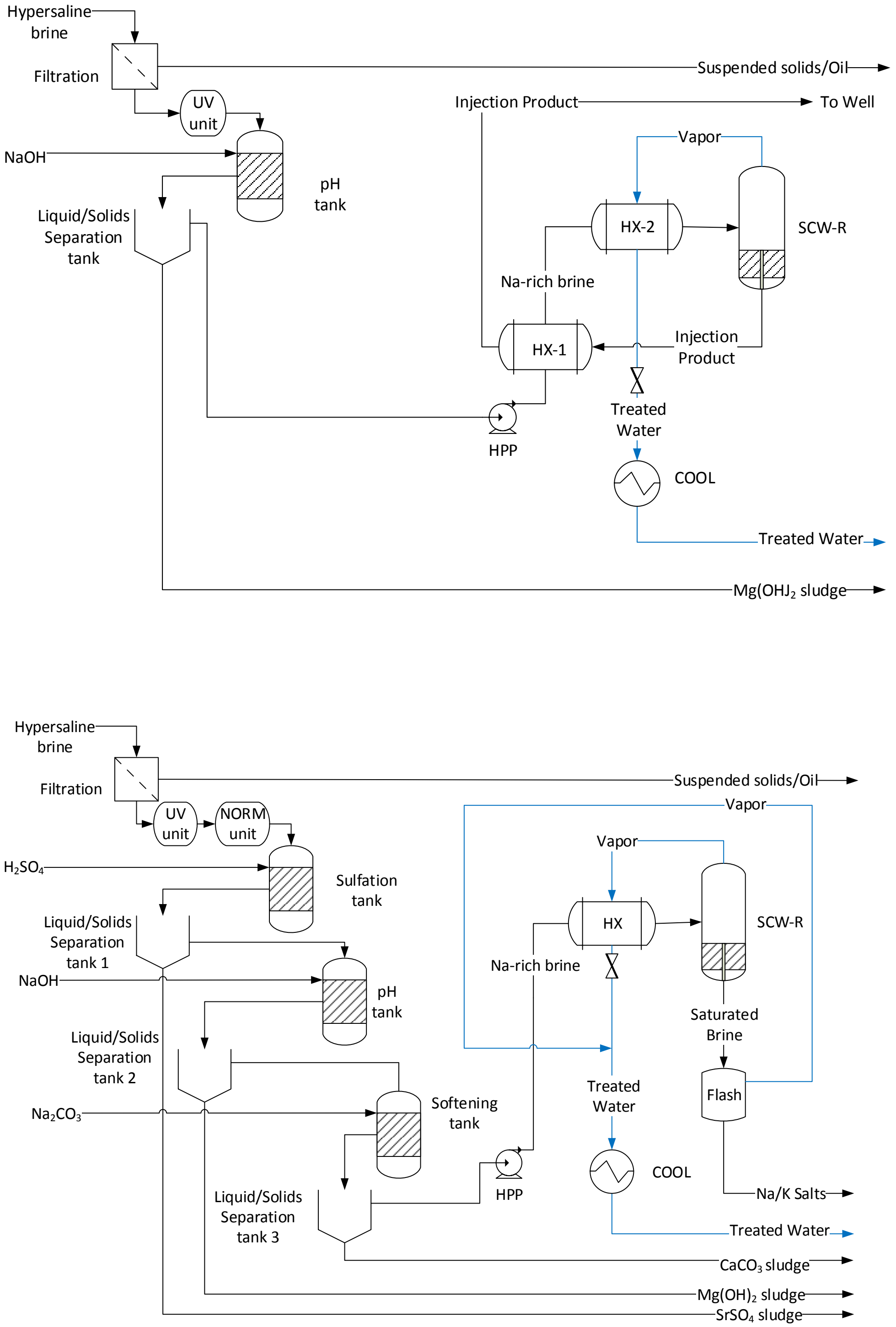

Figure 7**:** Process flow diagrams of the simulation used to estimate desalination process variables for brine concentration (above) and ZLD (below).

3.2 Cost Analysis

Two costing scenarios were considered for each operating scenario in this study. In the brine concentration case, brine product was sold as ten-pound brine for drilling operations as an alternative to well re-injection [77]. In the ZLD case, the chloride product was sold as rock salt [81], [82] as an alternative to disposing the chlorides as non-hazardous waste [75].

The results of the Aspen process model for the SCWD process were subsequently analyzed from a cost perspective using a combination of methods outlined by Turton [83] and vendor quotes for specialized equipment [18], [75], corrected to 2018 dollars using the Chemical Engineering Plant Cost Index [84]. A process treatment cost ($\$\cdot bbl^{-1}$) was developed to be used in comparison with other desalination techniques as well as for economic optimization. The treatment cost consisted of both capital (equipment) and operating (utilities, raw materials, waste disposal and labor) costs. Parameters used in the study are provided in Table 5 and explained subsequently.

Table 5: Default values and sensitivity ranges used in SCWD process cost analyses.

Variable	Default	Range	Units	Source
Salinity	176.3	75-270	$g\cdot L^{-1}$	[1]
Pressure	250	230-280	bar	[17]
Recovery Ratio (per mass)	0.5	0.4-0.8	-	
Cost of re-injection	-	0.5-2.5	$\$\cdot bbl^{-1}$	[85]
Electrolysis Losses	44	0-44%	%	[17]
Flow Rate	100	10-500	gpm	
Power Source	Natural Gas	WV, US Average	-	[18], [86]
Cost of NG	3.0	-	$\$\cdot MMBtu^{-1}$	[87]
NG Efficiency	30	-	%	[18]

Table 5 Continued

Hazardous Waste Cost	250	0-2,000	$\$\cdot ton^{-1}$	[18]
Non-Hazardous Waste Cost	33	0-100	$\$\cdot ton^{-1}$	[18]
Cooling water	0.354	-	$\$\cdot GJ^{-1}$	[19], [83]
NORM in feed	5,000	0-10,000	$pCi\cdot L^{-1}$	[79]
Equipment Lifetime	9.5	-	Years	
Capacity Factor	0.9	-		
Interest Rate	5%	-	yr^{-1}	
Transportation costs for brine	0	0-20	$\$\cdot bbl^{-1}$	
Ion Removal	Sr, Mg, Ca	Sr, Mg (keep Ca)	-	
Brine sale price	2.15	-	$\$\cdot bbl^{-1}$	[77], [88]
Rock salt sale price	72.24	-	$\$\cdot ton^{-1}$	[89], [90]
Cost of Materials				
H_2SO_4	110	55-220	$\$\cdot ton^{-1}$	[91]
NaOH	640	320-1280	$\$\cdot ton^{-1}$	[92]
Na_2CO_3	222	111-444	$\$\cdot ton^{-1}$	[93]
Clinoptilolite	108	-	$\$\cdot ton^{-1}$	[18]

The pressure of 250 bar was the midrange pressure used in prior experiments [1], [17]. Other pressures evaluated experimentally were 230 and 280 bar; this was considered in the sensitivity analysis below.

The recovery ratio was determined on a per mass basis per Equation 4 – this was for ease of use in future calculations as well as a reference for prior data [1], [17]. Here, $\dot{m}_v$ was the mass flow rate of the vapor and $\dot{m}_i$ was the mass flow rate of the inlet to the desalinator block.

$$\text{Water Recovery } (per\ mass) = \frac{\dot{m}_v}{\dot{m}_i} \tag{4}$$

Equipment costs were estimated using methods outlined in Turton [83] or estimated vendor quotes from 2014 [75] corrected to 2018 values [84]. Capital cost was subsequently annualized at a 5% interest rate with a 9.5 year equipment lifetime. The electrolysis losses (defined as “electrochemical power loss” in the experimental data [17]) were calculated based on low- and high-voltage tests in the desalination system, and were used to explain the large discrepancy in the experimental data vs. the theoretical limitations. Because of the voltages employed in the system (8 VAC), it was expected that some electrolysis will occur due to the high voltages, temperatures and overall conductivity of the fluid. However, it was noted no gaseous products (H_2, O_2) have been detected during any experiments. Based on the existing supercritical water desalination design, the energetic losses from electrolysis were expected to be 44% [17] at an operating voltage of 8 VAC; electrolysis losses decreased at lower applied voltages but also required varying reactor volumes. These factors were explored in the sensitivity analyses.

The costs of labor were provided using the Bureau of Labor Statistics for wastewater treatment operators in the Parkersburg-West Virginia area [94] as of May 2018. It was assumed this process will require two operators for continuous operation (ten total operators for 24-hour operation).

Raw materials costs were gathered from various industry sources for sulfuric acid [91], sodium hydroxide [92], and sodium carbonate [93]; these values were from 2018-2019 and were used as is. In addition, clinoptilolite zeolite was necessary for the removal of NORM; wholesale prices for this zeolite were gathered from Zhao and industry sources [95], [96] for a cost per ton of zeolite.

Disposal costs for various product streams were dependent upon composition. Sulfate precipitates generated in the ZLD case, for example, were assumed to be hazardous waste, as was the spent zeolite used for NORM removal (in both cases). Chloride and hydroxide salts were assumed to be non-hazardous in the ZLD case. The sodium and potassium chloride salt produced at the end of the ZLD case was alternatively considered as a revenue generating product to assess economic outputs based upon current rock salt pricing [89], [90]. For convenience, these products are tabulated in the supplementary information in Appendix A. The estimates for the disposal of hazardous and non-hazardous waste were considered in prior techno-economic analyses on this front [18]; $250 per ton was used for the disposal of hazardous waste, while $33 per ton was used for the disposal of non-hazardous waste.

Utility costs were estimated using a mobile natural gas generator from a vendor quote from prior work [75] scaled to 2018 values [84]. The spot price of natural gas was used to calculate utility costs (around $3 per MMBtu [87]) and a 30% conversion efficiency (converting natural gas into electrical power) was used. Industrial electrical sources existed as an alternative to using a natural gas generator for this process; however, the remote nature of fracturing wells coupled with current low natural gas pricing made this a reasonable option. Cooling water was used to condense vapor from the desalinator unit; these costs were roughly estimated from Turton [83].

Sensitivity ranges in Table 5 were selected based on available information for specific variables that may impact the overall brine remediation cost. For example, a salinity range of 75 to 270 $g \cdot L^{-1}$ was assessed to reflect brine composition [97] and operating pressure was varied from 230 to 280 bar based on prior experimental data [17]. For other sensitivity analyses, the high and low values were chosen vs. the base case.

3.3 Computational Methods

Correlations developed in this study were regressed using the numpy, scipy, lmfit and iapws packages freely available in the Python language [98]–[100]. Constraints and weighting of data were selectively used to ensure the correlations accurately depict low concentration data. The chi-square values were used in conjunction with manual analysis for sensible correlations to determine the appropriate fit. For larger data sets, computations for deriving the density and enthalpy correlations were completed with the aid of the Ohio Supercomputer [101]. Literature property data for H_2O-$CaCl_2$ are shown in Table 6. These data sets were then used in the regression of phase behavior and thermodynamic variables in the subsequent correlations.

Table 6: Literature property data examined for use in equation fitting.

Property	**Temperature Range (°C)**	**Pressure Range (bar)**	**x (mass fraction, $CaCl_2$)**	**Reference**
VLE, P_c, x_c	380-500	160-800	9×10^{-4} – 0.346	[34]
VLE, P_c, x_c, ρ_c	400-600	270-1325	4×10^{-3} – 0.447	[32], [35]
C_p	30-330	170	6×10^{-3} – 0.252	[36], [37]
ΔH_{dil}	300-400	107-406	9×10^{-4} – 3×10^{-3}	[38]
ΔH_{dil}, φ	170-250	72-366	9×10^{-4} – 0.348	[39]
ρ	25-250	70-420	3×10^{-2} – 0.406	[33]

Table 6 Continued

ρ	25-300	100-787	2 x 10^{-3} – 2 x 10^{-2}	[40]
ρ	350-370	168-220	2 x 10^{-2} – 0.264	[41]
ρ	50-325	1-407	5 x 10^{-3} – 0.416	[42]
ρ	50-200	20	5 x 10^{-2} – 0.417	[43]
$\rho^{\dagger}$, C_P	25	1	1 x 10^{-3} – 4 x 10^{-2}	[44]
ρ	10-200	10-681	0.100 – 0.400	[45]
$\rho^{\dagger}$	25-90	1	0.100 – 0.513	[46]
$\rho^{\dagger}$	5-35	1	0.250	[47]
ρ, ρ_s	25-125	1-594	2 x 10^{-2} – 0.400	[48]
$\rho^{\dagger}$, η	25	1	2 x 10^{-3} – 0.466	[49]
$\rho^{\dagger}$	10-75	1	5 x 10^{-2} – 0.217	[50]
$\rho^{\dagger}$, $\beta^{\dagger}$	5-35	1	4 x 10^{-2} – 0.453	[51]
$\rho^{\dagger}$	25-45	1	5 x 10^{-2} – 0.359	[52]
ρ, μ, σ	15-55	1	6 x 10^{-2} – 0.400	[53]
ρ, C_P	24-99	1	3 x 10^{-3} – 0.100	[54]
ρ	50-200	20.3	6 x 10^{-3} – 0.100	[55]
$\rho^{\dagger}$, $v_s^{\dagger}$	25	1	1 x 10^{-3} – 0.100	[56]
$\rho^{\dagger}$, C_P	25	1	5 x 10^{-3} – 0.418	[57]
$\rho^{\dagger}$, $\beta^{\dagger}$	25	1	4 x 10^{-3} – 0.451	[58]

†Denotes data not used in regression analyses.

3.4 Experimental Methods

The calorimeter used in this study consisted of a modified desalination system used for prior tests with both synthetic [17] and field-derived [1] brine. A process flow diagram (PFD) for the calorimeter system is shown in Figure 8. Liquid is charged to the system using a ChromTech HF-300 high flow dual piston pump with maximum flow rate and pressure of 300 mL·min^{-1} and 585 bar, and accuracy of 5% of set point. Solution flow rate was determined using a Mettler Toledo Precision Balance XS6002S (±0.01 g) at the liquid sampling point and recording liquid effluent mass over time using a data acquisition system. The solution was charged through a heat exchanger (HX-101) to recover energy from the liquid outlet before entering the preheater. A pre-heater (HX-103) in conjunction with a heat tape (HX-104) was used to achieve the desired fluid inlet temperature (TC 503-504). The calorimetric section itself was comprised of two Type E thermocouples (OMEGA Engineering) and a nichrome coil heating element (QCS Automation) for negligible resistance changes with temperature. Power to the coil heating element was controlled using a variable transformer (Staco Energy model 6020CT, 0-280 VAC output). The thermocouples were calibrated by an independent laboratory (ThermoWorks, Inc.) between 250-450 °C. Following the calorimeter section, the solution was cooled through the effluent heat exchanger and then with cooling water (HX-105). Fluid pressure was monitored prior to cooling and was controlled using a back-pressure control valve (RCV, labeled as BPR-101). A PID controller was used to maintain system pressure to within ±2 bar. All trials were conducted at a flow rate of 150 mL/min; the pressure in each trial varied between 200 and 260 bar. Extensive trials were completed using DI water to determine system heat loss. In addition, DI water was charged through the system to determine heat loss with pure water enthalpies from literature [102]. All relevant process information (voltage, amperage, temperature, pressure, mass flow rate) was recorded using a National Instruments cRIO and monitored with LabVIEW software designed for the calorimeter. The instrumentation limits of heating components were compiled in conjunction with their variances to give an expanded uncertainty for the specific heat in the following sections; this is discussed in greater detail in Appendix G. Prior to tests conducted with $CaCl_2$-H_2O, a collection of results were first collected with NaCl-H_2O for calibration purposes; these results are shown and discussed briefly in Appendix G.

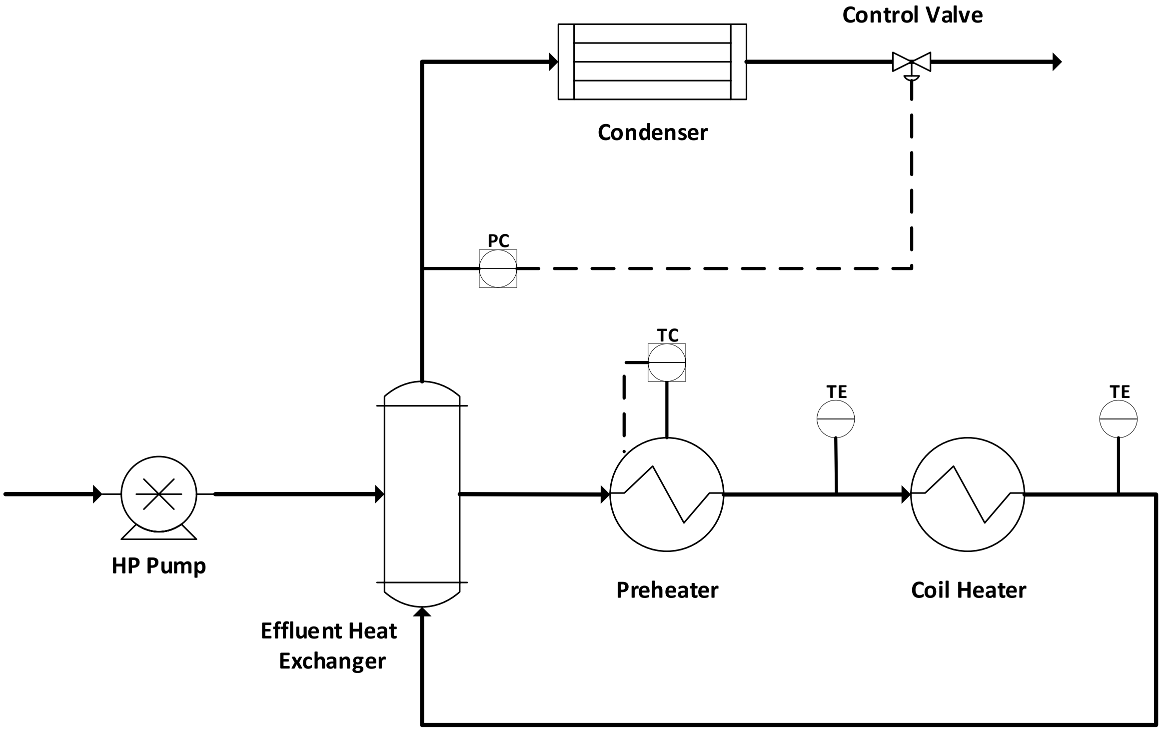

Figure 8: Calorimeter Piping & Instrumentation Diagram (P&ID). The temperature controllers (TCs), pressure controllers (PCs), and temperature measuring elements (TEs) are shown.

CHAPTER 4: ADVANCED SUPERCRITICAL WATER-BASED PROCESS CONCEPTS FOR TREATMENT AND BENEFICIAL REUSE OF BRINE IN OIL/GAS PRODUCTION

Information presented in this chapter appears in Desalination, Volume 481, Pg. 114334.

4.1 Introduction

Techno-economic analyses have been completed for supercritical water desalination to estimate the affiliated treatment cost [18], [19]; these analyses concluded the technique was similar in cost to existing brine management methods, including injection disposal with associated transportation [18], but were conducted without experimental validation. This study reconciled these differences with a simulation based upon reported experimental results from a prototype Joule-heated desalination system [1], [17], treating brine at the supercritical condition. Beyond this point, water's dielectric constant shifts, allowing for creation of a non-polar phase within the desalinator vessel [20]. This permitted the production of a low TDS vapor, the density of which was modulated by the operating pressure [17]. Two brine treatment scenarios were considered in this study. In the first case, brine was minimally pretreated followed by SCWD to generate clean water and a concentrated brine solution which may be reused as a drilling fluid [77]. In the second case, substantial pretreatment was added to remove problematic components (Ba^{2+}, Sr^{2+}, NORM, etc.), before SCWD generated a clean water and solid salt product, hereafter referred to as zero liquid discharge (ZLD). Sensitivity analyses were also conducted to determine the impact of salinity and water recovery on desalination system costs, as well as other factors, such as capacity, consumables, electrode efficiency and dissolved solid concentrations.

4.2 Results and Discussion

Operating cases considering treatment cost per barrel for 100 GPM waste throughput are shown in Table 7. In the ZLD cases, rock salt was generated and disposed via landfill or sold, resulting in nearly full recovery of water entering the system. In the brine generation cases, a ten-pound brine was generated and disposed via reinjection or sold, resulting in limited solids generation and lower volume of clean water product. Capital costs for the brine concentration cases were marginally greater than the ZLD cases (11.4%) due to the additional heat recovery equipment. Capital costs associated with additional hydrocyclones and separators required for ZLD operation were limited in comparison to the additional heat exchanger necessary for brine concentration. Brine concentration treatment costs were lower in comparison to the respective ZLD disposal (37.5%) and sales cases (31.1%). The lowest overall treatment cost was found for the brine concentration sales case ($4.75); although the utilities costs are comparable (contributing $\$2.46 \cdot \text{bbl}^{-1}$ in the ZLD case and $\$2.59 \cdot \text{bbl}^{-1}$ in the brine concentration case), the disposal and raw materials cost of the ZLD case was substantially larger than the brine concentration case, contributing an additional $\$5.31 \cdot \text{bbl}^{-1}$ for ZLD vs. only $\$1.14 \cdot \text{bbl}^{-1}$ for brine concentration. Itemized cost breakdowns of each individual component have been reported for previous techno-economic analyses of supercritical water treatment of brine [18], [19]; these itemizations for each capital and operating component for the default cases reported here are provided in Appendix B.

Table 7: Default ZLD and brine concentration cases considered, including capital costs, mineral product and cost per barrel.

	ZLD (Disposal)	**ZLD (Sales)**	**Brine Concentration (Disposal)**	**Brine Concentration (Sales)**
Brine Inlet Flow (GPM)	100	100	100	100
Capital Cost ($M)	3.1	3.2	3.5	3.5
Mineral Product (tons·day^{-1})	134.2	134.2	4.1	4.1
NORM (tons·day^{-1})	1.8	1.8	0	0
Sulfates (tons·day^{-1})	2.0	2.0	0	0
Hydroxides (tons·day^{-1})	3.2	3.2	4.1	4.1
Carbonates (tons·day^{-1})	31.9	31.9	0	0
Chlorides (tons·day^{-1})	95.3	95.3	0	0
Clean Water Product (GPM)	92.3	92.3	51.8	51.8
Brine Product (GPM)	0	0	48.3	48.3
Treatment Cost ($·bbl^{-1})	10.19	6.89	6.37	4.75

A detailed cost breakdown for the ZLD (solids disposal) and brine concentration (re-injection) cases are provided in Figure 9. The predominant cost for ZLD was the cost of raw materials (sodium carbonate, sodium hydroxide, sulfuric acid and clinoptilolite); these became dominant when significant pretreatment was needed to generate a reusable chloride product, accounting for \$3.78·bbl^{-1}. The cost of solids waste disposal was also large in this case. The resultant NORM and strontium sulfates were hazardous material; in spite of their relatively low production (a combined 3.8 tons per day), their disposal costs still contributed approximately \$0.28·bbl^{-1}. Additionally, large amounts of calcium carbonate (31.9 tons per day) and sodium and potassium chloride (95.3 tons per day) were generated, substantially increasing solids waste disposal (\$0.90·bbl^{-1}). With hydroxides included, non-hazardous waste produced via ZLD totaled around 130.4 tons per day, dwarfing the combined 3.8 tons per day of hazardous material. Utilities costs were dominant in the brine concentration case, due to lower pretreatment requirements. Re-injection accounted for a large portion of brine concentration cost, totaling between $\$0.22\cdot bbl^{-1}$ and $\$1.11\cdot bbl^{-1}$. If this liquid was sold as drilling fluid, significant cost savings resulted ($\$0.95\cdot bbl^{-1}$), not including cost of re-injection ($\$0.22$-$\$1.11\cdot bbl^{-1}$) (Figure 9). Capital costs and labor costs were low in comparison to other operational costs in either case, as seen in Table 5 and Appendix B (labor costs account for $\$0.24\cdot bbl^{-1}$).

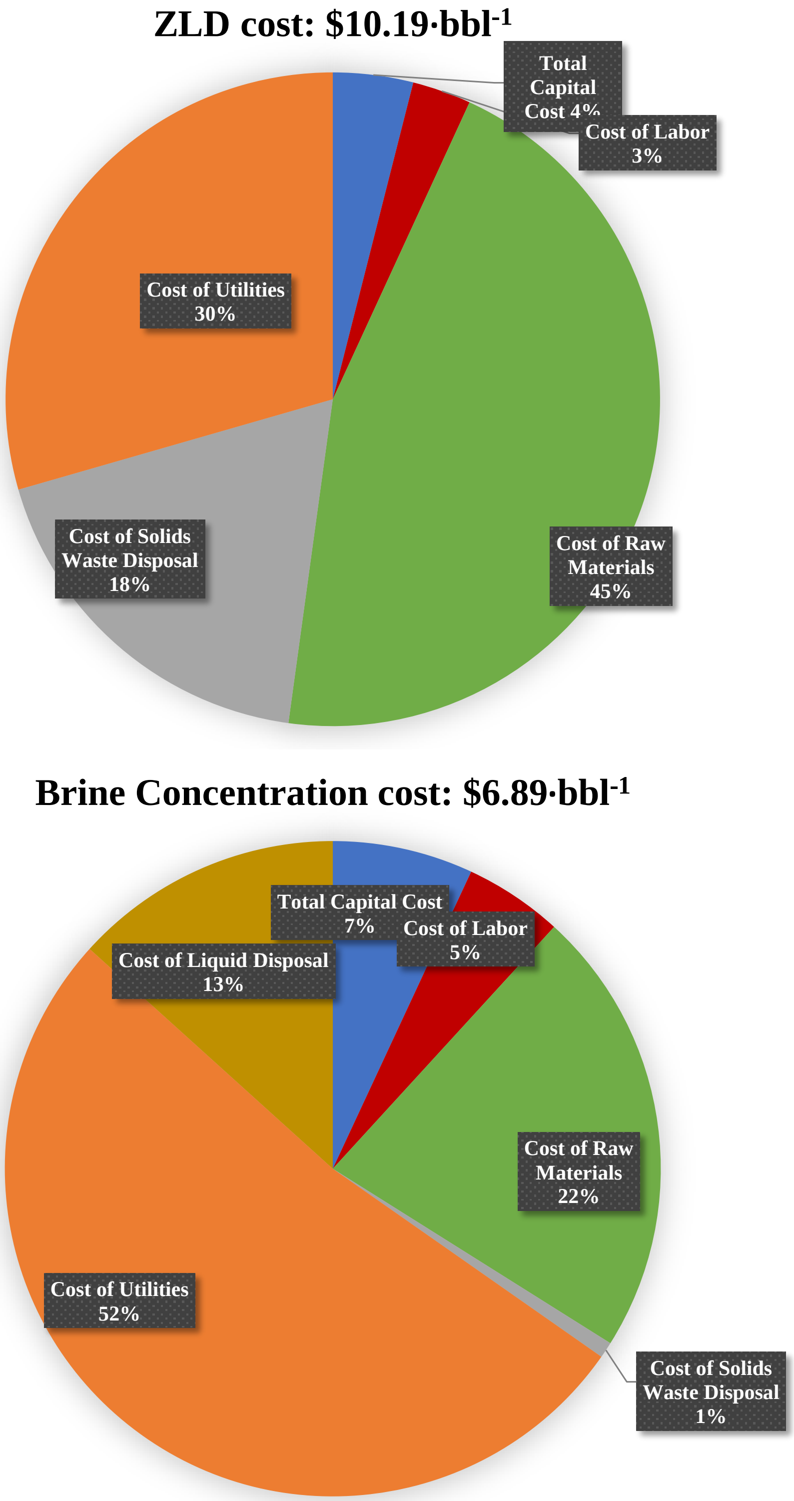

Figure 9: Disposal case cost breakdowns for the ZLD (above) and brine concentration (below) cases.

4.2.1 Recovery Ratio

By increasing power delivered to the desalination system, water vapor recovery is increased. The impact of clean water recovery on treatment case costs ($\$\cdot bbl^{-1}$) was evaluated at the default salinity and pressure values of 176.3 $g\cdot L^{-1}$ and 250 bar, respectively [1], [17]. Results for the brine concentration and ZLD cases are shown in Figure 11 and Figure 12, respectively. For the concentration case, two re-injection costs and a single revenue generation case were considered. The impact of recovery ratio was dependent on the cost of re-injection; higher re-injection costs prioritized larger recoveries, whereas a lower re-injection cost was economical at lower recoveries. In either case the impact was minimal; increasing recovery ratio of 0.4 to 0.6 increased treatment costs from \$5.86 to $\$6.07\cdot bbl^{-1}$ (for lower re-injection costs) and decreased from \$6.98 to $\$6.74\cdot bbl^{-1}$ (for higher re-injection costs). Desalinator power consumption increased with water recovery, while generating less waste for re-injection. Power consumption increased cost by $\$0.39\cdot bbl^{-1}$ and savings due to lower re-injection costs amounted from $\$0.11\cdot bbl^{-1}$ to $\$0.55\cdot bbl^{-1}$. Other impacts were minimal – the capital cost of the system shifted slightly in favor of higher recoveries due to a smaller liquid effluent heat exchanger, corresponding to $\$0.04\cdot bbl^{-1}$ of savings. For creating a drilling fluid, an increase in brine volume was beneficial, as further water recovery will only increase costs. As expected, increasing water recovery from 0.4 to 0.6 led to an increase of $\$0.79\cdot bbl^{-1}$ for the drilling fluid resale case. For the ZLD case, an increased vapor product can be used for further thermal recovery in the heat exchanger used to heat inlet flow. If the brine was flashed or re-injected rather than processed to produce clean vapor, the energy consumed to achieve operating conditions was effectively wasted – the total cost of utilities decreased by $\$0.40 \cdot \text{bbl}^{-1}$ with an increase in mass recovery ratio from 0.4 to 0.6.

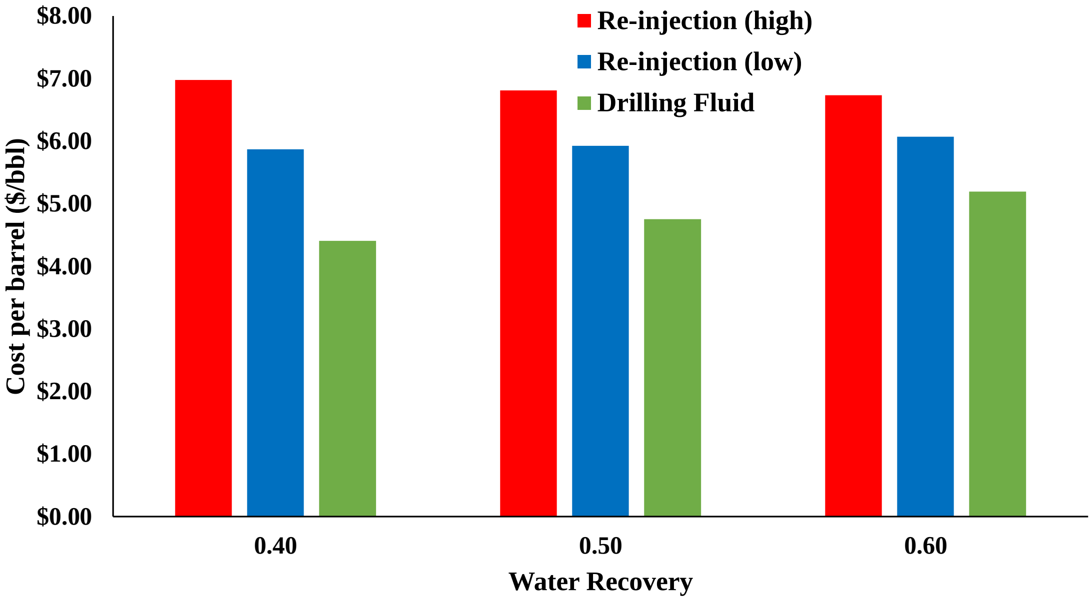

Figure 10: Brine product case process treatment costs ($\$ \cdot \text{bbl}^{-1}$) with increasing water recovery, 176.3 $\text{g} \cdot \text{L}^{-1}$ inlet salinity (at default composition) and 250 bar operating pressure.

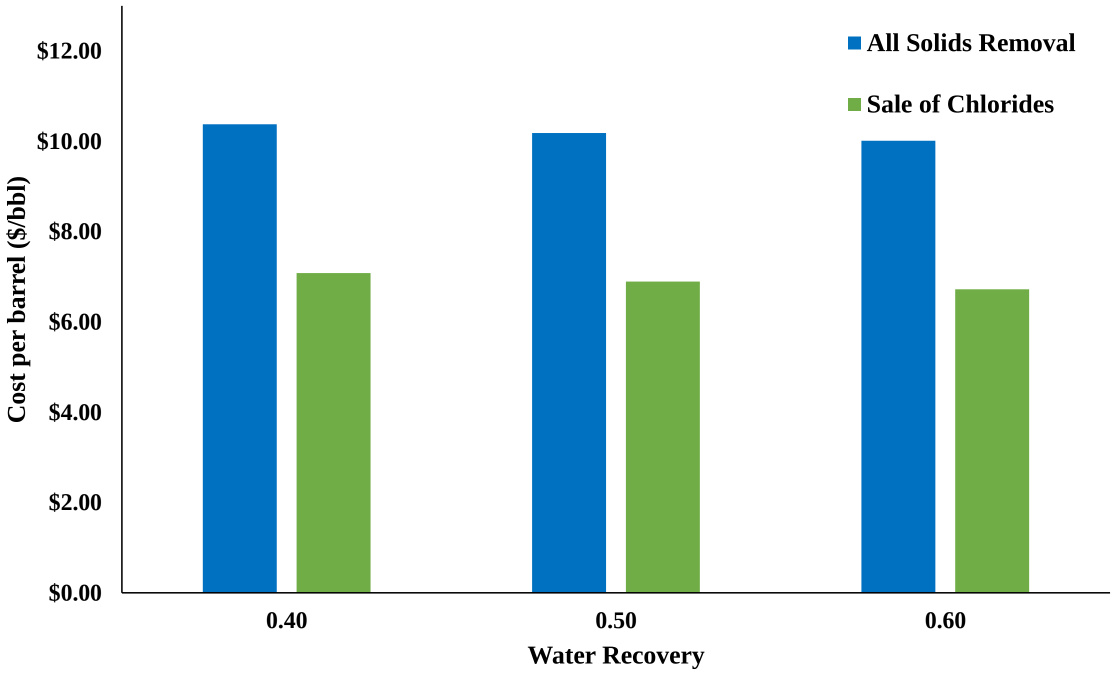

Figure 11: ZLD case process treatment costs ($·bbl^{-1}) with increasing water recovery, 176.3 g·L^{-1} inlet salinity (at default composition) and 250 bar operating pressure.

4.2.2. Inlet Brine Salinity

To evaluate process performance with a wide variety of feedstocks, the inlet salinity was varied between 75 and 270 g·L^{-1} (keeping the anion/cation ratios constant for this case). Brine concentration and ZLD case results with salinity are shown in Figure 12 and Figure 13, respectively. For Figure 11, the high and low costs of re-injection correspond to the respective re-injection costs from Table 5. Based upon estimates using sodium chloride and water solutions [22], a higher salinity brine was expected to have a lower specific heat, resulting in lower desalinator power consumption. However, a lower brine specific heat can also inhibit heat recovery. With a constant water recovery of 0.4, increasing inlet salinity from 75 to 270 $g \cdot L^{-1}$ decreased the inlet temperature to the desalinator from 306 to 258 °C thereby increasing desalinator power requirements from 6,949 kW to 12,890 kW, an increase of $\$1.42 \cdot bbl^{-1}$. Additionally, a higher salinity brine will require greater pretreatment chemical consumption (sulfuric acid, sodium hydroxide and sodium carbonate); for ZLD, this cost (raw materials + solids disposal) increased from $\$2.34 \cdot bbl^{-1}$ to $\$8.07 \cdot bbl^{-1}$. The case of producing a drilling fluid was buffered by higher salinities producing larger quantities of drilling fluid product. The brine savings increased from $\$0.51 \cdot bbl^{-1}$ at 75 $g \cdot L^{-1}$ to $\$1.86 \cdot bbl^{-1}$ at 270 $g \cdot L^{-1}$. It should be noted this limiting case was only shown to complete the trend; a salinity of 270 $g \cdot L^{-1}$ would be easier to simply remove magnesium and sell directly as ten-pound brine. In direct comparison, the ZLD case became more expensive relative to the brine concentration case with increasing salinity due to upfront treatment costs necessary for removal of solids; ZLD and brine concentration costs differed by $\$1.36 \cdot bbl^{-1}$ at 75 $g \cdot L^{-1}$ and $\$5.79 \cdot bbl^{-1}$ at 270 $g \cdot L^{-1}$ for the disposal cases (comparing solids disposal to re-injection) and $\$0.82 \cdot bbl^{-1}$ at 75 $g \cdot L^{-1}$ and $\$2.69 \cdot bbl^{-1}$ at 270 $g \cdot L^{-1}$ for the value-added product (drilling fluid or rock salt) cases.

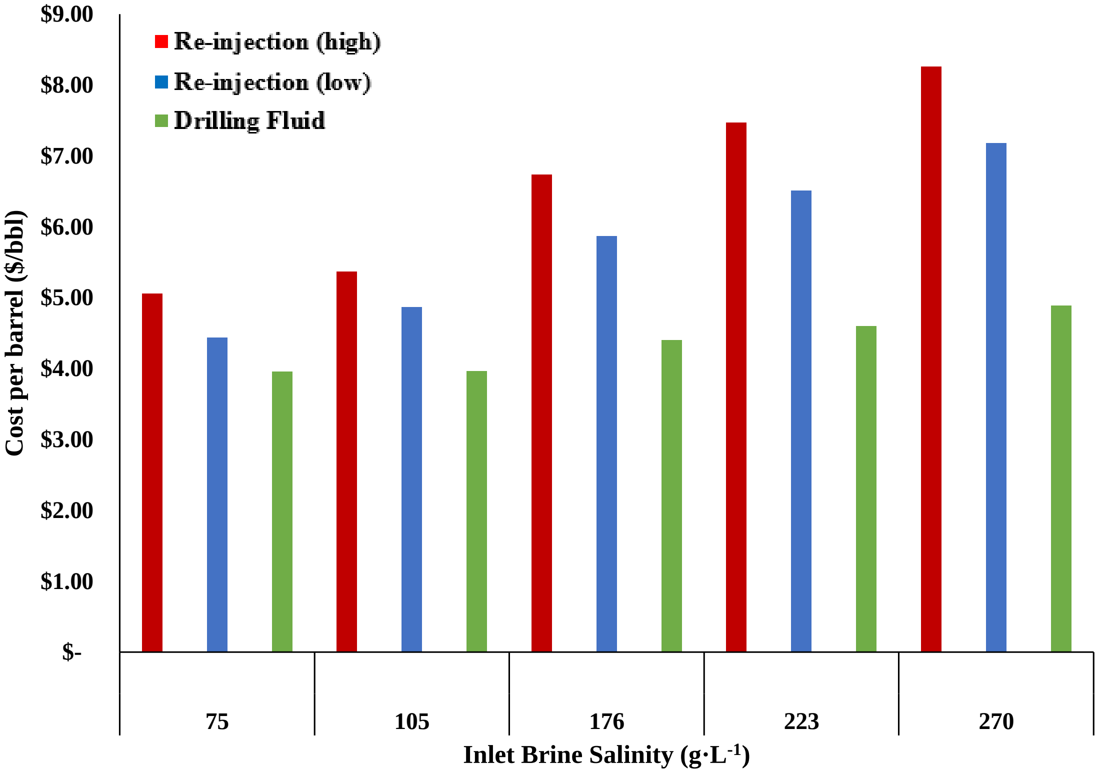

Figure 12: Cost of desalination ($·bbl^{-1}) for increasing salinity for the brine concentration case at 250 bar. For each salinity, the recovery ratio which produces the most favorable cost per barrel is shown.

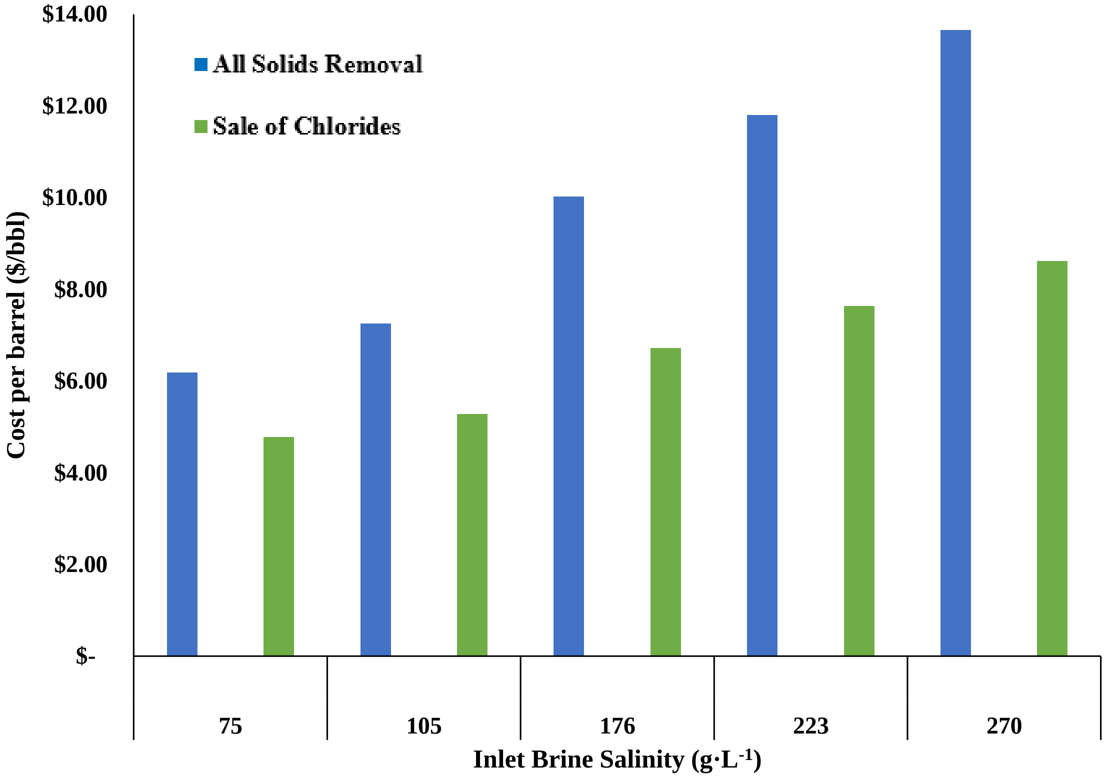

Figure 13: The cost of desalination ($\$\cdot bbl^{-1}$) for increasing salinity for the ZLD case at 250 bar. For each salinity, the recovery ratio which produces the most favorable cost per barrel is shown.

4.2.3 Pressure

Prior experiments [1], [17] provided insight as to the impact of operational pressure on the overall process. Higher desalinator temperatures were necessary with operating pressure to create a clean vapor product; the vapor-liquid equilibrium temperature, T_{vle}, increased with increasing pressure [17]. However, the energy required to generate clean vapor was lower once the appropriate equilibrium temperature is achieved – this was true in binary mixtures of sodium chloride and water [22] and verified using experimental brine data [17]. Table 8 contains these values for the operating pressures studied; note the stark differences in ΔH_{Vap} and T_{vle} as a function of pressure. Here, the “enthalpy of vaporization” denotes the amount of energy required to produce a low TDS vapor from the inlet brine, once the appropriate T_{vle} has been achieved [17].

Table 8: Enthalpies of vaporization, vapor-liquid equilibrium temperatures and pump power requirements as a function of pressure.

Pressure (bar)	ΔH_{Vap} **(kJ·kg^{-1})**	**T_{VLE} (℃)**	**Pump Power (kW)**
230	420	380.1	168.1
250	290	387.8	181.7
280	180	398.4	204.8

The re-injection case shown in Figure 14 presents treatment cost estimates at varying operating salinity combinations. For all cases and salinities, it was more expensive per barrel to create a clean vapor at 230 bar in comparison to 250 bar. This cost discrepancy increased with salinity, \$0.16·bbl^{-1} at 75 g·L^{-1}, \$0.41·bbl^{-1} at 176.3 g·L^{-1}, and \$0.60·bbl^{-1} at 270 g·L^{-1} for the re-injection cases. Thus, the benefit of lower pump power consumption (168 kW vs 182 kW) and lower T_{vle} (380.1 vs 387.8 °C) did not outweigh the increased desalinator power requirement. At a recovery ratio of 0.5 and inlet salinity of 176.3 g·L^{-1}, desalinator power decreased from 11,895 kW to 10,512 kW when moving from 230 to 250 bar for the re-injection cases shown, contributing \$0.33·bbl^{-1} difference between the two cases. Note the vapor produced at 230 bar possessed a lower TDS

(622.3 mg·L^{-1}) than at 250 bar (1167.7 mg·L^{-1}) [1]; thus, it may be preferential to operate at a pressure just above water's critical point in spite of the larger utility requirements depending upon operational strategy. 280 bar required an even higher T_{vle} but corresponded to a lower energy requirement for clean vapor production [17]. The cost per barrel trend past 250 bar, however, is not as large at 75 g·L^{-1}, resulting in a \$0.04·bbl^{-1} difference, increasing to \$0.29·bbl^{-1} at 176.3 g·L^{-1}, and \$0.41·bbl^{-1} at 270 g·L^{-1}. This was another result of decreasing desalinator power as seen in Table 8. At 176.3 g·L^{-1}, for example, the decreased desalinator power requirements corresponded to a decrease of \$0.21·bbl^{-1} for comparable recovery ratios.

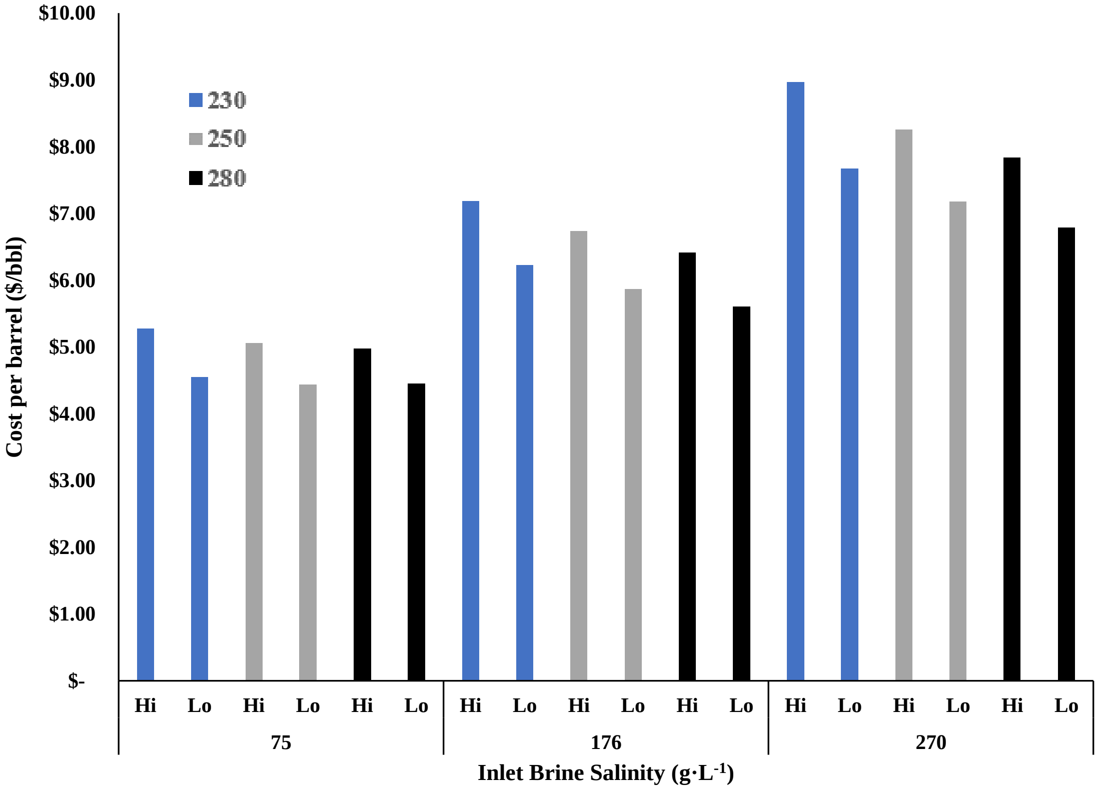

Figure 14: Brine concentration case costs with re-injection with salinity and pressure. For all salinities, the optimum recovery ratio is shown.

4.2.4 Process Cost Sensitivity Analyses

For all other process variables considered, cost ranges are given and compared to the default in Table 9 and Table 10. These costs were based on the high and low values for each variable as detailed in Table 5. For these cases, the salinity, water recovery and pressure were fixed at 176.3 g·L^{-1}, 0.5, and 250 bar, respectively – all variables are fixed to the base case value save for the single variable being considered. Operating costs were highly sensitive to process capacity (flow rate). Treating brine with a considerably smaller system (10 GPM) was more expensive per barrel than a much larger system due to increased capital cost weighting. Electrolysis losses were limited according to Driesner [22]; thus, only two reactor designs for differing voltages were considered. Because of this limitation, alternative reactor designs resulted in minimal savings ($\$0.11\cdot\text{bbl}^{-1}$). Given energetic requirements, power sourcing had an obvious effect on process treatment costs, adding an additional $\$2.40\cdot\text{bbl}^{-1}$ if switching from natural gas to average U.S. power cost. Solid waste disposal and chemical consumption costs had a much larger impact on ZLD operating costs. Non-hazardous waste disposal had a large impact (increasing costs by up to ~$\$2.80\cdot\text{bbl}^{-1}$), while sodium carbonate consumption also had a significant impact (increasing costs by up to $\$2.90\cdot\text{bbl}^{-1}$). Likewise, the ion concentration had a similarly large impact on the ZLD case – a high sodium brine (such as that found in the Permian Basin) [97] would be far easier to treat in this case using ZLD removing the need for extensive divalent cation pretreatment. If all of the final chloride product could be sold, the default case was $\$4.45\cdot\text{bbl}^{-1}$, which could imply a greater degree of success for this process in geographic locations where brine is lower in calcium content. Additionally, if only chloride salts are present, the calcium does not require removal. Removing the need for sodium carbonate led to massive savings in material costs. NORM has minimal impact – although the waste is considered hazardous, the amount produced (even with a 10,000 $\text{pCi}\cdot\text{L}^{-1}$ brine) is considerably lower than the amount of sulfides, carbonates and chlorides produced via ZLD. Note that NORM removal was not considered for brine concentration, as it is assumed not to meaningfully impact re-injection or drilling fluid use. Finally, transportation had a significant impact on the brine concentration case. At $\$5\cdot\text{bbl}^{-1}$, the sale of rock salt and removal of solid wastes (ZLD cases) became more lucrative than simply re-injecting or selling leftover brine, while at $\$15\cdot\text{bbl}^{-1}$ or greater, processing the brine was more cost effective than re-injection. This solidified the importance of minimizing brine production in cases of remote geographic locations, where transportation costs are higher. Note, this transportation cost is not considered in the ZLD case, where costs of disposal factor in transportation.

Table 9: Brine concentration cases sensitivity analysis results.

Brine Concentration					
Default Value: 176.3 $\text{g}\cdot\text{L}^{-1}$ salinity, 250 Bar Pressure, 0.5 water recovery					
Average treatment cost with re-injection (default):	$\$ 6.37\cdot\text{bbl}^{-1}$		Average treatment cost with drilling fluid sale (default):	$\$ 4.75\cdot\text{bbl}^{-1}$	
Variable	Low $	High $	Variable	Low $	High $
Electrolysis Losses	$ 6.26	$ 6.37	Electrolysis Losses	$ 4.64	$ 4.75
Flow Rate	$ 5.65	$ 13.30	Flow Rate	$ 4.03	$ 11.69
Power Source	$ 6.37	$ 8.72	Power Source	$ 4.75	$ 7.11
Non-Hazardous Waste Cost	$ 6.32	$ 6.46	Non-Hazardous Waste Cost	$ 4.71	$ 4.84
Transportation Costs	$ 6.37	$ 15.21	Transportation Costs	$ 4.75	$ 13.60
Ion Concentration	$ 5.12	$ 6.43	Ion Concentration	$ 3.49	$ 4.81
NaOH Cost	$ 5.75	$ 7.61	NaOH Cost	$ 4.13	$ 5.99

Table 10: Zero liquid discharge (ZLD) cases sensitivity analyses results.

Zero Liquid Discharge					
Default Value: 176.3 $g\cdot L^{-1}$ inlet salinity, 250 bar operating pressure, 0.5 water recovery					
Average treatment cost with solids removal (default):	$\$ 10.19\cdot \text{bbl}^{-1}$		Average treatment cost with chloride salt sale (default):	$\$ 6.89\cdot \text{bbl}^{-1}$	
Variable	Low $	High $	Variable	Low $	High $
Electrolysis Losses	$ 10.08	$ 10.19	Electrolysis Losses	$ 6.78	$ 6.89
Flow Rate	$ 9.45	$ 17.28	Flow Rate	$ 6.15	$ 14.05
Power Source	$ 10.19	$ 12.40	Power Source	$ 6.89	$ 9.11
Non-Hazardous Waste Cost	$ 8.78	$ 13.05	Non-Hazardous Waste Cost	$ 6.51	$ 7.66
Hazardous Waste Cost	$ 9.88	$ 12.37	Hazardous Waste Cost	$ 6.58	$ 9.08
NORM Cost	$ 10.00	$ 10.35	NORM Cost	$ 6.71	$ 7.06
Ion Concentration	$ 7.69	$ 10.19	Ion Concentration	$ 4.45	$ 6.89
Ion Removal	$ 7.10	$ 10.19	Ion Removal	$ 3.90	$ 6.89
H_2SO_4 Cost	$ 10.15	$ 10.27	H_2SO_4 Cost	$ 6.87	$ 6.94
NaOH Cost	$ 9.57	$ 11.43	NaOH Cost	$ 6.27	$ 8.13
Na_2CO_3 Cost	$ 8.73	$ 13.10	Na_2CO_3 Cost	$ 5.44	$ 9.80

The impact of each variable on brine concentration and ZLD cases is shown in Figure 15, with cost differences relative to the default. In spite of the sensitivity to key variables (flow rate, ion concentrations, chemical pricing), this process mostly fell within range of other competitive desalination and treatment processes under $\$8\cdot \text{bbl}^{-1}$ [18].

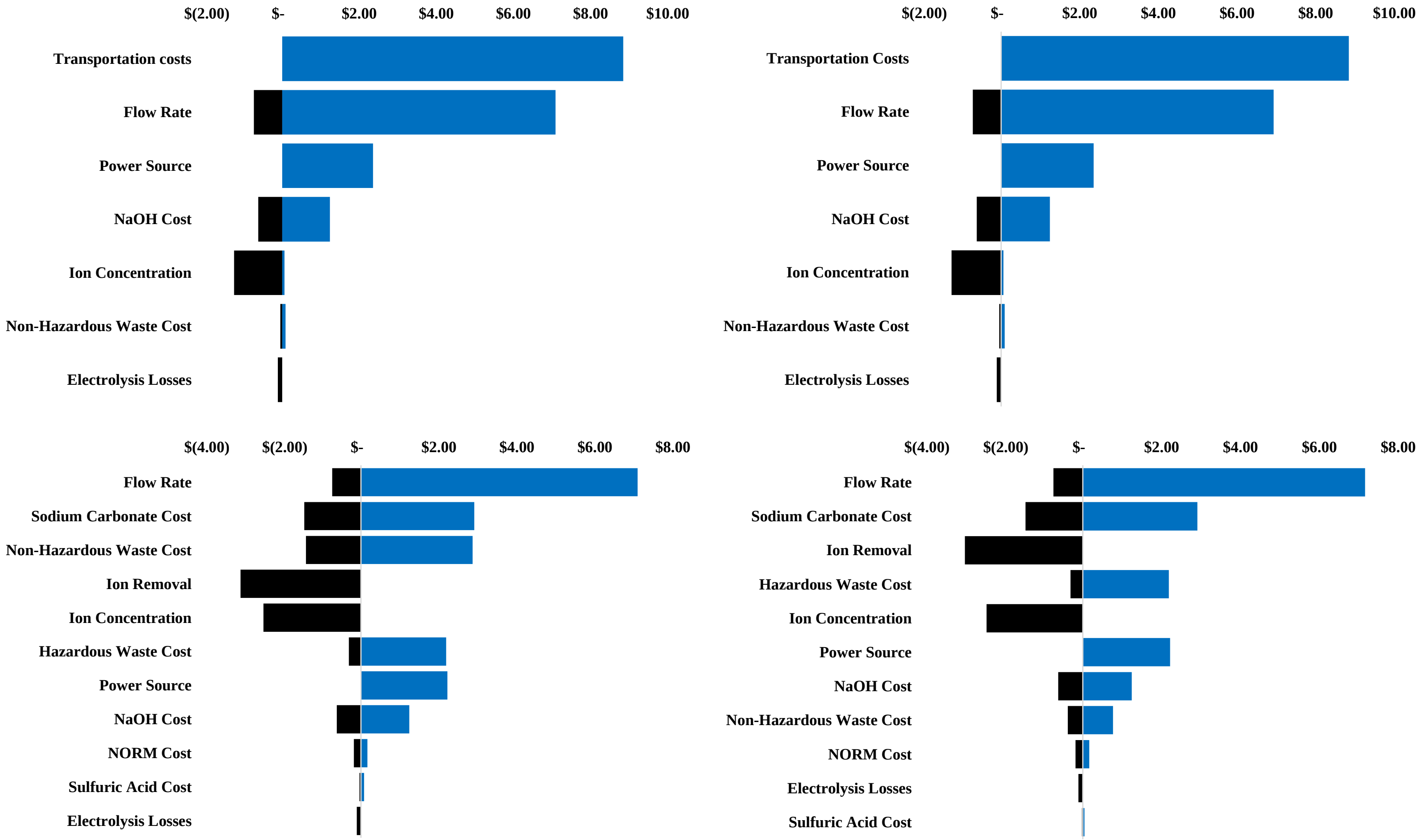

Figure 15: Case sensitivity charts: re-injection (upper-left), drilling fluid (upper-right), solids removal (lower-left) and sale of chlorides (lower-right). The color of the bar denotes the impact on the default case.

4.2.5 Comparison with Conventional Technologies

There are numerous technologies potentially available for brine remediation at lower salinities[12]; however, most of these techniques have not been tested beyond salinities around seawater[65]–[67], [103], [104]. The currently accepted commercial technology for high salinity brine concentration and zero liquid discharge is an evaporator/crystallizer technique; for this technique, SaltWorks[69] makes their energetics for treatment readily available. The comparison between this technique and the SCWD cases considered is shown in Table 7. For this comparison, all salinities, recoveries and pressures were considered to create a range of energetics requirements; however, the flow rate was fixed at 100 GPM. Additional analyses have been completed using a pretreatment step with MVC prior to crystallization in literature [16]; for this analysis, the SaltWorks crystallizer was considered as a single-step process.

Table 11: A comparison between the energetics of the SaltWorks crystallizer and the SCWD process described herein. All energetics units are in kWh·bbl^{-1} for a flow rate of 100 GPM.

	Saltworks	**SCWD**
Brine Concentration	52.9	48.6 - 109.0
ZLD	55.3	48.7 - 116.8

CHAPTER 5: THE SYSTEM $CACL_2$-H_2O: THERMODYNAMIC MODELING AND FLOW CALORIMETRY EXPERIMENTS AT ELEVATED TEMPERATURES AND PRESSURES

5.1 Introduction

H_2O-NaCl solution correlations originally developed by Driesner for seafloor modeling [22], [23] have found application in simulating SCWD systems [1], [15], [17]. Hence, developing similar correlations for 2:1 electrolytes (namely $CaCl_2$) has a number of expected applications. In this paper, a series of correlations were shown that allow for accurate prediction of key thermodynamic and phase properties of H_2O-$CaCl_2$ solutions; namely, (T,P,x) behavior along the critical curve, vapor-liquid equilibria at supercritical temperatures, and density, enthalpy and specific heat correlations across a broad region of the (T,P,x) phase space. In addition, specific heat data for H_2O-$CaCl_2$ has been furnished for high temperatures and pressures, allowing for more accurate determination of specific enthalpies in regions that were previously unavailable [36], [38], [39].

5.2 Results and Discussion

5.2.1 Critical Curve

Behavior of the H_2O-$CaCl_2$ system's critical curve as a function of temperature, pressure and concentration was derived from two data sets. Of these data sets, only the Bischoff data [34] provided estimates of the critical pressure as a function of temperature; these data were expected to be accurate to 0.2 – 1% depending on the temperature/pressure region. To aid regression, the highest pressure data from Tkachenko were also incorporated; for example, a pressure of 311.3 bar at 400 °C [32], [35]. Given the small data size, the critical pressure fit was developed using a least squares fitting algorithm in Python [98]. From these data sets, Equations 1 and 2 were developed to estimate the critical pressure (bar) for the $CaCl_2$-H_2O system, at a given temperature (°C), exceeding water's critical temperature:

$$P_c = a_1 * (T - T_{c,H2O})^{a_2} + P_{c,H2O}, T_c < T < 500 \quad (1)$$

$$P_c = a_3 * (T - T_{c,H2O})^{a_4} + P_{c,H2O}, T \geq 500 \quad (2)$$

where $T_{C,H2O}$ and $P_{C,H2O}$ are the critical temperature and pressure of pure water (373.976 °C and 220.54915 bar). Equation parameter values were given in Table 12. A piecewise-defined function was developed to more accurately predict critical pressure between lower and higher temperature bounds. As the two equations produce nearly identical critical pressure values at 500 °C (differing by $6 \cdot 10^{-4}$ %), this temperature was selected as the piecewise temperature boundary for the equations.

Accuracy of Equations 1 and 2 overall fit of H_2O-$CaCl_2$ system's critical pressure is shown in Figure 16. The critical pressure fit had a strong agreement with low temperature data (less than 2.8% deviation below 500 °C) with increased deviation at higher temperatures (5.0% at 600 °C). This critical pressure curve was also compared to the polynomial fit of Bischoff [34], where there was only a small discrepancy between the two correlations with an identical number of equation coefficients. No data exists for the critical pressure beyond 600 °C; however, extrapolation by researchers at 800 °C for the H_2O-$CaCl_2$ system [32] predicted that the critical pressure is approximately 2,500 bar. Equation 2 reasonably predicted behavior within this high temperature region, whereas the Bischoff curve significantly over predicted critical pressure (reaching over 4,000 bar) in the data shown. No further attempts were made to calculate critical pressure beyond 600 °C, and equations of state for the H_2O-$CaCl_2$ system at these conditions were lacking. Given the accuracy of Equations 1 and 2 at lower temperatures to 600 °C in addition to the projection, the curve was believed to reasonably estimate critical pressure at temperatures up to 800 °C.

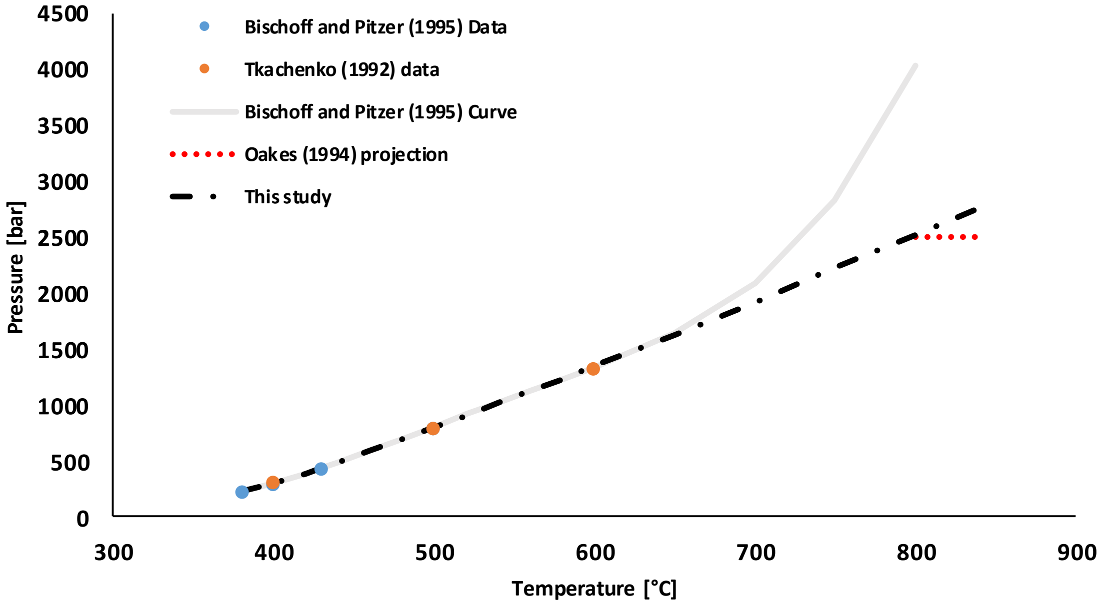

Figure 16: Critical pressure for H_2O-$CaCl_2$ system with temperature.

The Bischoff data set [34] was used with additional fluid inclusion data from Oakes [32] to derive critical composition as a function of temperature. Given the size of the data set, the least squares algorithm was used in Python for this fit as well [98]. Accurate prediction of critical composition as a function of temperature required development of a piecewise-defined function shown in Equations 3 and 4:

$$x_c = b_1 * \ln\left(b_2 * (T - T_c)\right), T: 380 - 450 \text{ °C} \qquad (3)$$

$$x_c = b_3 * \ln\left(b_4 * (T - T_c)\right), T > 450 \text{ °C} \qquad (4)$$

Here, x_c defines the critical composition as the mass fraction of $CaCl_2$. Equation parameter values were given in Table 12. Figure 17 presents a comparison of predicted and estimated critical composition data by Bischoff [34]. Note, Bischoff et al. [34] were unable to generate a polynomial fit for this difficult data set; the authors stated that the curve is complex and too difficult to fit to a polynomial. In addition, later regression efforts by Shibue [105] were also compared; this fit was only used to 500 °C with moderate success. The two data sets used [32], [34], [35] converged at T > 450 °C; however, from 395-400 °C there exist obvious differences between the two data sets (a stark increase in molality of 0.5 mol/kg to 0.9 mol/kg over 5 °C). The curve thus interpolated between these two points.

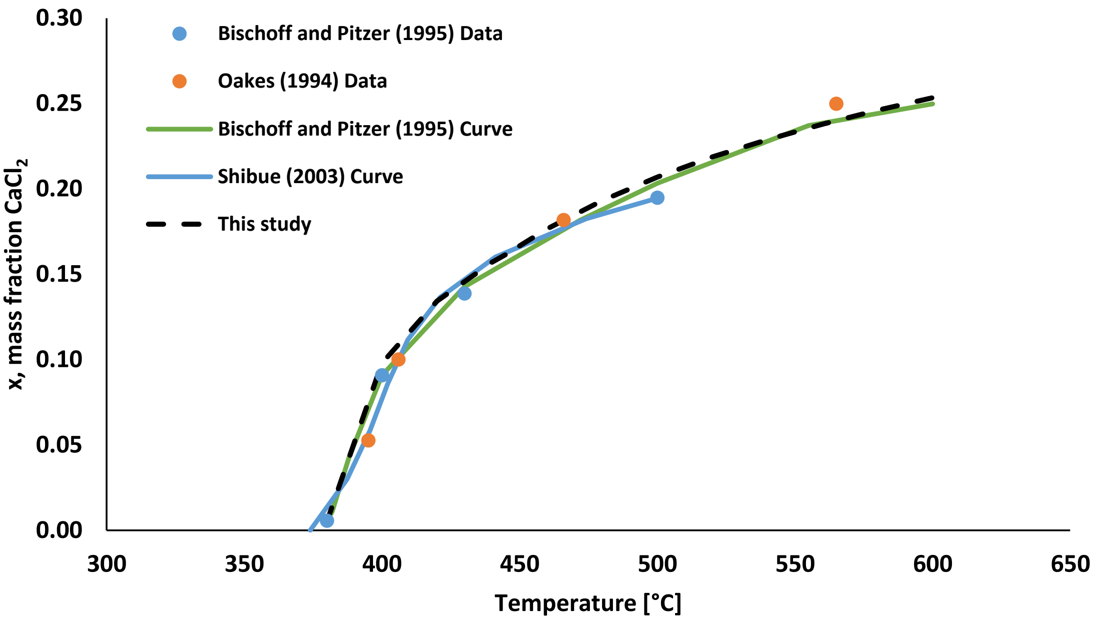

Figure 17: The critical composition (in mass fraction) for H_2O-$CaCl_2$ system as a function of temperature. Note the discrepancy between the two data sets near 400 °C.

Table 12: Parameters for critical pressure and composition in Equations 1-4.

a_1	1.77651
a_2	1.19719
a_3	2.45957
a_4	1.12992
b_1	6.35667×10^{-2}
b_2	1.79173×10^{-1}
b_3	7.96735×10^{-2}
b_4	1.06478×10^{-1}

5.2.2 Vapor-Liquid Equilibria Around Critical Conditions

The liquid branch of the vapor-liquid (V+L) equilibria envelope for the H_2O-$CaCl_2$ system near the critical conditions was effectively described by a logarithmic relationship, terminating at the critical composition of $CaCl_2$ at each critical pressure (denoted by Equations 1-4 above). This is shown in Equation 5:

$$x_{VLE,L} = x_c + d_1 * \ln\left(1 + d_2 * (P_c - P)\right) \quad (5)$$

Note here that at each $P = P_c$, the logarithmic term trends towards 0, and $x_{VLE,L}$ appropriately produced the critical composition (Equations 3 and 4) . The d_1 and d_2 terms were linearized functions with respect to temperature yielding an overall relationship with respect to temperature and pressure according to Equations 6 and 7:

$$d_1 = d_{11} + \frac{d_{12}}{1+e^{\frac{T-d_{13}}{d_{14}}}} \quad (6)$$

$$d_2 = d_{21} + \frac{d_{22}}{1+e^{\frac{T-d_{23}}{d_{24}}}} \quad (7)$$

This fit produced a sound overall curve for the five temperatures for which there is data with an average deviation of 5% for the logarithmic curves in Figure 19. Where there is discrepancy between the two data sets [34], [35] (e.g. at 400 °C), the regressed curve provided good agreement between the data sets.

The vapor branch of V+L envelope was considerably more difficult to accurately estimate using conventional methods, most notably because of the degree of hydrolysis of $CaCl_2$ present in one of the two studies available on high temperature vapor-liquid equilibria [34]. This caused inconsistent vapor concentration values far from the critical point. For reference, this is shown in Figure 20 from Bischoff [34]. For near critical behavior the relationship shown in Equation 8 was developed:

$$x_{VLE,v} = \frac{x_c}{1+e_1*(P_c-P)^{e_2}} \qquad (8)$$

Constant relationships for this portion of the vapor branch follow a similar relationship for temperature:

$$e_1 = e_{11} + \frac{e_{12}}{1+e^{\frac{T-e_{13}}{e_{14}}}} \qquad (9)$$

$$e_2 = e_{21} + \frac{e_{22}}{1+e^{\frac{T-e_{23}}{e_{24}}}} \qquad (10)$$

As discussed, Figure 19 depicts good agreement for the five temperatures depicted in the data sets [32], [34] for both vapor and liquid branches near the critical point. Where critical point data discrepancy exists, the regressed curve crossed between the data sets.

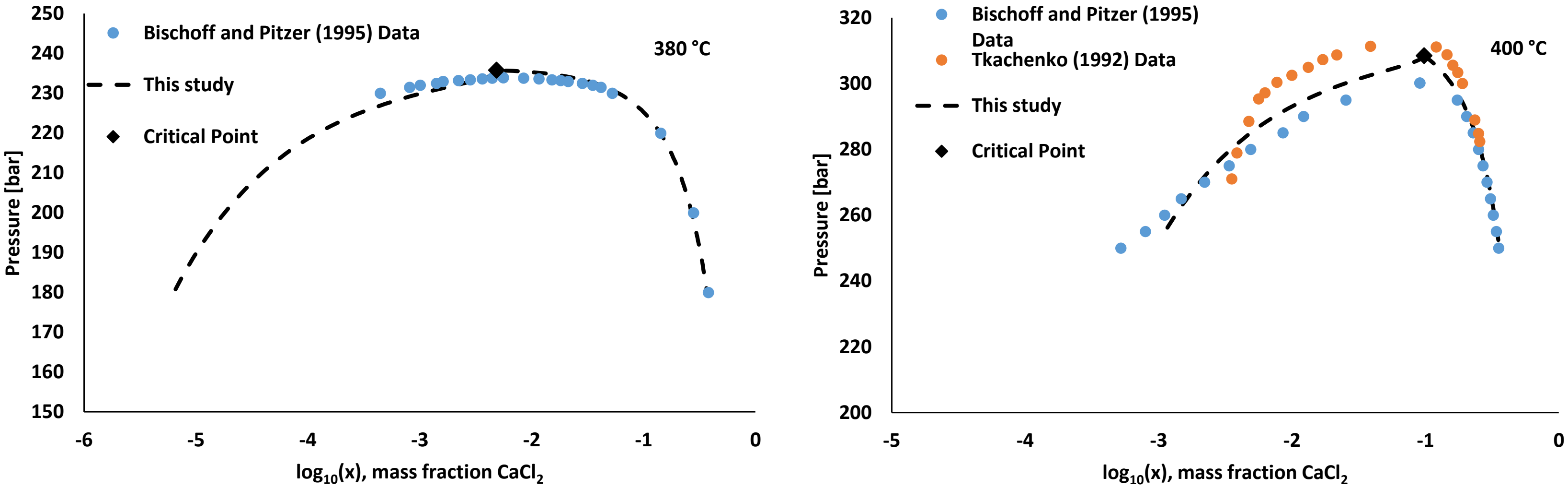

Figure 18: Isothermal sections of the V+L surface as compared to data from literature [34], [35]. Composition (mass fraction) is given on a logarithmic scale.

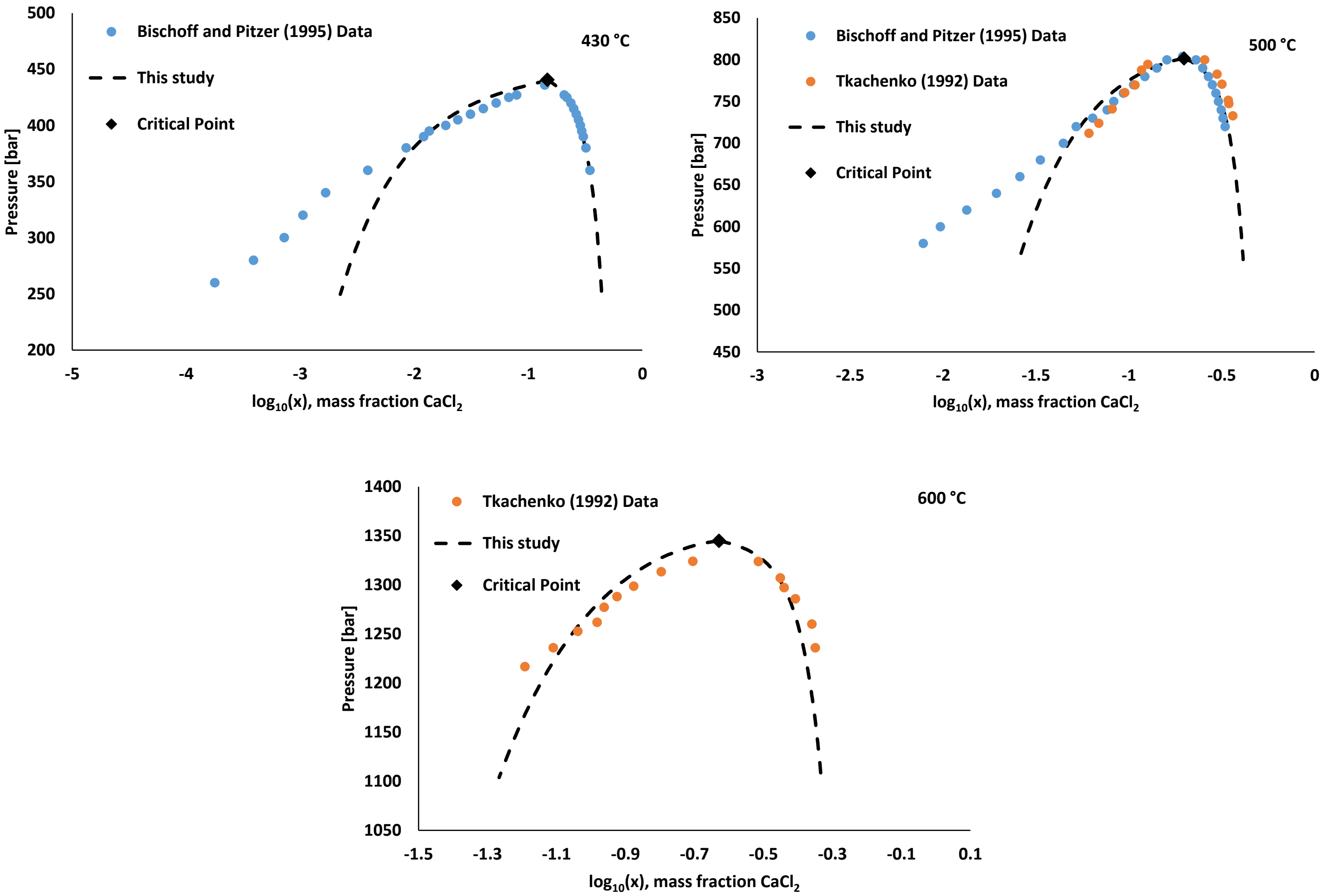

Figure 19: Isothermal sections of the V+L surface as compared to data from literature [34], [35]. Composition (mass fraction) is given on a logarithmic scale.

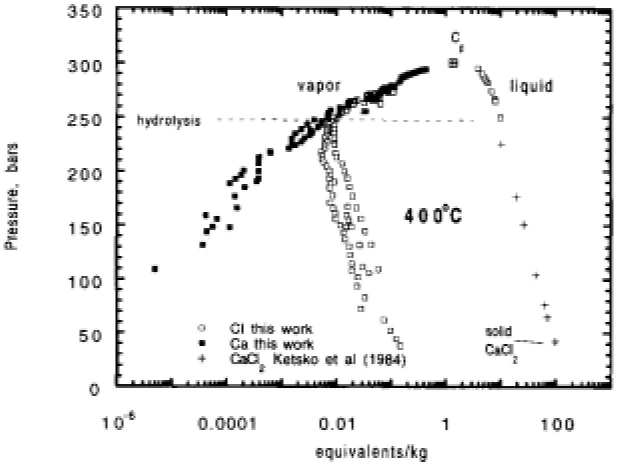

Figure 20: V+L data for the H_2O-$CaCl_2$ system at 400 °C. Note the degree of hydrolysis below 250 bar pressure, where Ca and Cl values are divergent [34].

Table 13: Constants for Equations 5-10.

d_{11}	6.82646×10^{-2}
d_{12}	5.70518×10^{5}
d_{13}	-1.48536×10^{1}
d_{14}	2.77822×10^{1}
d_{21}	4.65448×10^{1}
d_{22}	-9.33086×10^{1}
d_{23}	6.81660×10^{1}
d_{24}	5.52281×10^{4}
e_{11}	5.70452×10^{-2}
e_{12}	6.25587
e_{13}	5.37037×10^{1}

Table 13 Continued

e_{14}	7.12679
e_{21}	7.24378×10^{-1}
e_{22}	1.52806×10^{1}
e_{23}	2.79428×10^{2}
e_{24}	4.74443×10^{1}

5.2.3 Specific Volume

In contrast to the data for phase behavior at criticality, there was a wealth of information on the effect of $CaCl_2$ concentration on solution density at a variety of temperatures and pressures. The full extent of the available data is tabulated for convenience in Table 6. Most of this data was collected for low temperature solutions below 80 °C; however, higher temperature data was still available.

In building parametrizations for specific volume, a similar method to the Driesner correlations was followed [22], where the equivalent specific volume was found for pure water and a parametrization was developed to produce the T* shown in Equation 11:

$$V_s(T, P, x) = V_{H_2O}(T^*, P) \qquad (11)$$

where T* is a function of x and P. There was comparatively limited data for pure $CaCl_2$ densities at different temperatures and pressures due to stability; thus, no validation data could be provided at the endpoints where x = 1. For higher temperature data, this shift generated accurate specific volume predictions at a variety of concentrations and pressures. However, at lower temperatures and depending on the composition (for example, 50 °C and 20 wt. % $CaCl_2$), the density of an aqueous $CaCl_2$ solution can far surpass any pure water densities at constant pressure. Thus, only data above ambient conditions were considered for the following correlations. The T* fit is of the form of Equation 12:

$$T^* = f_1 + f_2 T \qquad (12)$$

Here, the constants used in the fit are functions of composition (Equation 13) and pressure (Equation 14):

$$f_1 = f_{10}x^{1.3} + f_{11}x^{1.4} + f_{12}x \qquad (13)$$

$$f_2 = (1 + \frac{x}{f_{20}}) + f_{21}x^{0.8} + f_{22}x^3 \qquad (14)$$

The formulations were written such that f_1 = 0 and f_2 = 1 at x = 0. Here, x is the mass fraction of $CaCl_2$ and P is expressed in bar with temperature in Kelvin. This correlation was solved using the Nelder-Mead algorithm with the IAPWS-95 equation in Python [98]–[100] for pure water.

Table 14: Expressions for the terms used in Equations 13-14.

f_{10}	9.74269 x 10^3
f_{11}	-7.85361 x 10^3
f_{12}	$-4.04567\ x\ 10^{-3} + -1.41846\ x\ 10^{-1} * \left(\frac{P}{10}\right)^{1.73391}$
f_{20}	5.445618 x 10^3
f_{21}	1.729618
f_{22}	$-4.10363 + -1.23621 * \left(\frac{P}{10}\right)^{3.46425\ x\ 10^{-2}}$

This function was able to predict the H_2O-$CaCl_2$ system specific volume over a wide range of temperatures, pressures and compositions. The ranges and number of data points considered is shown in Table 15. The maximum deviation for the fit was approximately 2.3%; this is shown in histogram form in Figure 21. In addition, individual histograms for select data sets are shown in Figure 22 and Figure 23.

Table 15: Ranges and number of data points considered for Equations 11-14.

Total number of data points considered	417
T (K)	318-643
P (bar)	1-787
x	1.67×10^{-3} – 0.264

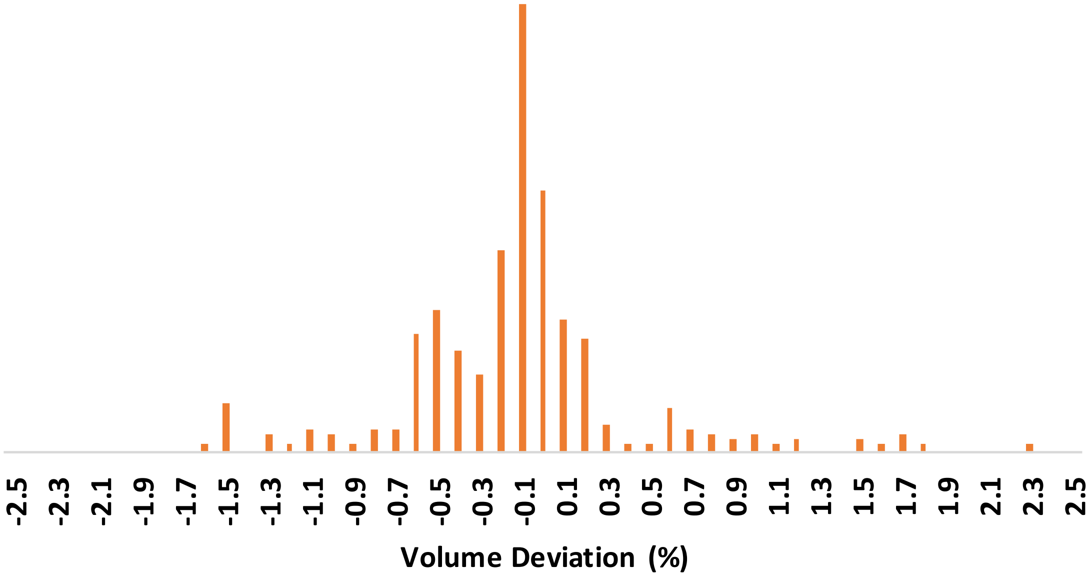

Figure 21: Histogram of deviation from the specific volume fit for all data points considered.

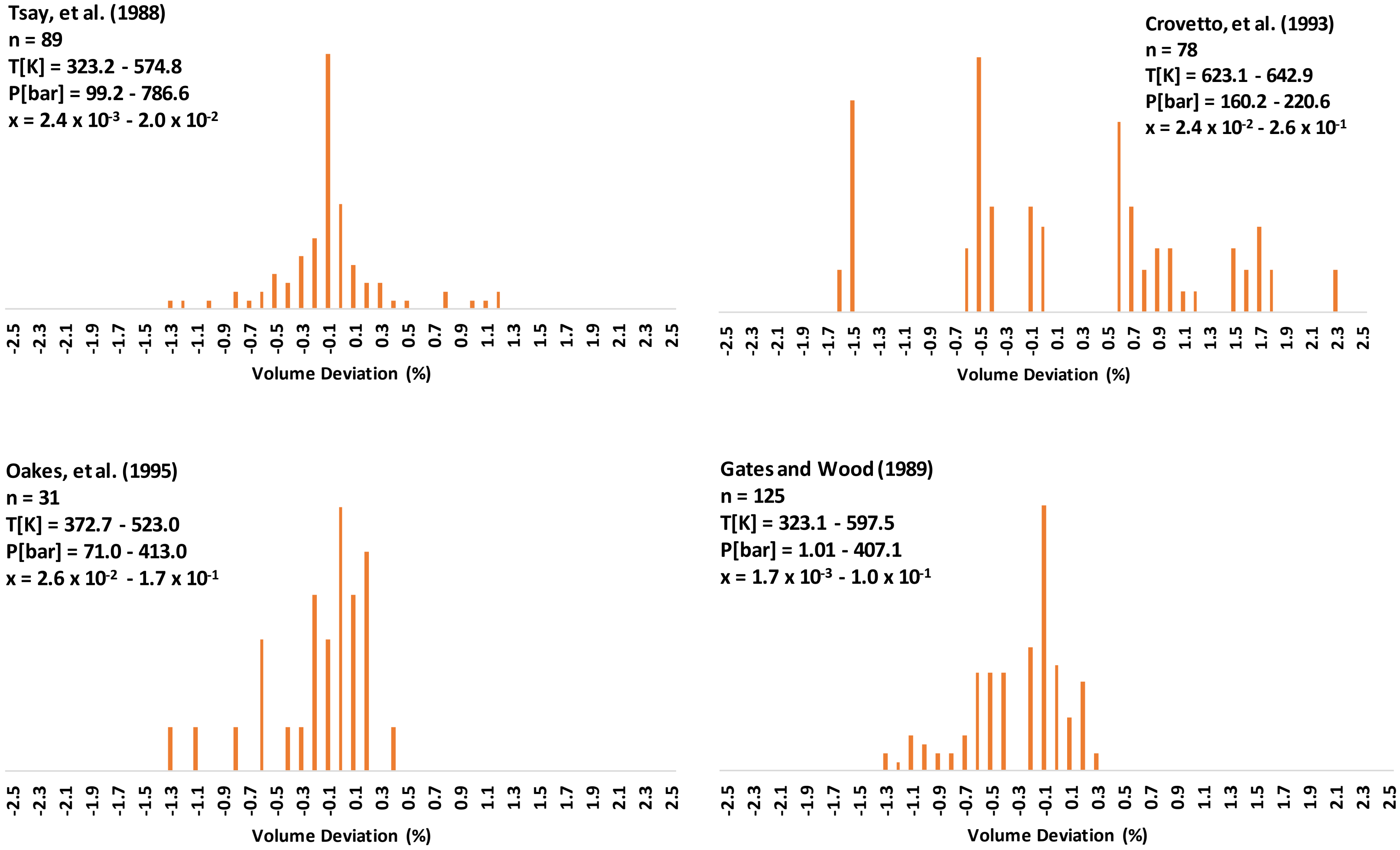

Figure 22: Deviations for select data sets along with the number of points, temperatures, pressures, and mass fractions considered.

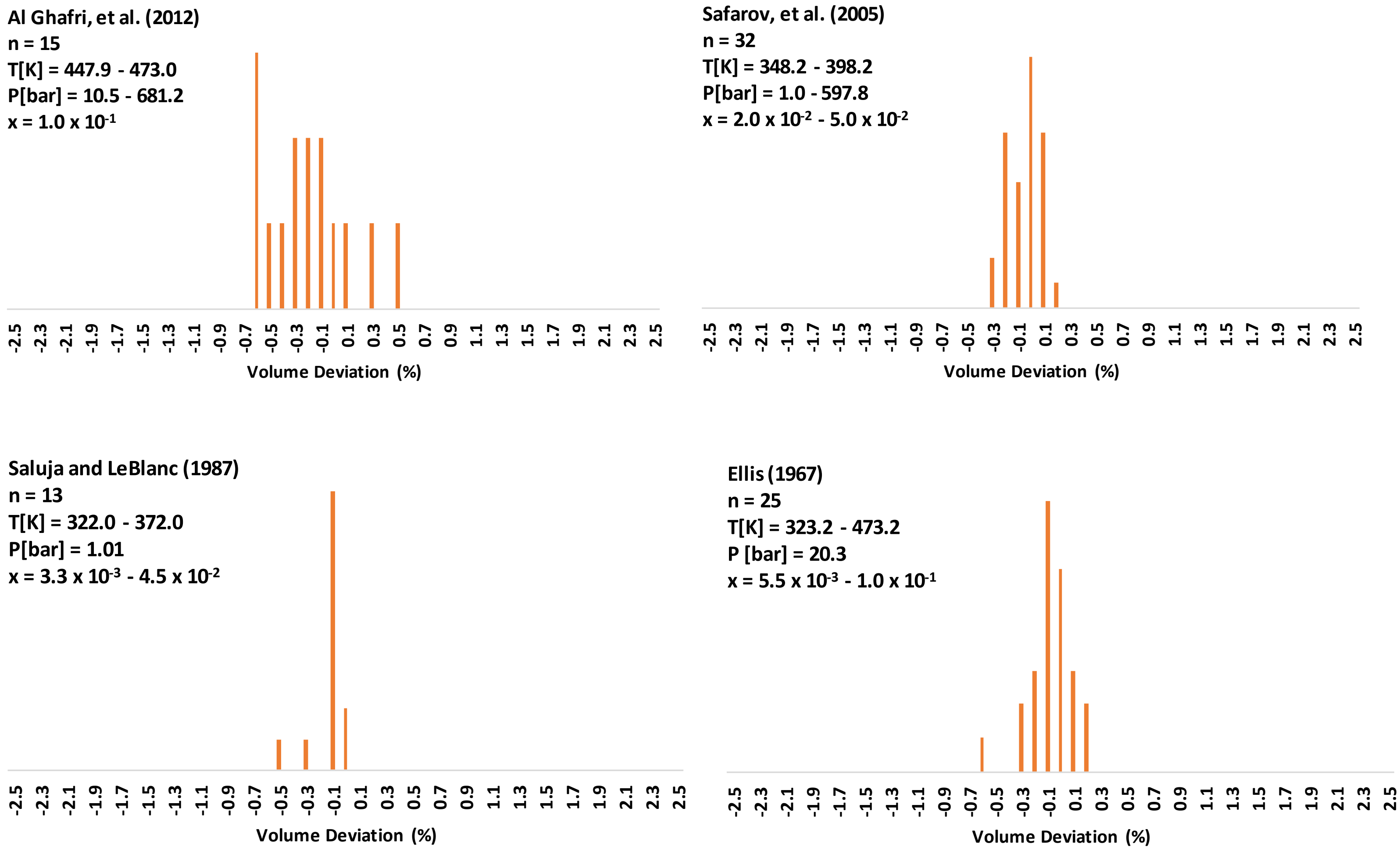

Figure 23: Deviations for select data sets along with the number of points, temperatures, pressures, and mass fractions considered.

Lower temperature data (less than 200 °C) was fit to this specific volume equation with good agreement (<1 %) [45], [48], [54], [55]. For higher temperatures, deviations between 1-2% can be seen [33], [40]–[42]. The largest deviation was seen in the Crovetto data set at 2.3% [41]; there were multiple measurements for each pressure and temperature which provided a small window of potential densities at each mass fraction. Figure 24 contains specific volume data for two higher temperatures (above 350 °C) and different pressure regions as compared with the relationship developed in this study in Equations 11-14.

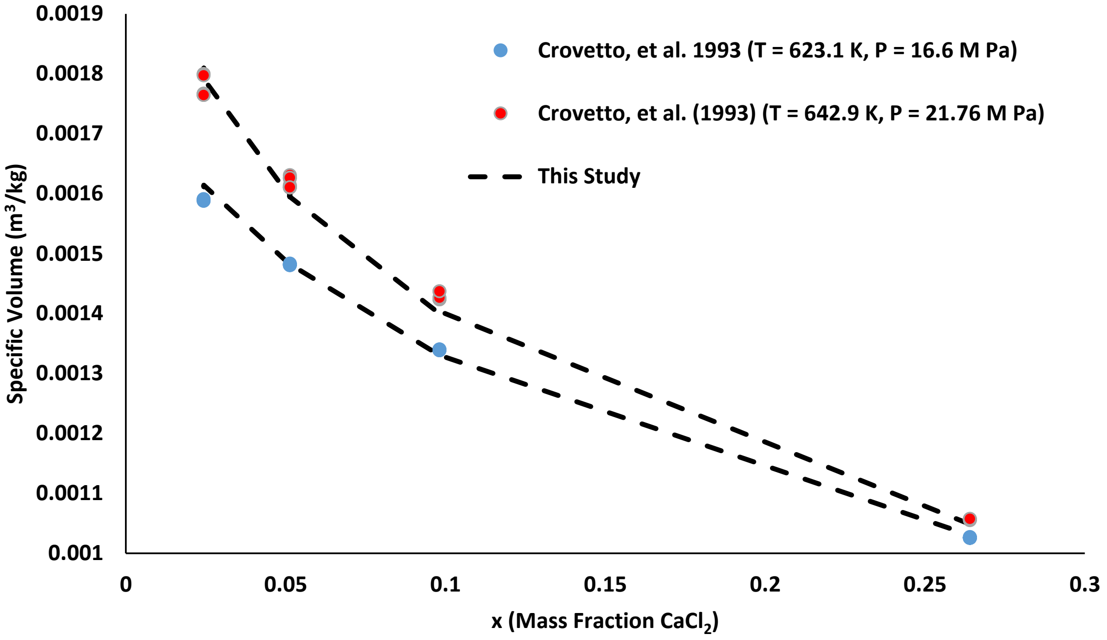

Figure 24: The Crovetto [41] data as compared to Equations 11-14. Note the data set contains very slight variations in temperature and pressure.

Because of the relative uncertainty of the data set (>5%) [32], critical densities as a function of temperature, pressure and mass fraction were not used in the regression analysis. However, attempting to extrapolate into the critical region demonstrated a sensible fit with the critical density data; these are shown as functions of $CaCl_2$ mass fraction (x) in Figure 25. This success suggested that Equations 11-14 are expected to provide relative validity outside of the range of data studied.

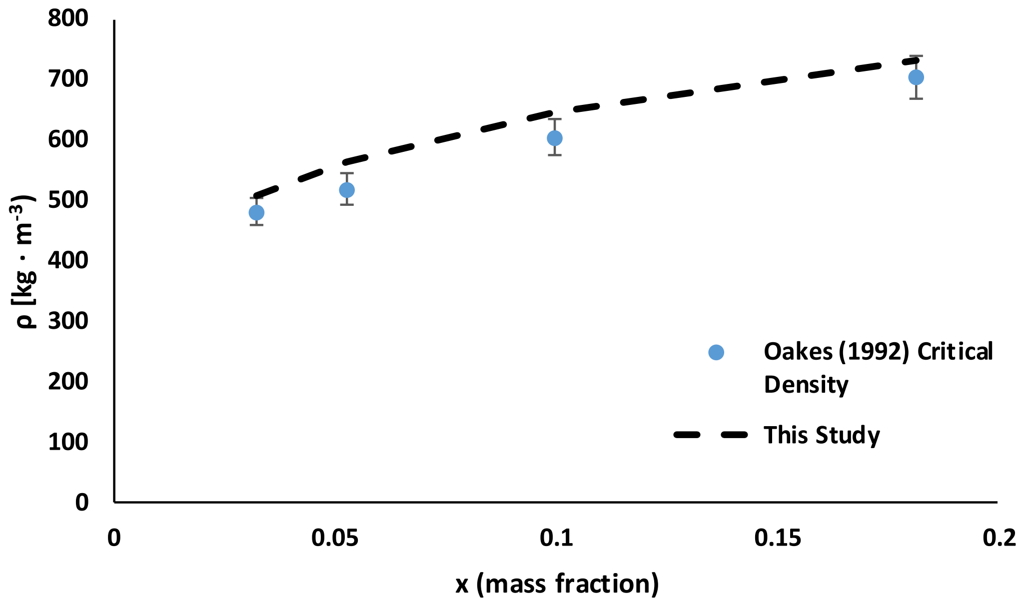

Figure 25: H_2O-$CaCl_2$ critical density from literature [33] compared with the results derived from Equations 11-14.

5.2.4 Enthalpy and Specific Heat

Data for specific enthalpies of the H_2O-$CaCl_2$ system are uncommon; however, indirect enthalpy measurements are possible with the enthalpy of dilution [38], [39] or specific heat [36], [37], [44], [54]. The specific volume correlation can be used to directly determine the specific enthalpy for a given condition using thermodynamic relations shown in Equation 15 [22], [106]:

$$\left(\frac{\partial h}{\partial x_{CaCl_2}}\right)_{T,P} = \left[T\left(\frac{\partial P}{\partial T}\right)_{v,X} - v\left(\frac{\partial P}{\partial v}\right)_{T,x}\right]\left(\frac{\partial v}{\partial x}\right)_{T,P} \qquad (15)$$

This computation was difficult to use for expedient calculations; in addition, it was of interest to fit the enthalpy data to the existing data for dilution enthalpies and specific heat measurements. Thus, this calculation was used as a starting point, and utilized data in literature for the following relations for specific enthalpy. The correlation was similar in form to the specific volume correlation:

$$T^* = g_1 + g_2 T \qquad (16)$$

$$g_1 = g_{10}x + g_{11}x^{0.9} + g_{12}x^{1.3} \qquad (17)$$

$$g_2 = (1 + \frac{x}{g_{20}})^3 + g_{21}x^2 + g_{22}x^{0.9} \qquad (18)$$

Table 16: Constants and expressions for Equations 17 and 18.

g_{10}	2.10230 x 10^{2}
g_{11}	-8.74890 x 10^{1}
g_{12}	$2.20958\ x\ 10^{-1} + -1.21705\ x\ 10^{-2} * \left(\frac{P}{10}\right)^{8.32496\ x\ 10^{-2}}$
g_{20}	$-5.43495\ x\ 10^{-1} + -3.34714\ x\ 10^{-2} * \left(\frac{P}{10}\right)^{-3.87610\ x\ 10^{-2}}$
g_{21}	1.87986 x 10^{2}
g_{22}	-1.67305

Using the enthalpies calculated from Equation 15, the Nelder-Mead algorithm [98], [99] fit the T* data to the appropriate T* given by the IAPWS equation of state [100]. Once the initial constants were determined, points were added in an iterative method from the existing C_p and H_{dil} data:

$$H_2 = C_P * (T_2 - T_1) + H_1 \quad (19)$$

$$H_2 = \left(\Delta H_{dil} + \frac{H_1 - H_w}{m_1}\right) * m_2 + H_w \quad (20)$$

Thus, using C_p or H_{dil} literature data (including relevant molalities), data can be added to correct for anomalies present in the initial data set from Equation 15.

The C_p data included results from of the experimental system discussed in Section 4.3.2, shown here in Table 17. Given the limitations of the system, the relative error of measurements amounted to approximately 10%. The impact of mass fraction on specific heat was statistically significant, whereas small changes in pressure and temperature did not have a significant impact in this region.

Table 17: Specific heat results for aqueous $CaCl_2$ solutions. x (mass fraction $CaCl_2$) precedes each data set.

x = 0.1			x = 0.15			x = 0.2		
T [K]	P [bar]	C_p [J · g^{-1} · K^{-1}]	T [K]	P [bar]	C_p [J · g^{-1} · K^{-1}]	T [K]	P [bar]	C_p [J · g^{-1} · K^{-1}]
309.4	230	4.3 ± 0.3	310.0	230	3.8 ± 0.4	309.4	230	3.5 ± 0.3
314.7	230	4.4 ± 0.3	315.0	230	3.8 ± 0.4	314.1	230	3.6 ± 0.3
319.5	230	4.4 ± 0.4	319.8	230	3.9 ± 0.4	319.7	230	3.6 ± 0.3
325.3	230	4.5 ± 0.3	325.2	230	4.0 ± 0.4	325.2	230	3.7 ± 0.4
330.4	230	4.5 ± 0.4	329.7	230	4.1 ± 0.5	330.1	230	3.8 ± 0.4
335.6	230	4.7 ± 0.4	334.6	230	4.2 ± 0.4	334.8	230	3.9 ± 0.4
339.5	230	4.8 ± 0.4	339.3	230	4.4 ± 0.5	339.7	230	4.0 ± 0.4
314.9	245	4.6 ± 0.4	313.7	245	4.1 ± 0.5	314.9	245	3.7 ± 0.3
319.8	245	4.6 ± 0.3	319.4	245	4.2 ± 0.5	320.1	245	3.7 ± 0.3
325.2	245	4.8 ± 0.4	324.6	245	4.3 ± 0.4	324.7	245	3.8 ± 0.3
330.0	245	4.8 ± 0.4	330.0	245	4.5 ± 0.5	328.7	245	3.8 ± 0.3
335.1	245	4.8 ± 0.4	334.5	245	4.6 ± 0.5	334.2	245	3.8 ± 0.3
340.2	245	5.0 ± 0.4	339.7	245	4.7 ± 0.6	339.0	245	3.9 ± 0.3
344.3	245	5.0 ± 0.4	344.7	245	4.6 ± 0.4	345.1	245	4.1 ± 0.4
320.0	260	4.5 ± 0.4	319.5	260	4.0 ± 0.4	319.7	260	3.7 ± 0.3
324.8	260	4.5 ± 0.4	325.3	260	4.1 ± 0.4	325.5	260	3.8 ± 0.3
329.8	260	4.6 ± 0.5	330.1	260	4.2 ± 0.5	330.2	260	3.9 ± 0.4
335.0	260	4.7 ± 0.4	334.7	260	4.3 ± 0.4	334.8	260	3.9 ± 0.4
339.7	260	4.9 ± 0.5	339.8	260	4.4 ± 0.5	339.8	260	4.0 ± 0.4
344.8	260	5.0 ± 0.5	345.3	260	4.6 ± 0.5	345.0	260	4.1 ± 0.4
349.7	260	5.1 ± 0.5	350.1	260	4.8 ± 0.6	351.0	260	4.3 ± 0.4

The data in Table 17 was compared directly to Equations 16 – 18 in Figure 26. The correlations for enthalpy produced values that were within error of the experimental result for all but two of the specific heat points across all temperatures, pressures and compositions, with a maximum deviation for all data sets of 12.8%.

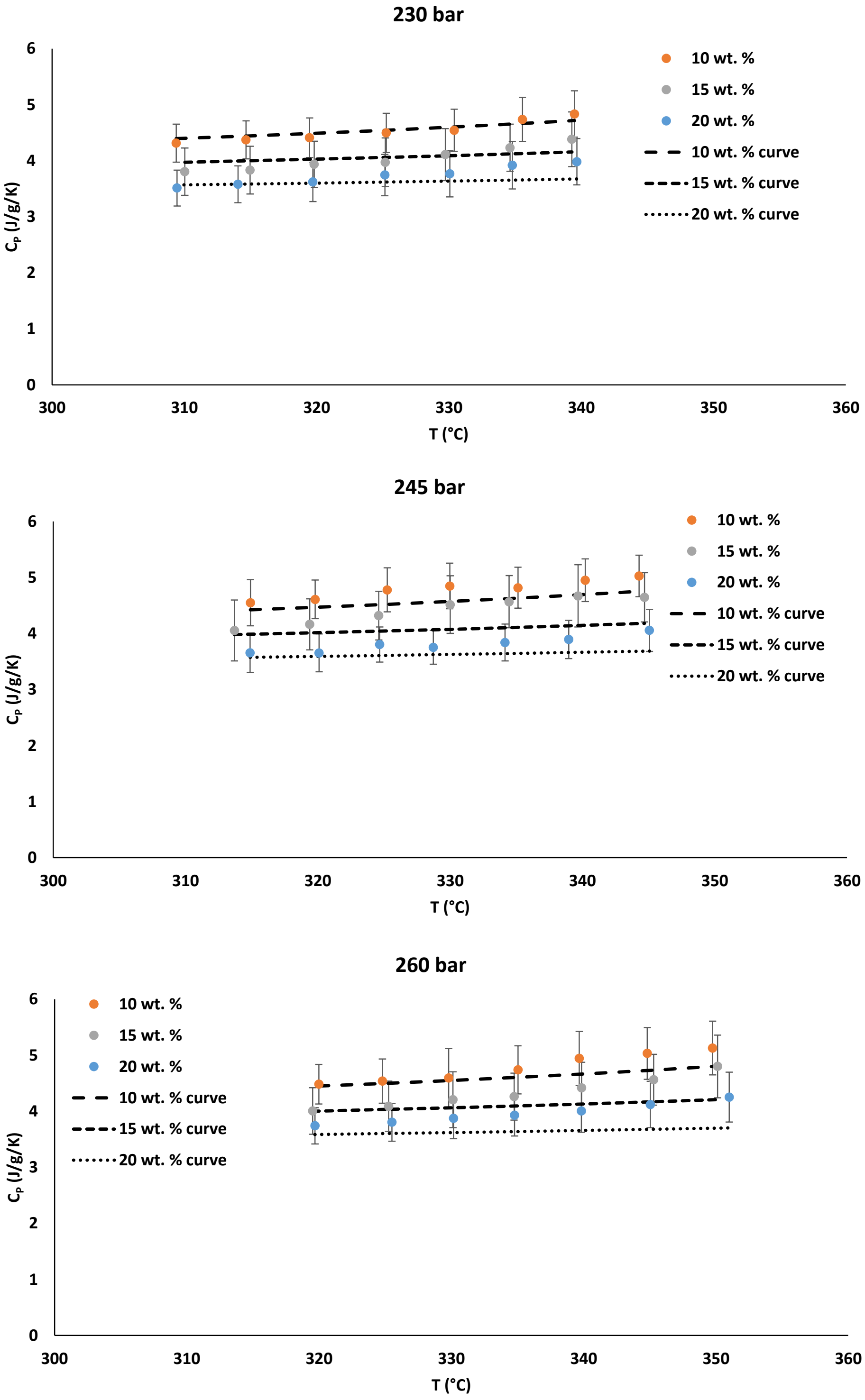

Figure 26: Experimental data from this study as compared to Equations 16-18. All weight percents are in reference to $CaCl_2$.

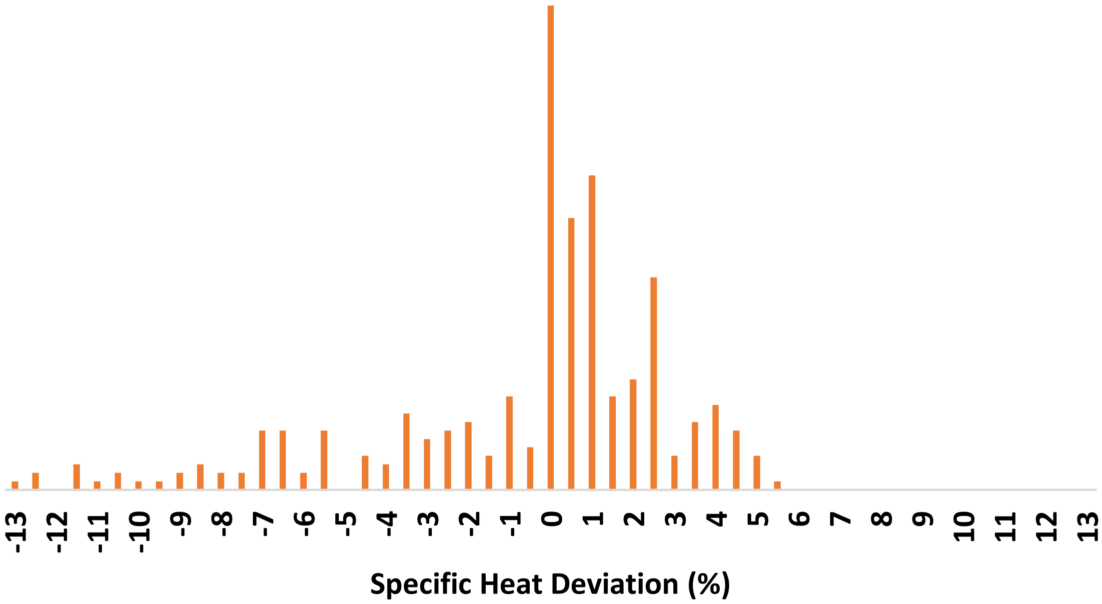

Figure 27: Histogram of the specific heat data for all of the points considered.

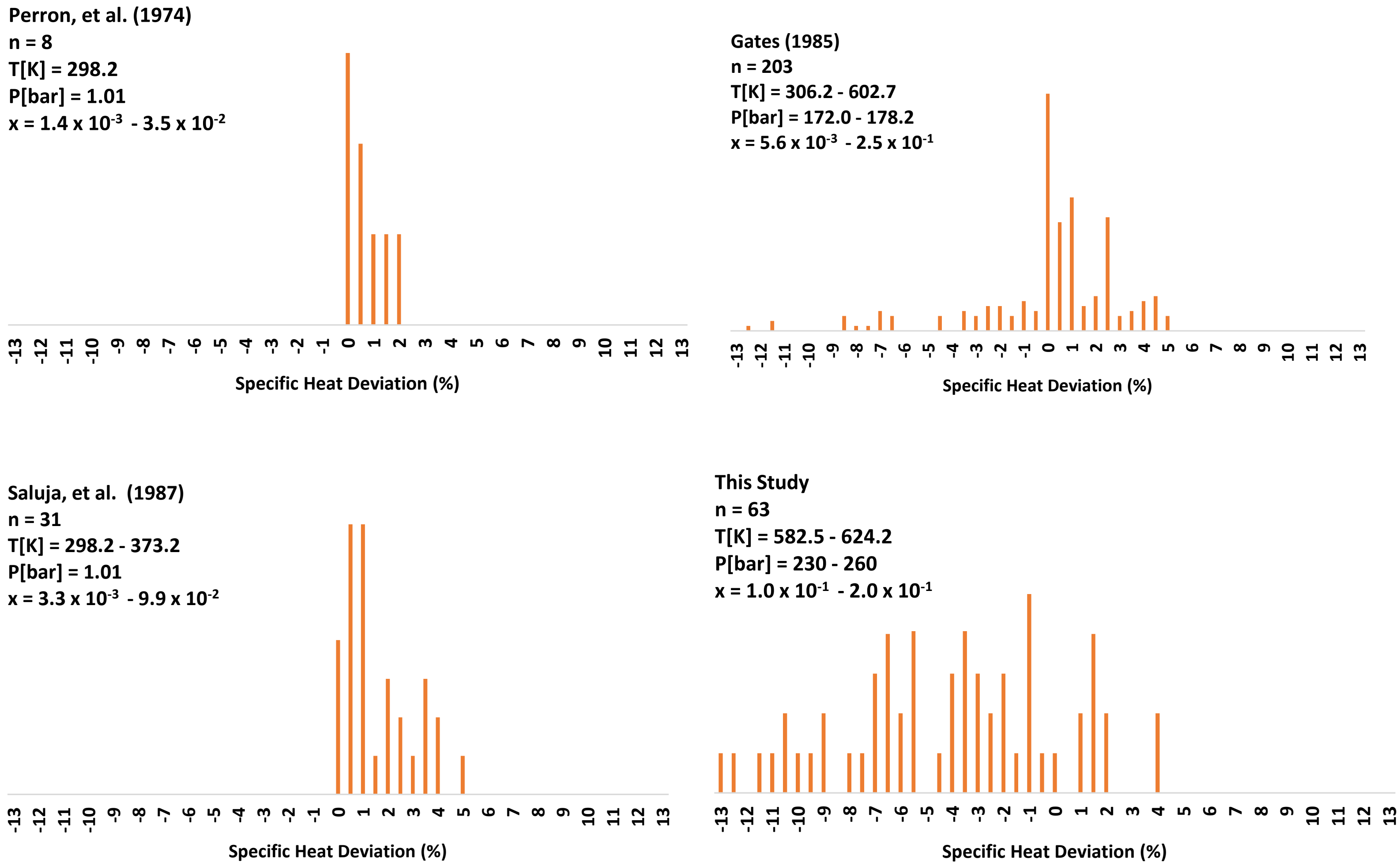

Figure 28: Histograms for studies considered in the specific heat data set.

The remaining data sets are featured in Figure 27 and Figure 28. The fit to ambient temperature data is limited; as with the specific volume correlations, high concentrations of $CaCl_2$ at room temperature produced a T^* that is well below the freezing point of water. There are a total of five data sets, including this study [36], [37], [44], [54], [57]; only two of these [36], [37] featured data above 373 K.

The fit to heat of dilution data was less successful due to the amplification of deviations present at low concentrations (< 0.1 % $CaCl_2$) required for effective measurement. This correlation was able to qualitatively match existing heat of dilution data; a comparison with Holmes, et al. [39] is shown below in Figure 29. For very dilute concentrations, small specific enthalpy deviations can result in large deviations in the heat of dilution; a very small m_2 in Equation 20 resulted in orders of magnitude difference for the heat of dilution.

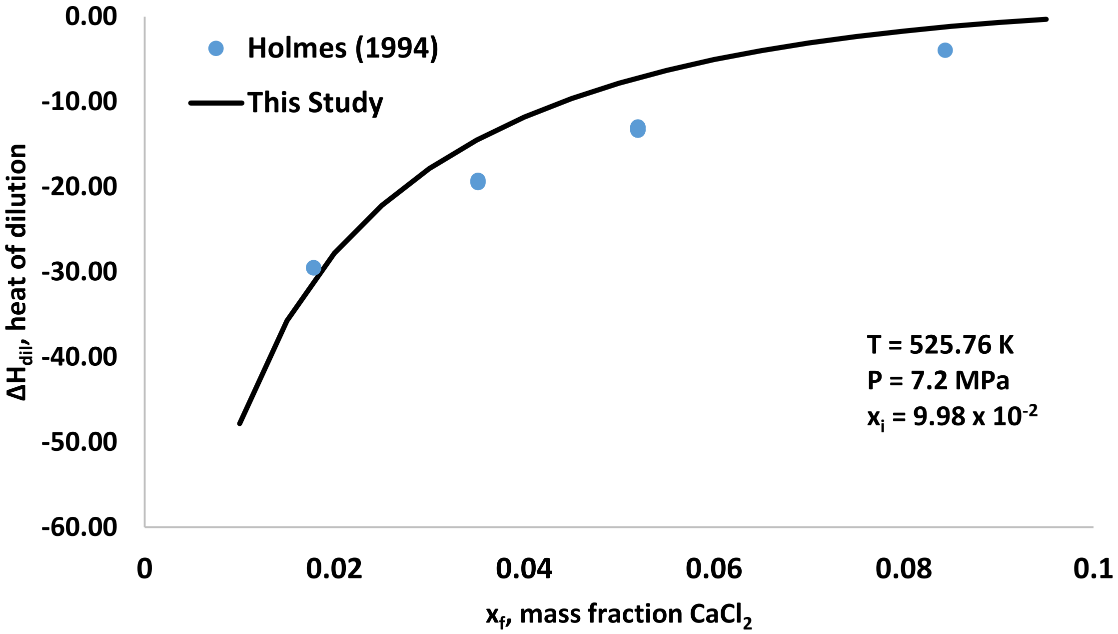

Figure 29: Heats of dilution calculated with Equations 16-18 as compared with a selection of Holmes (1994) [39] data.

CHAPTER 6: CONCLUSIONS

This study was successful in assessing brine treatment costs of the experimentally evaluated Joule-heated desalination system over a variety of process conditions. The process was simulated in Aspen Plus v.10 with user-defined models based upon prior experimental data for the application. Projected brine treatment costs ranged from \$3.49·bbl^{-1} to \$17.28·bbl^{-1}. Treatment costs were highly dependent on process capacity, cost of transportation, cost of sodium carbonate (as a pretreatment chemical) and power sourcing. Additionally, sensitivity to brine composition was considered; high sodium content brines were less costly to treat than brines high in divalent ions (such as Ca^{2+}, Sr^{2+} and Mg^{2+}) which required chemical pretreatment.

The sensitivity analyses around transportation costs suggest this technique could be most effective in remote locations where transportation costs are high. Given the large amount of brine that is currently being transported to disposal/re-injection sites, the Joule-heating desalination system could effectively remove the need for brine transportation, creating a significant environmental impact both in terms of carbon emissions and in the hazards associated with brine transportation and spillage. The greenhouse gas emissions of the transportation of brine would have to be compared with the emissions associated with the treatment method. This additionally removes the environmental issues associated with re-injection, both in danger to the larger water table and in the associated seismic activity.

The combined correlations proved successful at predicting the thermodynamic properties of the $CaCl_2$-H_2O system. The critical pressure, temperature and concentration were evaluated along with vapor-liquid equilibria around the critical line, specific volume and specific enthalpy. In addition, the calorimetric technique described herein was successful at producing specific heat data for the $CaCl_2$-H_2O system around water's critical point, and proved directly useful in furnishing these correlations. These correlations provide some illumination for a previously sporadic set of data at high temperatures – this should prove immediately useful not only for applications associated with produced water with high Ca^{2+} content, but also for geological applications in deep seafloor systems, where temperatures and pressures are high and concentrations of Na^+ and Ca^{2+} far surpass those found in surface seawater systems.

CHAPTER 7: RECOMMENDATIONS

Based on the experimental and simulation results and conclusions drawn from the current research, the following areas can be further investigated in future studies related to this topic:

- The economic model should be validated against further experimental results at pilot scale;
- The correlations from the $CaCl_2$-H_2O system should be used in coordination with NaCl-H_2O data for ternary system behavior for mixed brines, and;
- The calorimeter should be improved for eliminating noise and simplicity.

The economic assessment of the Joule heating method proved successful; however, the model will be unable to predict the advancements in material that will no doubt be made for the novel technique. As the experimental system is developed into a pilot scale process, the model will need to be adapted in order to function at scale. The plugging issues present within the smaller experimental system should be mitigated at scale – once data is made available at the limits of the process, the ZLD potential for the Joule heating system can be re-evaluated. It may not be necessary to have downstream flash vessels; instead, a larger system may be able to achieve ZLD in isolation. I recommend that the limits of a larger system be tested directly with brines similar to those found in earlier papers – the water recoveries should be much higher, and the power requirements expressed in the model can be validated or altered with further experimentation. The above findings suggest the system will be more economically viable at scale; this will, however, need to be balanced with the system's modular advantages in remote areas, where a smaller scale system could be deployed at the site of water production.

In addition, the correlations for the $CaCl_2$-H_2O system were effective in predicting binary solution properties at high temperatures. However, the mixed salt brine encountered in brine is rarely, if ever, comprised of a pure single salt (whether NaCl or $CaCl_2$). Now that the two most prominent salts featured in brine have calculable thermodynamic properties, the next obvious step is to provide data for the ternary system of NaCl-$CaCl_2$-H_2O. However, data for such a system is sparse – this is especially true at higher temperatures. A series of tests will be necessary not only for specific heat data in this region but also densities and phase equilibria that is missing from the ternary system. It is recommend that the density of the mixed salt brine be evaluated at the pressures and temperatures described in earlier chapters (around the critical point of the pure solvent) in order to assess the effect of competing electrolytes in solution and their impact on thermodynamic properties. The methods described in earlier chapters for specific heat should be sufficient for the mixed salt brine as well, and the rugged design of the calorimeter should be able to withstand the mixed salt brine just as easily as the $CaCl_2$-H_2O solution.

Finally, improvements to the calorimeter are recommended. In order to quickly gather data, an AC power source was used from the existing desalination system. A more precise DC power system described in earlier papers on flow calorimetry should be more successful at eliminating noise and producing a result with lower uncertainty than the existing data. In addition, a smaller microcalorimetric system would be much simpler to operate. With these changes, data can be quickly gathered for the two binary solutions ($NaCl$-H_2O and $CaCl_2$-H_2O) and additional mixed salt compositions.

REFERENCES

[1] C. M. Able, D. D. Ogden, and J. P. Trembly, “Sustainable management of hypersaline brine waste: Zero liquid discharge via Joule-heating at supercritical condition,” *Desalination*, vol. 444, pp. 84–93, Oct. 2018, doi: 10.1016/j.desal.2018.07.014.

[2] P. N. Service, “What oil leaves behind in 2.5 billion gallons of water every day in U.S.” https://www.purdue.edu/newsroom/releases/2019/Q1/what-oil-leaves-behind-in-2.5-billion-gallons-of-water-every-day-in-u.s..html (accessed Oct. 03, 2019).

[3] M. S. Blondes, K. D. Gans, E. L. Rowan, J. J. Thordsen, M. E. Reidy, M. A. Engle, Y. K. Kharaka, V. Saraswathula, and E. Morrissey, “US Geological Survey National Produced Waters Geochemical Database v2. 3 (PROVISIONAL) Documentation,” *USGS, December*, 2017.

[4] D. W. Knowles and R. G. Boytim, “Brine Handling And Disposal By Reinjection,” in *SPE/EPA Exploration and Production Environmental Conference*, Houston, Texas, 1995, doi: 10.2118/29763-MS.

[5] C. E. Clark and J. A. Veil, “Produced water volumes and management practices in the United States.,” Argonne National Laboratory (ANL), 2009.

[6] T. Auch and PhD, “The Hidden Inefficiencies and Environmental Costs of Fracking in Ohio,” *FracTracker Alliance*, Jan. 13, 2020. https://www.fractracker.org/2020/01/hidden-inefficiencies-and-environmental-costs-of-fracking-in-ohio/ (accessed May 21, 2020).

[7] A. Bradford, “Produced Water Volumes Climb Driven By Unconventional Oil - BTU Analytics,” *https://btuanalytics.com/*. https://btuanalytics.com/shale-production/produced-water-volumes-climb-driven-by-unconventional-oil/ (accessed May 21, 2020).

[8] A. Wrobetz and J. Gartner, “Wastewater Treatment Technologies in Natural Gas Hydraulic Fracturing: Executive Summary.”

[9] S. G. J. Heijman, H. Guo, S. Li, J. C. van Dijk, and L. P. Wessels, “Zero liquid discharge: Heading for 99% recovery in nanofiltration and reverse osmosis,” *Desalination*, vol. 236, no. 1–3, pp. 357–362, Jan. 2009, doi: 10.1016/j.desal.2007.10.087.

[10] L. F. Greenlee, D. F. Lawler, B. D. Freeman, B. Marrot, and P. Moulin, “Reverse osmosis desalination: Water sources, technology, and today’s challenges,” *Water Research*, vol. 43, no. 9, pp. 2317–2348, May 2009, doi: 10.1016/j.watres.2009.03.010.

[11] R. Y. Ning and T. L. Troyer, “Tandom reverse osmosis process for zero-liquid discharge,” *Desalination*, vol. 237, no. 1–3, pp. 238–242, Feb. 2009, doi: 10.1016/j.desal.2007.11.060.

[12] G. P. Thiel, E. W. Tow, L. D. Banchik, H. W. Chung, and J. H. Lienhard, “Energy consumption in desalinating produced water from shale oil and gas extraction,” *Desalination*, vol. 366, pp. 94–112, Jun. 2015, doi: 10.1016/j.desal.2014.12.038.

[13] R. Kaplan, D. Mamrosh, H. H. Salih, and S. A. Dastgheib, “Assessment of desalination technologies for treatment of a highly saline brine from a potential CO 2 storage site,” *Desalination*, vol. 404, pp. 87–101, Feb. 2017, doi: 10.1016/j.desal.2016.11.018.

[14] S. A. Dastgheib, “An Integrated Supercritical System for Efficient Produced Water Treatment and Power Generation,” DOE-UIUC--0024015, 1462360, Aug. 2018. doi: 10.2172/1462360.

[15] S. van Wyk, S. O. Odu, A. G. J. van der Ham, and S. R. A. Kersten, “Design and results of a first generation pilot plant for supercritical water desalination (SCWD),” *Desalination*, vol. 439, pp. 80–92, Aug. 2018, doi: 10.1016/j.desal.2018.03.028.

[16] S. van Wyk, A. G. J. van der Ham, and S. R. A. Kersten, “Analysis of the energy consumption of supercritical water desalination (SCWD),” *Desalination*, vol. 474, p. 114189, Jan. 2020, doi: 10.1016/j.desal.2019.114189.

[17] D. D. Ogden and J. P. Trembly, “Desalination of hypersaline brines via Joule-heating: Experimental investigations and comparison of results to existing models,” *Desalination*, vol. 424, pp. 149–158, Dec. 2017, doi: 10.1016/j.desal.2017.10.006.

[18] X. Dong, J. Trembly, and D. Bayless, “Techno-economic analysis of hydraulic fracking flowback and produced water treatment in supercritical water reactor,” *Energy*, vol. 133, pp. 777–783, Aug. 2017, doi: 10.1016/j.energy.2017.05.078.

[19] D. E. López and J. P. Trembly, “Desalination of hypersaline brines with joule-heating and chemical pre-treatment: Conceptual design and economics,” *Desalination*, vol. 415, pp. 49–57, Aug. 2017, doi: 10.1016/j.desal.2017.04.003.

[20] O. Yakaboylu, J. Harinck, K. Smit, and W. de Jong, “Supercritical Water Gasification of Biomass: A Literature and Technology Overview,” *Energies*, vol. 8, no. 12, pp. 859–894, Jan. 2015, doi: 10.3390/en8020859.

[21] S. O. Odu, A. G. J. van der Ham, S. Metz, and S. R. A. Kersten, “Design of a Process for Supercritical Water Desalination with Zero Liquid Discharge,” *Industrial & Engineering Chemistry Research*, vol. 54, no. 20, pp. 5527–5535, May 2015, doi: 10.1021/acs.iecr.5b00826.

[22] T. Driesner, “The system H2O–NaCl. Part II: Correlations for molar volume, enthalpy, and isobaric heat capacity from 0 to 1000°C, 1 to 5000bar, and 0 to 1 XNaCl,” *Geochimica et Cosmochimica Acta*, vol. 71, no. 20, pp. 4902–4919, Oct. 2007, doi: 10.1016/j.gca.2007.05.026.

[23] T. Driesner and C. A. Heinrich, “The system H2O–NaCl. Part I: Correlation formulae for phase relations in temperature–pressure–composition space from 0 to 1000°C, 0 to 5000bar, and 0 to 1 XNaCl,” *Geochimica et Cosmochimica Acta*, vol. 71, no. 20, pp. 4880–4901, Oct. 2007, doi: 10.1016/j.gca.2006.01.033.

[24] D. G. Archer, “Thermodynamic properties of the NaCl+ H2O system. II. Thermodynamic properties of NaCl (aq), NaCl· 2H2 (cr), and phase equilibria,” *Journal of Physical and Chemical Reference Data*, vol. 21, no. 4, pp. 793–829, 1992.

[25] A. Anderko and K. S. Pitzer, “Equation-of-state representation of phase equilibria and volumetric properties of the system NaCl-H2O above 573 K,” *Geochimica et Cosmochimica Acta*, vol. 57, no. 8, pp. 1657–1680, Apr. 1993, doi: 10.1016/0016-7037(93)90105-6.

[26] J. C. Tanger IV and K. S. Pitzer, “Thermodynamics of NaCl-H2O: A new equation of state for the near-critical region and comparisons with other equations for adjoining regions,” *Geochimica et Cosmochimica Acta*, vol. 53, no. 5, pp. 973–987, 1989.

[27] S. Jiang and K. S. Pitzer, “Phase equilibria and volumetric properties of aqueous CACl2 by an equation of state,” *AIChE J.*, vol. 42, no. 2, pp. 585–594, Feb. 1996, doi: 10.1002/aic.690420227.

[28] Z. Duan, N. Moller, and J. H. Weare, “A high temperature equation of state for the H2O-CaCl2 and H2O-MgCl2 systems,” *Geochimica et Cosmochimica Acta*, vol. 70, no. 15, pp. 3765–3777, Aug. 2006, doi: 10.1016/j.gca.2006.05.007.

[29] I. Pioro and S. Mokry, “Thermophysical Properties at Critical and Supercritical Conditions,” *Heat Transfer*, p. 22.

[30] J. L. Bischoff and K. S. Pitzer, “Liquid-vapor relations for the system NaCl-H2O: summary of the P-T- x surface from 300° to 500°C,” *American Journal of Science*, vol. 289, no. 3, pp. 217–248, 1989.

[31] J. L. Bischoff, R. J. Rosenbauer, and K. S. Pitzer, “The system NaCl-H2O: Relations of vapor-liquid near the critical temperature of water and of vapor-liquid-halite from 300 to 500 C,” *Geochimica et Cosmochimica Acta*, vol. 50, no. 7, pp. 1437–1444, 1986.

[32] C. S. Oakes, R. J. Bodnar, J. M. Simonson, and K. S. Pitzer, “Critical and supercritical properties for 0.3 to 3.0 mol· kg- 1 CaCl2 (aq),” *Geochimica et cosmochimica acta*, vol. 58, no. 11, pp. 2421–2431, 1994.

[33] C. S. Oakes, R. J. Bodnar, J. M. Simonson, and K. S. Pitzer, “CaCl 2-H 2 O in the supercritical and two-phase ranges,” *International journal of thermophysics*, vol. 16, no. 2, pp. 483–492, 1995.

[34] J. L. Bischoff, R. J. Rosenbauer, and R. O. Fournier, “The generation of HCl in the system CaCl2-H2O: Vapor-liquid relations from 380–500 C,” *Geochimica et Cosmochimica Acta*, vol. 60, no. 1, pp. 7–16, 1996.

[35] S. I. Tkachenko and K. Shmulovich, “Liquid-vapor equilibria in water-salt systems (NaCl, KCl, CaCl 2, MgCl 2) at 400–600 C,” in *Dokl Akad SSSR*, 1992, vol. 326, pp. 1055–1059.

[36] J. A. Gates, “Thermodynamics of aqueous electrolyte solutions at high temperatures and pressures,” PhD Thesis, University of Delaware, 1985.

[37] D. E. White, A. L. Doberstein, J. A. Gates, D. M. Tillett, and R. H. Wood, “Heat capacity of aqueous CaCl2 from 306 to 603 K at 17.5 MPa,” *The Journal of Chemical Thermodynamics*, vol. 19, no. 3, pp. 251–259, 1987.

[38] J. M. Simonson, R. H. Busey, and R. E. Mesmer, “Enthalpies of dilution of aqueous calcium chloride to low molalities at high temperatures,” *J. Phys. Chem.*, vol. 89, no. 4, pp. 557–560, Feb. 1985, doi: 10.1021/j100250a001.

[39] H. F. Holmes, R. H. Busey, J. M. Simonson, and R. E. Mesmer, “CaCl2 (aq) at elevated temperatures. Enthalpies of dilution, isopiestic molalities, and thermodynamic properties,” *The Journal of Chemical Thermodynamics*, vol. 26, no. 3, pp. 271–298, 1994.

[40] S. V. Tsay, V. N. Gilyarov, V. I. Zarembo, and L. V. Puchkov, “Bulk Properties of Aqueous Calcium Chloride at High State Parameters,” *Geochemistry International*, vol. 26, no. 1–4, p. 52, 1989.

[41] R. Crovetto, S. N. Lvov, and R. H. Wood, “Vapor pressures and densities of NaCl (aq) and KCl (aq) at the temperature 623 K and CaCl2 (aq) at the temperatures 623 K and 643 K,” *The Journal of Chemical Thermodynamics*, vol. 25, no. 1, pp. 127–138, 1993.

[42] J. A. Gates and R. H. Wood, “Density and apparent molar volume of aqueous calcium chloride at 323-600 K,” *Journal of Chemical and Engineering Data*, vol. 34, no. 1, pp. 53–56, 1989.

[43] A. Kumar, “Densities and apparent molal volumes of aqueous concentrated calcium chloride solutions from 50 to 200 C at 20.27 bar,” *Journal of solution chemistry*, vol. 15, no. 5, pp. 409–412, 1986.

[44] G. Perron, J. E. Desnoyers, and F. J. Millero, “Apparent Molal Volumes and Heat Capacities of Alkaline Earth Chlorides in Water at 25 °C,” *Can. J. Chem.*, vol. 52, no. 22, pp. 3738–3741, Nov. 1974, doi: 10.1139/v74-558.

[45] S. Al Ghafri, G. C. Maitland, and J. P. M. Trusler, “Densities of Aqueous $MgCl_2$ (aq), $CaCl_2$ (aq), KI(aq), NaCl(aq), KCl(aq), $AlCl_3$ (aq), and (0.964 NaCl + 0.136 KCl)(aq) at Temperatures Between (283 and 472) K, Pressures up to 68.5 MPa, and Molalities up to 6 mol·kg^{-1},” *J. Chem. Eng. Data*, vol. 57, no. 4, pp. 1288–1304, Apr. 2012, doi: 10.1021/je2013704.

[46] J. M. Wimby and T. S. Berntsson, “Viscosity and density of aqueous solutions of lithium bromide, lithium chloride, zinc bromide, calcium chloride and lithium nitrate. 1. Single salt solutions,” *J. Chem. Eng. Data*, vol. 39, no. 1, pp. 68–72, Jan. 1994, doi: 10.1021/je00013a019.

[47] Z. Yan, J. Wang, W. Kong, and J. Lu, “Effect of temperature on volumetric and viscosity properties of some ⎵-amino acids in aqueous calcium chloride solutions,” *Fluid Phase Equilibria*, p. 8, 2004.

[48] J. T. Safarov, G. N. Najafov, A. N. Shahverdiyev, and E. Hassel, “(p,ρ,T) and (ps,ρs,Ts) properties, and apparent molar volumes Vϕ of CaCl2 (aq) at T=298.15 to 398.15 K and at pressures up to p=60 MPa,” *Journal of Molecular Liquids*, vol. 116, no. 3, pp. 165–174, Feb. 2005, doi: 10.1016/j.molliq.2004.07.083.

[49] H.-L. Zhang, G.-H. Chen, and S.-J. Han, “Viscosity and density of H2O+ NaCl+ CaCl2 and H2O+ KCl+ CaCl2 at 298.15 K,” *Journal of Chemical & Engineering Data*, vol. 42, no. 3, pp. 526–530, 1997.

[50] J. Kiepe, A. Karine de Araújo Rodrigues, S. Horstmann, and J. Gmehling, “Experimental Determination and Correlation of Liquid Density Data of Electrolyte Mixtures Containing Water or Methanol,” *Ind. Eng. Chem. Res.*, vol. 42, no. 9, pp. 2022–2029, Apr. 2003, doi: 10.1021/ie020936b.

[51] A. Kumar and G. Atkinson, “Thermodynamics of concentrated electrolyte mixtures. 3. Apparent molal volumes, compressibilities, and expansibilities of sodium chloride-calcium chloride mixtures from 5 to 35.degree.C,” *J. Phys. Chem.*, vol. 87, no. 26, pp. 5504–5507, Dec. 1983, doi: 10.1021/j150644a039.

[52] L. A. Romankiw and I. M. Chou, “Densities of aqueous sodium chloride, potassium chloride, magnesium chloride, and calcium chloride binary solutions in the concentration range 0.5-6.1 m at 25, 30, 35, 40, and 45.degree.C,” *J. Chem. Eng. Data*, vol. 28, no. 3, pp. 300–305, Jul. 1983, doi: 10.1021/je00033a005.

[53] T. Isono, “Density, viscosity, and electrolytic conductivity of concentrated aqueous electrolyte solutions at several temperatures. Alkaline-earth chlorides, lanthanum chloride, sodium chloride, sodium nitrate, sodium bromide, potassium nitrate, potassium bromide, and cadmium nitrate,” *J. Chem. Eng. Data*, vol. 29, no. 1, pp. 45–52, Jan. 1984, doi: 10.1021/je00035a016.

[54] P. P. S. Saluja and J. C. LeBlanc, “Apparent molar heat capacities and volumes of aqueous solutions of magnesium chloride, calcium chloride, and strontium chloride

at elevated temperatures,” *J. Chem. Eng. Data*, vol. 32, no. 1, pp. 72–76, Jan. 1987, doi: 10.1021/je00047a021.

[55] A. J. Ellis, “Partial molal volumes of MgCl 2, CaCl 2, SrCl 2, and BaCl 2 in aqueous solution to 200°,” *Journal of the Chemical Society A: Inorganic, Physical, Theoretical*, pp. 660–664, 1967.

[56] F. J. Millero, G. K. Ward, and P. V. Chetirkin, “Relative sound velocities of sea salts at 25°C,” *The Journal of the Acoustical Society of America*, vol. 61, no. 6, pp. 1492–1498, Jun. 1977, doi: 10.1121/1.381449.

[57] G. Perron, A. Roux, and J. E. Desnoyers, “Heat capacities and volumes of NaCl, $MgCl_2$, $CaCl_2$, and $NiCl_2$ up to 6 molal in water,” *Can. J. Chem.*, vol. 59, no. 21, pp. 3049–3054, Nov. 1981, doi: 10.1139/v81-446.

[58] A. Kumar, G. Atkinson, and R. D. Howell, “Thermodynamics of concentrated electrolyte mixtures. II. Densities and compressibilities of aqueous NaCl- CaCl 2 at 25° C,” *Journal of Solution Chemistry*, vol. 11, no. 12, pp. 857–870, 1982.

[59] K. S. Pitzer, “Thermodynamics of electrolytes. I. Theoretical basis and general equations,” *The Journal of Physical Chemistry*, vol. 77, no. 2, pp. 268–277, 1973.

[60] K. S. Pitzer, “Thermodynamics of natural and industrial waters,” *The Journal of Chemical Thermodynamics*, vol. 25, no. 1, pp. 7–26, 1993.

[61] J. L. Oscarson, B. Liu, and R. M. Izatt, “A Model Incorporating Ion Dissociation, Solute Concentration, and Solution Density Effects To Describe the Thermodynamics of Aqueous Sodium Chloride Solutions in the Critical Region of Water,” *Industrial & Engineering Chemistry Research*, vol. 43, no. 23, pp. 7635–7646, Nov. 2004, doi: 10.1021/ie040112p.

[62] J. L. Oscarson, B. A. Palmer, S. Fuangswasdi, and R. M. Izatt, “A New Model Incorporating Ion Dissociation for Sodium Chloride Solutions near the Critical Point of Water,” *Industrial & Engineering Chemistry Research*, vol. 40, no. 9, pp. 2176–2182, May 2001, doi: 10.1021/ie000930r.

[63] A. A. Afanasyev, “Modeling of Multiphase Thermodynamic Equilibria of NaCl–H 2 O Binary Mixture in a Wide Range of Pressures and Temperatures,” *High Temperature*, vol. 56, no. 6, pp. 859–866, 2018.

[64] Y. Cohen, R. Semiat, and A. Rahardianto, “A perspective on reverse osmosis water desalination: Quest for sustainability,” *AIChE Journal*, vol. 63, no. 6, pp. 1771–1784, 2017, doi: 10.1002/aic.15726.

[65] D. L. Shaffer, L. H. Arias Chavez, M. Ben-Sasson, S. Romero-Vargas Castrillón, N. Y. Yip, and M. Elimelech, “Desalination and Reuse of High-Salinity Shale Gas Produced Water: Drivers, Technologies, and Future Directions,” *Environmental Science & Technology*, vol. 47, no. 17, pp. 9569–9583, Sep. 2013, doi: 10.1021/es401966e.

[66] A. Al-Karaghouli and L. L. Kazmerski, “Energy consumption and water production cost of conventional and renewable-energy-powered desalination processes,” *Renewable and Sustainable Energy Reviews*, vol. 24, pp. 343–356, Aug. 2013, doi: 10.1016/j.rser.2012.12.064.

[67] R. L. McGinnis, N. T. Hancock, M. S. Nowosielski-Slepowron, and G. D. McGurgan, “Pilot demonstration of the NH3/CO2 forward osmosis desalination process on high salinity brines,” *Desalination*, vol. 312, pp. 67–74, Mar. 2013, doi: 10.1016/j.desal.2012.11.032.

[68] A. Alkhudhiri, N. Darwish, and N. Hilal, “Produced water treatment: Application of Air Gap Membrane Distillation,” *Desalination*, vol. 309, pp. 46–51, Jan. 2013, doi: 10.1016/j.desal.2012.09.017.

[69] “SaltMaker MultiEffect Evaporator Crystallizer | Saltworks Technologies,” *Saltworks Techologies*. https://www.saltworkstech.com/technology/saltmaker-evaporator-crystallizer/ (accessed Oct. 09, 2019).

[70] R. H. Busey, H. F. Holmes, and R. E. Mesmer, “The enthalpy of dilution of aqueous sodium chloride to 673 K using a new heat-flow and liquid-flow microcalorimeter. Excess thermodynamic properties and their pressure coefficients,” *The Journal of Chemical Thermodynamics*, vol. 16, no. 4, pp. 343–372, 1984.

[71] C. J. Peterson, “A new model for aqueous electrolyte solutions near the critical point of water incorporating aqueous reaction equilibria,” Ph.D., Brigham Young University, United States -- Utah, 2009.

[72] D. Smith-Magowan, “The measurement of heat capacities of aqueous electrolytes at elevated temperatures and pressures using a new flow calorimeter.,” 1981.

[73] P. Picker, P.-A. Leduc, P. R. Philip, and J. E. Desnoyers, “Heat capacity of solutions by flow microcalorimetry,” *The Journal of Chemical Thermodynamics*, vol. 3, no. 5, pp. 631–642, Sep. 1971, doi: 10.1016/S0021-9614(71)80084-8.

[74] L. Hnědkovský, V. Hynek, V. Majer, and R. H. Wood, “A new version of differential flow heat capacity calorimeter; tests of heat loss corrections and heat capacities of aqueous NaCl from T= 300 K to T= 623 K,” *The Journal of Chemical Thermodynamics*, vol. 34, no. 6, pp. 755–782, Jun. 2002, doi: 10.1006/jcht.2001.0949.

[75] X. Dong, “Techno-Economic Analysis of a Cost-Effective Treatment of Flowback and Produced Waters via an Integrated Precipitative Supercritical Process,” Ohio University, 2015.

[76] J. Cogan, “The Removal of Barium, Strontium, Calcium and Magnesium from Hydraulic Fracturing Produced Water Using Precipitation with Traditional and Alternative Reactant Feedstocks,” Ohio University, 2016.

[77] "Sales & Distribution | Texas Brine Company, LLC," *TexasBrine*, Nov. 04, 2017. https://www.texasbrine.com/our-services/brine-sales-and-distribution (accessed Nov. 21, 2018).

[78] Intrepid Fluids, "Intrepid Fluids Spec Sheet - 10 lb Brine with K-Control." http://www.intrepidpotash.com/wp-content/uploads/2017/02/Spec-Sheet-10-LB-Brine-8-3-17.pdf (accessed Jul. 26, 2019).

[79] W. Fan, B. Liberati, M. Novak, M. Cooper, N. Kruse, D. Young, and J. Trembly, "Radium-226 Removal from Simulated Produced Water Using Natural Zeolite and Ion-Exchange Resin," *Industrial & Engineering Chemistry Research*, vol. 55, no. 48, pp. 12502–12505, Dec. 2016, doi: 10.1021/acs.iecr.6b03230.

[80] X. Tang, S. Wang, D. Xu, Y. Gong, J. Zhang, and Y. Wang, "Corrosion Behavior of Ni-Based Alloys in Supercritical Water Containing High Concentrations of Salt and Oxygen," *Ind. Eng. Chem. Res.*, vol. 52, no. 51, pp. 18241–18250, Dec. 2013, doi: 10.1021/ie401258k.

[81] US Bureau of Labor Statistics, "March 2019 PPI Detailed Report," [Online]. Available: https://www.bls.gov/ppi/ppidr201903.pdf.

[82] US Department of the Interior., "Mineral Commodity Summaries 2015," [Online]. Available: https://s3-us-west-2.amazonaws.com/prd-wret/assets/palladium/production/mineral-pubs/mcs/mcs2015.pdf.

[83] R. Turton, *Analysis, Synthesis, and Design of Chemical Processes*. Prentice Hall, 2009.

[84] "Chemical Engineering Plant Cost Index: 2018 Annual Value - Chemical Engineering | Page 1." https://www.chemengonline.com/2019-cepci-updates-january-prelim-and-december-2018-final/?printmode=1 (accessed Jul. 26, 2019).

[85] R. McCurdy and C. E. Corporation, "Underground Injection Wells for Produced Water Disposal," [Online]. Available: https://www.epa.gov/sites/production/files/documents/21_McCurdy_-_UIC_Disposal_508.pdf.

[86] "EIA - Electricity Data." https://www.eia.gov/electricity/monthly/epm_table_grapher.php?t=epmt_5_6_a (accessed Jul. 26, 2019).

[87] "Henry Hub Natural Gas Prices to Average $2.99 This Year, $3.08 in 2019, EIA Says." https://www.naturalgasintel.com/articles/114687-henry-hub-natural-gas-prices-to-average-299-this-year-308-in-2019-eia-says?v=preview (accessed Jul. 26, 2019).

[88] M. Wenzlick, N. Siefert, and A. Hakala, "Tailoring Treated Brines for Reuse Scenarios," presented at the SPE/AAPG/SEG Unconventional Resources Technology Conference, Aug. 2018, doi: 10.15530/URTEC-2018-2902572.

[89] “Salt Statistics and Information.” https://www.usgs.gov/centers/nmic/salt-statistics-and-information (accessed Oct. 05, 2019).

[90] “Archived Producer Price Index Detailed Report Information.” https://www.bls.gov/ppi/ppi_dr.htm (accessed Nov. 21, 2018).

[91] “Argus Sulphuric Acid | Argus Media.” https://www.argusmedia.com/en/fertilizer/argus-sulphuric-acid?page=1 (accessed Nov. 21, 2018).

[92] B. Bowen, “OUTLOOK ’18: US caustic soda could push higher on restricted global supply,” *Icis*. https://www.icis.com/explore/resources/news/2018/01/03/10172550/outlook-18-us-caustic-soda-could-push-higher-on-restricted-global-supply (accessed Jul. 26, 2019).

[93] M. Hindi, “US 2019 soda ash prices increase amid globally short supply,” *Icis*. https://www.icis.com/explore/resources/news/2019/01/15/10306648/us-2019-soda-ash-prices-increase-amid-globally-short-supply (accessed Jul. 26, 2019).

[94] “West Virginia - May 2018 OES State Occupational Employment and Wage Estimates.” https://www.bls.gov/oes/current/oes_wv.htm#51-0000 (accessed Jul. 26, 2019).

[95] H. Zhao, G. F. Vance, G. K. Ganjegunte, and M. A. Urynowicz, “Use of zeolites for treating natural gas co-produced waters in Wyoming, USA,” *Desalination*, vol. 228, no. 1, pp. 263–276, Aug. 2008, doi: 10.1016/j.desal.2007.08.014.

[96] “Food Grade Best Price Per Ton Clinoptilolite Natural Zeolite - Buy Zeolite Price Per Ton,Clinoptilolite Natural Zeolite,Zeolite Food Grade Product on Alibaba.com,” *www.alibaba.com*. //www.alibaba.com/product-detail/Food-Grade-Best-Price-Per-Ton_60804243464.html (accessed Jul. 26, 2019).

[97] M. S. Blondes, K. D. Gans, E. L. Rowan, J. J. Thordsen, M. E. Reidy, M. A. Engle, Y. K. Kharaka, V. Saraswathula, and E. Morrissey, “US Geological Survey National Produced Waters Geochemical Database v2. 3 (PROVISIONAL) Documentation,” *USGS, December*, 2017.

[98] P. Virtanen, R. Gommers, T. E. Oliphant, M. Haberland, T. Reddy, D. Cournapeau, E. Burovski, P. Peterson, W. Weckesser, and J. Bright, “SciPy 1.0: fundamental algorithms for scientific computing in Python,” *Nature methods*, pp. 1–12, 2020.

[99] M. Newville, T. Stensitzki, D. B. Allen, and A. Ingargiola, “LMFIT: Non-Linear Least-Square Minimization and Curve-Fitting for Python. Zenodo (2014),” *There is no corresponding record for this reference.[Google Scholar]*.

[100] jjgomera, *iapws: Python implementation of standards from The InternationalAssociation for the Properties of Water and Steam*. .

[101] O. S. Center, *Ohio supercomputer center*. 1987.

[102] N. O. of D. and Informatics, “NIST Chemistry WebBook.” https://webbook.nist.gov/chemistry/ (accessed Mar. 30, 2020).

[103] S. Mondal and S. R. Wickramasinghe, “Produced water treatment by nanofiltration and reverse osmosis membranes,” *Journal of Membrane Science*, vol. 322, no. 1, pp. 162–170, Sep. 2008, doi: 10.1016/j.memsci.2008.05.039.

[104] K. L. Hickenbottom, N. T. Hancock, N. R. Hutchings, E. W. Appleton, E. G. Beaudry, P. Xu, and T. Y. Cath, “Forward osmosis treatment of drilling mud and fracturing wastewater from oil and gas operations,” *Desalination*, vol. 312, pp. 60–66, Mar. 2013, doi: 10.1016/j.desal.2012.05.037.

[105] Y. Shibue, “Vapor pressures of aqueous NaCl and CaCl2 solutions at elevated temperatures,” *Fluid Phase Equilibria*, vol. 213, no. 1–2, pp. 39–51, Oct. 2003, doi: 10.1016/S0378-3812(03)00284-X.

[106] J. M. H. Levelt Sengers, “Dilute mixtures and solutions near critical points,” *Fluid Phase Equilibria*, vol. 30, pp. 31–39, Jan. 1986, doi: 10.1016/0378-3812(86)80038-3.

[107] “Nickel Alloy Hastelloy C-276 UNS N10276,” *http://www.hysuperalloy.com/*. http://hysuperalloy.com/nickel-alloy-hastelloy-c-276-uns-n10276.html (accessed Oct. 15, 2019).

[108] “TC4676IW | 500 Gallon Plastic Water Storage Tank Chemtainer.” https://www.plastic-mart.com/product/3448/500-gallon-water-tank-chemtainer-tc4676iw (accessed Oct. 14, 2019).

[109] “BPVC Code Cases: Boiler & Pressure Vessels - ASME.” https://www.asme.org/codes-standards/find-codes-standards/bpvc-cc-bpv-bpvc-code-cases-boilers-pressure-vessels (accessed Oct. 15, 2019).

[110] “Haynes International - Principal Features.” https://www.haynesintl.com/alloys/alloy-portfolio_/Corrosion-resistant-Alloys/HASTELLOY-C-276-Alloy (accessed Oct. 15, 2019).

[111] Mott. Souders and G. Granger. Brown, “Design of Fractionating Columns I. Entrainment and Capacity,” *Ind. Eng. Chem.*, vol. 26, no. 1, pp. 98–103, Jan. 1934, doi: 10.1021/ie50289a025.

[112] D. PR, “GPSA Midstream Suppliers,” *GPSA Midstream Suppliers*. https://gpsamidstreamsuppliers.org/ (accessed Oct. 15, 2019).

[113] D. R. White and C. J. Downes, “Heat loss corrections for heat capacity flow calorimeters,” *Journal of Solution Chemistry*, vol. 17, no. 8, pp. 733–750, Aug. 1988, doi: 10.1007/BF00647419.

[114] P. S. Z. Rogers and C. J. Duffy, “Comparison of calibration methods for flow heat-capacity calorimeters and heat capacities of concentrated NaCl(aq) to 598 Ka,” p. 20.

APPENDIX A: PRODUCTS FORMED

Table S1: The products formed from each case.

Brine Concentration	**Zero Liquid Discharge**
Suspended solids/oil	Suspended solids/oil
Hydroxides (Magnesium)	Hydroxides (Magnesium and Calcium)
Clean water	Sulfates (Barium and Strontium)
Concentrated brine (all ions save Magnesium)	Carbonates (Calcium and Strontium)
Drilling Fluid	NORM (adsorbed onto clinoptilolite)
	Clean water
	Chloride product (sodium, potassium, calcium)
	Rock Salt

APPENDIX B: INDIVIDUAL COST BREAKDOWN

Table S2: Bare module cost factors used for ZLD case equipment costing [83]. Equipment cost based upon vendor quotes features the appropriate citation.

Equip	A	P	K1	K2	K3	C1	C2	C3	B1	B2	Fm
SCWD											
(as pressure vessel)	0.248	300	3.4974	0.4485	0.1074	-	-	-	2.25	1.82	4.8
(control valves) [75]	-	-	-	-	-	-	-	-	-	-	-
(electrode cost) [107]	-	-	-	-	-	-	-	-	-	-	-
HX	40.7	300	3.9912	0.0668	0.243	-0.4045	0.1859	0	1.74	1.55	3.7
Sulf											
(hydrocyclone) [75]	-	-	-	-	-	-	-	-	-	-	-
(holding tank) [108]	-	-	-	-	-	-	-	-	-	-	-
(pump)	4.08	3.40	3.3892	0.0536	0.1538	-0.3935	0.3957	-0.00226	1.89	1.35	2.5
Soft											

Table S2 Continued

(hydrocyclone) [75]	-	-	-	-	-	-	-	-	-	-	-
(holding tank) [108]	-	-	-	-	-	-	-	-	-	-	-
(pump)	4.08	3.40	3.3892	0.0536	0.1538	-0.3935	0.3957	-0.00226	1.89	1.35	2.5
Hydro											
(hydrocyclone) [75]	-	-	-	-	-	-	-	-	-	-	-
(holding tank) [108]	-	-	-	-	-	-	-	-	-	-	-
(pump)	2.93	3.40	3.3892	0.0536	0.1538	-0.3935	0.3957	-0.00226	1.89	1.35	2.5
HP Pump [75]	-	-	-	-	-	-	-	-	-	-	-
Flash											
10 Bar	1.62	9	3.5565	0.3776	0.0905	-	-	-	1.49	1.52	4.8
1 Bar	0.62	0	3.4974	0.4485	0.1074	-	-	-	2.25	1.82	4.8
(flash control valves) [75]	-	-	-	-	-	-	-	-	-	-	-
NORM											

Table S2 Continued

(as pressure vessel)	2.70	3.40	3.5565	0.3776	0.0905	-	-	-	1.49	1.52	1.7
(tower packing)	0.804	3.40	2.4493	0.9744	0.0055	-	-	-	-	-	4.1
(pump)	4.08	3.40	3.3892	0.0536	0.1538	-0.3935	0.3957	-0.00226	1.89	1.35	2.5
Sand											
(sand filter) [75]	-	-	-	-	-	-	-	-	-	-	-
(pump)	4.08	3.40	3.3892	0.0536	0.1538	-0.3935	0.3957	-0.00226	1.89	1.35	2.5
UV [75]	-	-	-	-	-	-	-	-	-	-	-
Generator [75]	-	-	-	-	-	-	-	-	-	-	-
Cool	86.8	1	4.3247	-0.303	0.1634	0.03881	-0.11272	0.08183	1.63	1.66	1

The design of the supercritical water desalination system itself bypassed Aspen Plus entirely; instead, the existing reactor design [17] was scaled appropriately to a much larger vessel volume. The vessel itself was costed as a pressure vessel comprised of a high Ni-alloy with a maximum pressure rating of 300 barg. Once the required inner volume was found, the scaled height and diameter of the system were used in conjunction with ASME boiler and pressure vessel codes [109] to determine vessel thickness. These equations are listed here:

$$t = \frac{PR}{SE-0.6P}\ ,\ \frac{PR}{2SE+0.4P} \qquad \text{(S1)}$$

In Equation S1, P is the pressure rating (chosen as 300 barg), R is the radius (in inches), S is the ultimate tensile strength of the material (chosen as 98,800 psi based on Haynes International documentation for HC-276 [110]) and E is the joint efficiency (chosen as 0.9). The larger of the two thicknesses was used to determine the vessel thickness as an appropriate safety measure. Assuming the existing reactor design can successfully treat 300 $mL \cdot min^{-1}$, the reactor volume necessary for treating 100 GPM would have to be roughly 0.25 m^3. The authors believe that the existing design can handle higher throughputs - this constraint is merely a limitation of the pump used in the existing design. As the higher throughput is not yet confirmed, this conservative estimate is used to scale the existing design.

The electrode was scaled in a similar manner along with the outer vessel, shifting the length and diameter of the electrode to appropriately reflect the new height and inner diameter of the outer vessel. Using this method, the volume of the electrode was found to be 0.024 m^3, roughly 1/10th of the volume of the vessel itself. Costing the electrode was done merely by taking the expected mass of HC-276 in the electrode (using the density value found from Haynes International [110]) and costing it appropriately per kilogram.

The range for HC-276 was found to be \$25-80 per kilogram [107]; the high value of \$80 per kilogram was used for costing the electrode.

The existing system uses two control valves to modulate both the vapor and liquid flow rates depending on pressure and resistance requirements within the system. Quotes for these control valves were furnished in 2014 [75] and were scaled appropriately to 2018 values. With these three costs combined, the total C_{BM} for the SCWD system was found to be \$249,000.

The ZLD case utilizes two flash vessels for the liquid effluent from the SCWD system. The system uses the heat from the steam in the 10 bar flash vessel in order to dry the salt product in the 1 bar flash vessel; this is shown to be thermodynamically viable [1], [15] regardless of effluent concentration and is not processed through Aspen. The overall volume of the vessel was estimated using the inlet flow rates with an assumed 5 minutes of holdup time. The diameters of these flash vessels were estimated using the Souders-Brown equation [111] which is used to calculate the maximum vapor velocity based on the difference in liquid and vapor densities:

$$v = k\sqrt{\frac{\rho_L - \rho_V}{\rho_V}} \qquad \text{(S2)}$$

In Equation S2, k is assumed to be 0.0535 for a system lacking a demister pad based on GPSA Engineering Data Book [112] factors. Once the vapor velocity is known, the diameter is determined using the following relation in Equation S3:

$$D = \left(\frac{4}{\pi} * \left(\frac{Q_V}{v}\right)\right)^{0.5} \qquad \text{(S3)}$$

Here, Q_V is the vapor flow rate and D is the required vessel diameter. Using the volume and diameter, the length/height of the flash vessel could also be calculated; the relationship between L and D was used to determine if the vessel should be horizontal or vertical. A table for these values is found below.

Table S3: Values for flash vessel calculations.

Pressure (bar)	10	1
ρ_L (kg·m^{-3})	1200	2160
ρ_V (kg·m^{-3})	5.15	0.590
Q_V (m^3·s^{-1})	0.188	2.34
Q_i (m^3·s^{-1})	5.40 x 10^{-3}	2.08 x 10^{-3}
V (m^3)	1.62	0.622
L (m)	7.03	0.860
D (m)	0.542	0.960

Additionally, a control valve for each flash vessel was required in order to modulate pressure – these are costed identically to the control valves used in the SCWD design above [75].

Using the total cost, an annual interest rate of 5% and a 9.5 year lifetime, the annual payment can be calculated as follows [83]:

$$Annual\ Payment = C_{BM} * \frac{i(1+i)^n}{(1+i)^n - 1}$$

Here, i is the interest rate (0.05) and n is the number of years.

Table S4: ZLD case equipment capital costs, bare module cost (CBM) and total module cost (CTM).

	Total Cost	Cost·yr^{-1}	Annual Payment·yr^{-1}
SCWR	$ 249,000	$ 26,000	$ 34,000
HX	$ 672,000	$ 71,000	$ 91,000
Sulf	$ 27,000	$ 3,000	$ 4,000
Soft	$ 25,000	$ 3,000	$ 3,000
Hydro	$ 27,000	$ 3,000	$ 4,000
Pump	$ 233,000	$ 24,000	$ 31,000
Flash	$ 131,000	$ 14,000	$ 18,000
NORM	$ 59,000	$ 6,000	$ 8,000
Sand	$ 25,000	$ 3,000	$ 3,000
UV	$ 16,000	$ 2,000	$ 2,000
Generator	$ 1,025,000	$ 108,000	$ 138,000
Cool	$ 112,000	$ 12,000	$ 15,000
Total (CBM)	**$ 2,599,000**	**$ 274,000**	**$ 350,000**
Total (CTM)	**$ 3,067,000**	**$ 323,000**	**$ 413,000**

Table S5: Brine concentration case equipment capital costs, bare module cost (CBM) and total module cost (CTM).

	Total Cost	Cost·yr^{-1}	Annual Payment·yr^{-1}
SCWR	$ 249,000	$ 26,000	$ 34,000
HX0	$ 588,000	$ 62,000	$ 79,000
HX1	$ 432,000	$ 45,000	$ 58,000
Hydro	$ 27,000	$ 3,000	$ 4,000
Pump	$ 233,000	$ 24,000	$ 31,000
Sand	$ 25,000	$ 3,000	$3,000
UV	$ 16,000	$ 2,000	$2,000
Generator	$ 1,060,000	$ 112,000	$ 143,000
Cool	$ 108,000	$ 11,000	$ 15,000
Total (CBM)	**$ 2,737,000**	**$ 287,000**	**$ 367,000**
Total (CTM)	**$ 3,215,000**	**$ 338,000**	**$ 433,000**

Table S6: ZLD case operating costs breakdown.

	Typical Range	Value Used	Cost ($·yr^{-1})
Direct Manufacturing Cost			
Raw Materials	-	1	$ 4,732,000
Solid Waste Disposal	-	1	$ 1,919,000
Utilities	-	1	$ 3,077,000
Operating Labor	-	1	$ 303,000
Direct Supervisory and Clerical Labor	(0.1-0.25)COL	0.1	$ 30,000
Maintenance and repairs	(0.02-0.1)FCI	0.1	$ 307,000
Operating Supplies	(0.1-0.2)Maintenance	0.2	$ 61,000
Laboratory Charges	(0.1-0.2)COL	0	$ 0
Patents and Royalties	(0-0.06)COM	0	$ 0
Fixed Manufacturing Costs			
Depreciation	0.1FCI	0	$ 0
Local Taxes and Insurance	(0.014-0.05)FCI	0.032	$ 98,000

Table S6 Continued

Plant Overhead Costs	(0.5-0.7)*(COL+DSCL+MR)	0.5	$ 320,000
General Manufacturing Costs			
Administration costs	0.15*(COL+DSCL+MR)	0.15	$ 96,000
Distribution and selling costs	(0.02-0.2)COM	0.11	$ 1,353,000
Research and Development	0.05COM	0	$ 0
Total Operating Costs			**$ 12,298,000**

Table S7: Brine concentration case operating costs breakdown.

	Typical Range	Value Used	Cost ($\$\cdot yr^{-1}$)
Direct Manufacturing Cost			
Raw Materials	-	1	$ 1,384,000
Solid Waste Disposal	-	1	$ 49,000
Utilities	-	1	$ 3,254,000
Operating Labor	-	1	$ 303,000
Direct Supervisory and Clerical Labor	(0.1-0.25)COL	0.1	$ 30,000
Maintenance and repairs	(0.02-0.1)FCI	0.1	$ 321,000
Operating Supplies	(0.1-0.2)Maintenance	0.2	$ 64,000
Laboratory Charges	(0.1-0.2)COL	0	$ 0
Patents and Royalties	(0-0.06)COM	0	$ 0
Fixed Manufacturing Costs			
Depreciation	0.1FCI	0	$ 0
Local Taxes and Insurance	(0.014-0.05)FCI	0.032	$ 103,000
Plant Overhead Costs	(0.5-0.7)*(COL+DSCL+MR)	0.5	$ 328,000
General Manufacturing Costs			
Administration costs	0.15*(COL+DSCL+MR)	0.15	$ 98,000
Distribution and selling costs	(0.02-0.2)COM	0.11	$ 734,000
Research and Development	0.05COM	0	$ 0
Total Operating Costs			**$ 6,669,000**

APPENDIX C. FIGURES OF ASPEN SIMULATION

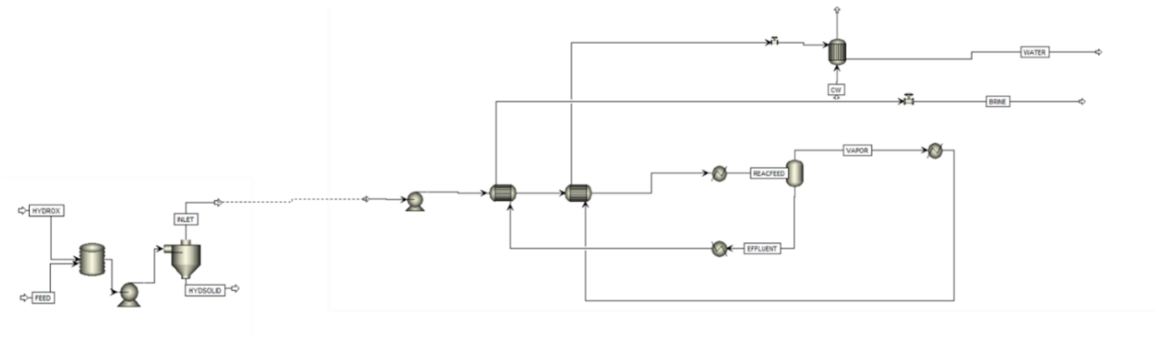

Figure S1: Brine concentration case Aspen Simulation.

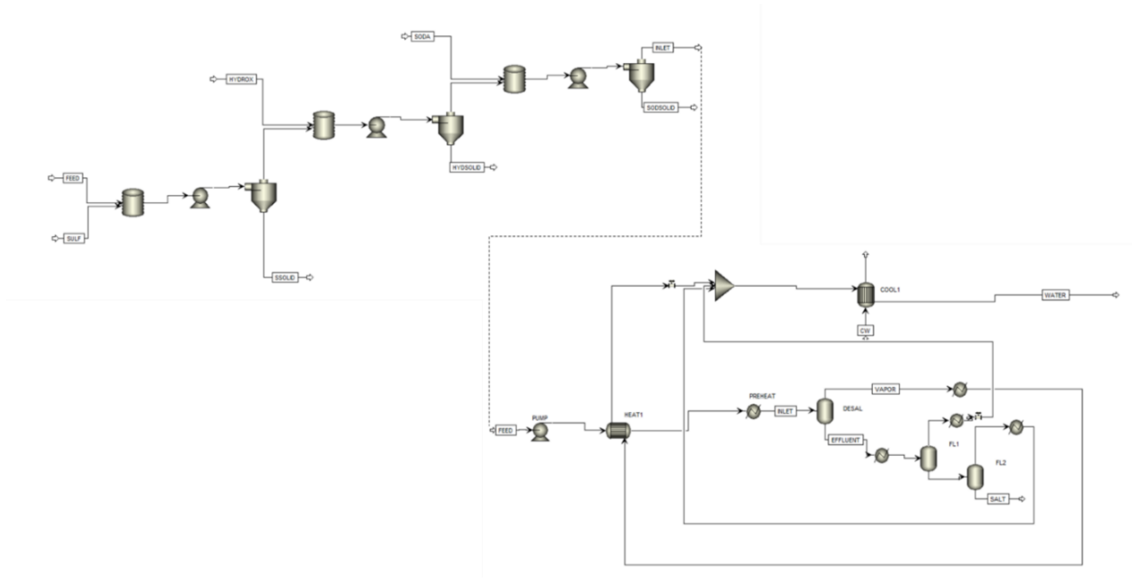

Figure S2: ZLD case Aspen Simulation.

APPENDIX D: LISTING OF PERTINENT STREAMS

D.1. Chemical precipitation

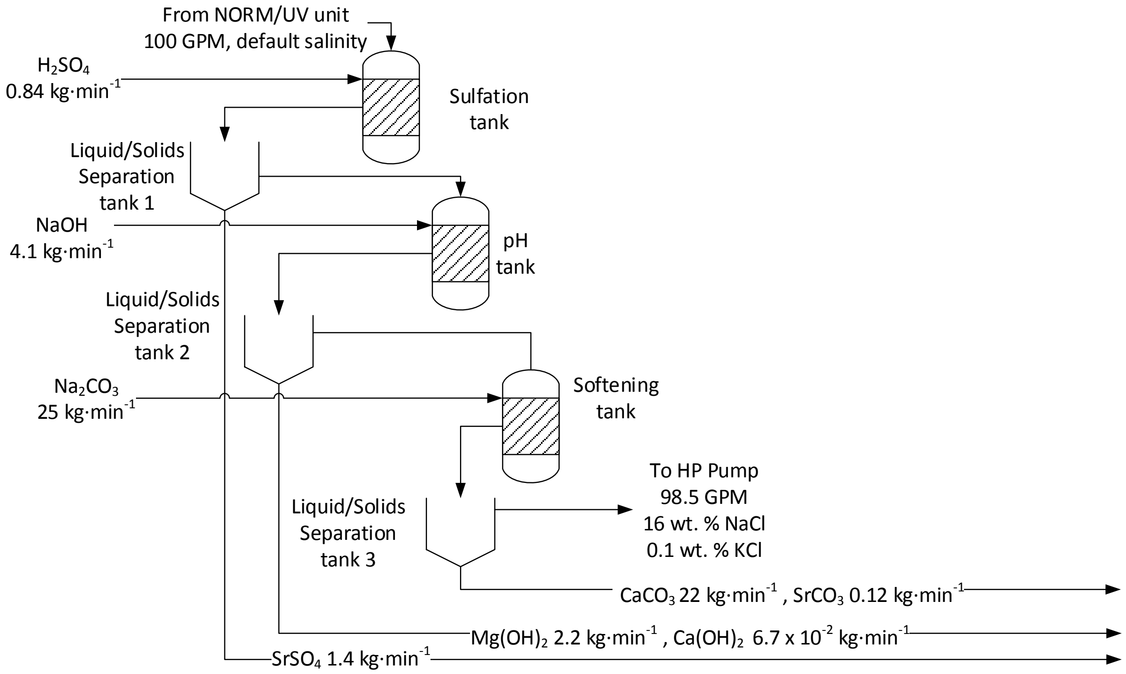

Figure S3: ZLD case precipitation unit material balances.

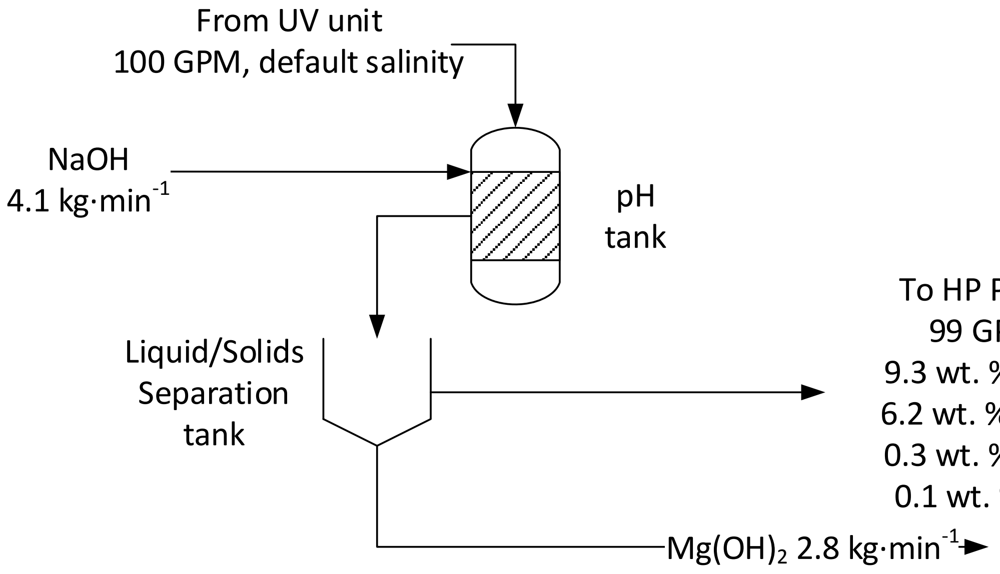

Figure S4: Brine concentration case precipitation unit material balances.

D.2 SCWD system and associated equipment

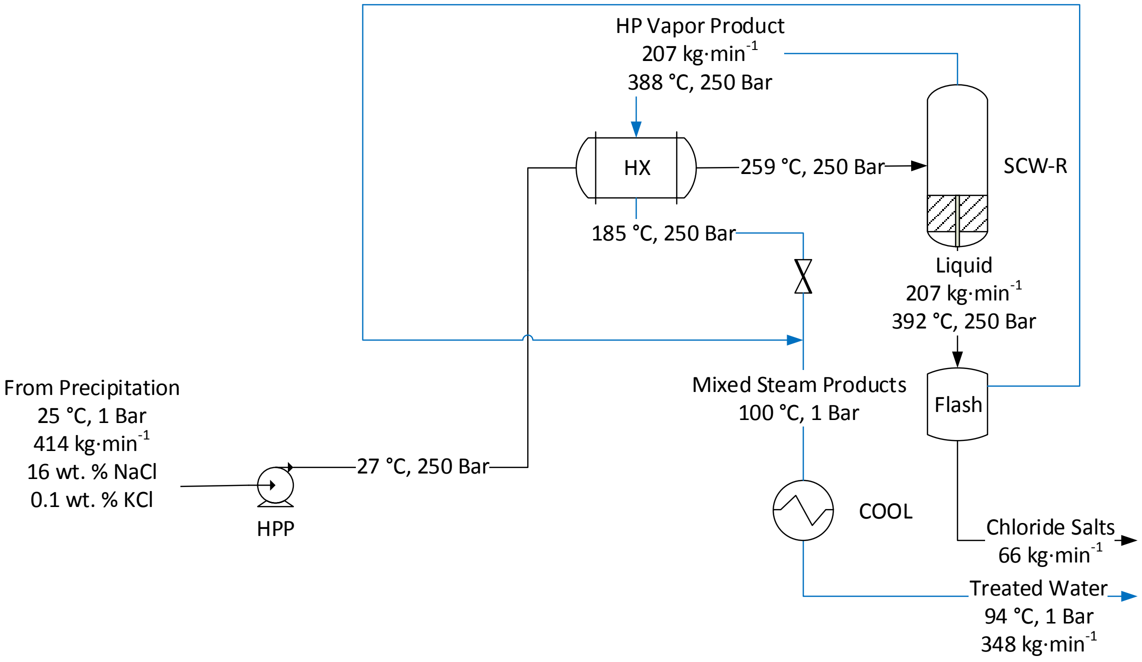

Figure S5: ZLD case high pressure/temperature stream material balances.

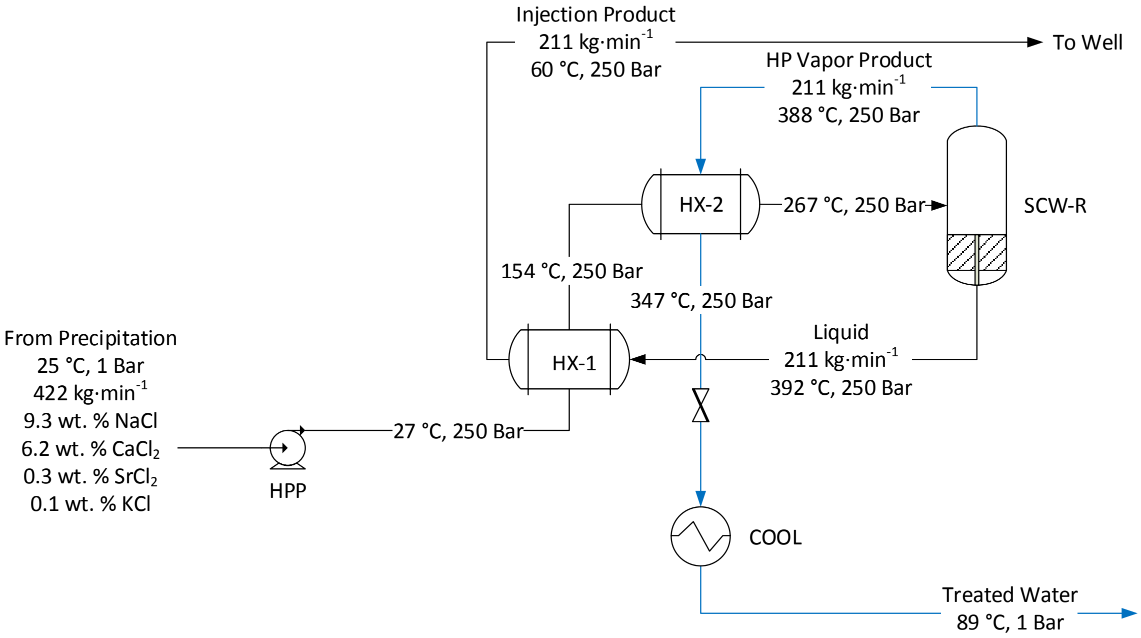

Figure S6: Brine concentration case high pressure/temperature stream material balances.

APPENDIX E: COST BREAKDOWNS BY SALINITY AND PRESSURE

The following tables are meant to demonstrate the shifts in weight for capital, utilities, raw materials, disposal, and labor dependent on the shifts in salinity and pressure for the SCWD system. These are compared to the base case which is also shown in Figure 9.

Table S8: Percentage breakdowns for each cost factor for the ZLD case by salinity and by pressure. The base case numbers are also featured in Figure 9.

	Optimum Recovery Ratio						
		By Salinity, Default Pressure				By Pressure, Default Salinity	
	Base Case	75 g·L^{-1}	105 g·L^{-1}	223 g·L^{-1}	270 g·L^{-1}	230 Bar	280 Bar
Total Capital Cost	**4.0%**	7.6%	6.3%	3.7%	3.2%	4.4%	4.2%
Cost of Labor	**2.9%**	5.1%	4.3%	2.5%	2.1%	2.9%	3.0%
Cost of Raw Materials	**45.3%**	34.2%	39.8%	49.1%	50.8%	44.9%	47.4%
Cost of Solids Disposal	**18.4%**	15.2%	16.9%	19.6%	20.1%	18.2%	19.2%
Cost of Utilities	**29.5%**	37.8%	32.7%	25.1%	23.7%	29.7%	26.2%

Table S9: Percentage breakdowns for each cost factor for the brine concentration case by salinity and by pressure. The base case numbers are also featured in Figure 9.

	Optimum Recovery Ratio						
		By Salinity, Default Pressure				By Pressure, Default Salinity	
	Base Case	75 g·L^{-1}	105 g·L^{-1}	223 g·L^{-1}	270 g·L^{-1}	230 Bar	280 Bar
Total Capital Cost	**6.9%**	9.0%	7.6%	6.1%	5.7%	6.8%	6.8%
Cost of Labor	**4.9%**	6.7%	6.2%	4.3%	3.8%	4.5%	5.1%
Cost of Raw Materials	**22.1%**	13.0%	16.8%	24.7%	26.8%	20.7%	23.3%
Cost of Solids Disposal	**0.8%**	0.5%	0.6%	0.9%	1.0%	0.7%	0.8%
Cost of Utilities	**52.0%**	60.9%	59.3%	52.5%	50.0%	54.8%	53.1%
Cost of Liquid Disposal	**13.3%**	9.9%	9.5%	11.5%	12.7%	12.4%	10.9%

APPENDIX F: ERROR PROPAGATION FOR CALORIMETRIC UNCERTAINTY CALCULATIONS

In the interest of furnishing accurate and applicable thermodynamic data for brines of varying salinity, it is crucial to accurately assess the limits of detection and overall uncertainty involved in calculating the specific heats for these brines. The master equation is rather simple for the furnishing of this data:

$$Q = \dot{m} C_P \Delta T$$

Where Q is the net heat input to the calorimeter in Watts, $\dot{m}$ is the mass flow rate through the calorimeter in g/s, C_P is the specific heat (averaged between the temperature measurements for a given temperature) in J/g*K and ΔT is the temperature difference in K.

Or, when rearranging for C_P:

$$C_P = \frac{Q}{\dot{m}\Delta T}$$

Thus, for a series of C_P measurements, the variance involved in calculating Cp (foregoing any systematic bias) can be calculated one of two ways:

$$\sigma_{C_P}^2 = \sigma_{C_P,avg}^2, \sigma_{C_P,implicit}^2$$

Expanding these two terms for clarity produces:

$$\sigma_{C_P,avg}^2 = \frac{\sum_{i=1}^{N}\left(C_{p,i} - \overline{C_p}\right)^2}{N}$$

$$\sigma_{C_p,implicit}^2 = \overline{C_p}^2 * \left(\left(\frac{\sigma_Q}{Q}\right)^2 + \left(\frac{\sigma_{\dot{m}}}{\dot{m}}\right)^2 + \left(\frac{\sigma_{\Delta T}}{\Delta T}\right)^2\right)$$

Where $\sigma^2_{C_P}$ is the variance associated with the specific heat, $\sigma^2_{C_{P,avg}}$ is the variance calculated from an individual specific heat data set, $\sigma^2_{C_{P,implicit}}$ is the variance associated with the variables used to calculate C_P, $\overline{C_p}$ is the average specific heat calculated for an individual data set, and σ_Q, $\sigma_{\dot{m}}$ and $\sigma_{\Delta T}$ are the independent standard deviations associated with Q, $\dot{m}$ and ΔT.

In this manner, the variances are compared and the larger of the two is used as the specific heat variance. This is a pessimistic but cautious calculation of the estimated uncertainty involved in calculating the specific heat in flow calorimetry. The deviations of the individual measurements are compared to the deviation in the specific heat measurement itself. Each of these deviations are discussed in greater detail in the following sections, where appropriate literature is used to infer the proper calculation of each value.

Deviation in heat input (Q)

The net heat input, Q, is a summation of the heat supplied to the calorimeter and the heat lost through the calorimeter:

$$Q = Q_{in} - Q_{loss}$$

Accurately determining the heat lost for a fluid whose calorimetric properties are inherently unknown is non-trivial; the correction for heat losses is the subject with quite a bit of contention within literature. One approach from White [113] is to use a high density solution of sodium chloride and water as a reference fluid to calculate a correction factor, *f*, for the unknown fluid. This method is contested by Rogers and Duffy

[114] in favor of a method which calculates this correction factor in terms of the temperature difference, flow rate and specific heat of the fluid for a single heater:

$$f = \left(\frac{a}{(b + \Delta T)Fc_P}\right) + 1$$

For a constant temperature difference, the calibration was thus completed by simply varying the flow rate. Investigations into simple salt solutions were spurred in the eighties by these differing methods which produced varying results [37], [113], [114]and were continued by Hnedkovsky [74] in the early 2000's; the higher temperature calorimeter used by this author employed a correction by varying the power and flow rate to produce the same temperature difference at varying flow rates:

$$f = \frac{P_r * \Delta F}{\Delta P_r * F_r}$$

The advantage of this method is that the specific heat of the reference fluid does not need to be known in order to estimate the heat losses from this calorimeter. The values calculated from this calorimeter for sodium chloride were compared to the global fit provided by Archer [24] with some larger discrepancies at higher temperatures in spite of the very small uncertainty predicted by this method.

For the calorimeter described in this paper, a series of trials were completed with de-ionized water provided via reverse osmosis (RO) filtration from a Millipore Q-Pod in order to assess the dependence of the heat loss on temperature, pressure, density of the working fluid within the calorimeter, and heater power. While some weak trends were found, none were found to be statistically significant by this method; this calorimeter, while more rugged, does not possess the instruments necessary to provide the uncertainty claimed by the authors of the former methods [74], [114]– thus, a lumped parameter with an expected uncertainty is used for Q_{loss} in this paper. However, repeated corrosion issues have necessitated some repairs to the calorimeter apparatus – for the calcium chloride data that is tabulated in Chapter 4, each run was first calibrated with a separate trial with DI water. The NIST enthalpies [102] were used at each pressure and temperature split in order to generate a heat loss value for each run which is simply:

$$Q_{loss} = Q_{in} - \dot{m}(h_{out} - h_{in})$$

It is believed that the heat losses will still shift dependent on the solution being considered (salt solutions as compared to pure water); however, the lack of a trend in (ρ, T, P) makes this difficult to consider. To counteract this, each specific heat shown is the average of duplicate runs: one run is done with enough power to create a positive temperature differential, i.e. $Q_{in} > Q_{loss}$, and another is done with a negative temperature differential of the same approximate magnitude, i.e. $Q_{in} < Q_{loss}$.

Deviation in mass flow rate (ṁ)

In terms of the set variables, the mass flow rate is calculated using the following:

$$\dot{m} = \rho F$$

Where ρ is the room temperature mass density of the fluid and F is the volumetric flow rate charged into the calorimeter using the HPLC pump. The independent error associated with each of these values is as follows:

$$\sigma_\rho^2 = \sigma_{solution}^2$$

$$\sigma_F = \sqrt{{\sigma_{F,avg}}^2 + {\delta_{scale}}^2}$$

Where $\sigma_{solution}^2$ is the variances associated with the production of the solution (very small, three to four errors of magnitude lower than other errors), and δ_{scale} is the error associated with the scale used to take liquid measurements. The flow rate is calculated as a rolling average with scale data; this produces far more accurate mass flow measurements than using the HPLC pump set point as is. With the exception of the noise in flow rate, all of these errors are much smaller than the error associated with Q or ΔT; this error is thus considered simply as the flow rate uncertainty for the calculation of C_P.

Deviation in temperature difference (ΔT)

The implicit and independent deviation associated with the temperature differential is simply a calculation involving the limit of detection for the probes employed within the calorimeter. The calorimeter utilizes SLE grade Type E thermocouples provided by Omega Engineering which were independently calibrated using a five-point calibration at temperatures of interest (250-450 °C) with an uncertainty of 0.088 °C or K. This error is directly used in the calculation of the deviation in temperature difference in the following formula:

$$\sigma_{\Delta T} = \sqrt{\sigma_{\Delta T,avg}{}^2 + \sigma_{T1}^2 + \sigma_{T2}^2} = \sqrt{\sigma_{\Delta T,avg}{}^2 + \left(\delta_T * \sqrt{2}\right)^2}$$

Here, $\sigma_{\Delta T,avg}{}^2$ is the variance associated with the average of the temperature difference measurement, and σ_{T1}^2 and σ_{T2}^2 are the variances associated with the temperature probes T_1 and T_2 – this is equivalent to the probe uncertainty provided via calibration δ_T multiplied by the square root of 2. This uncertainty is used directly in the above equation to calculate a relative uncertainty in ΔT; this number should not be overly large for temperature differences between 2 and 4 K.

APPENDIX G: CALIBRATION DATA FOR THE CALORIMETRIC APPARATUS

Initial tests were conducted within the NaCl-H_2O system in order to ensure the accuracy of the calorimetric apparatus. As with the $CaCl_2$-H_2O results shown in Figure 26, the system was first calibrated with DI water using reference pure water enthalpies available from the NIST database [102]. The resulting NaCl-H_2O results at 10 and 15 wt. % were then compared with the specific heat correlation available in Driesner [22]. The initial results at temperatures near and above the critical point of pure water were substantially noisier than the lower temperature counterparts, which directed the results published in this work at temperatures at or below 350 °C.

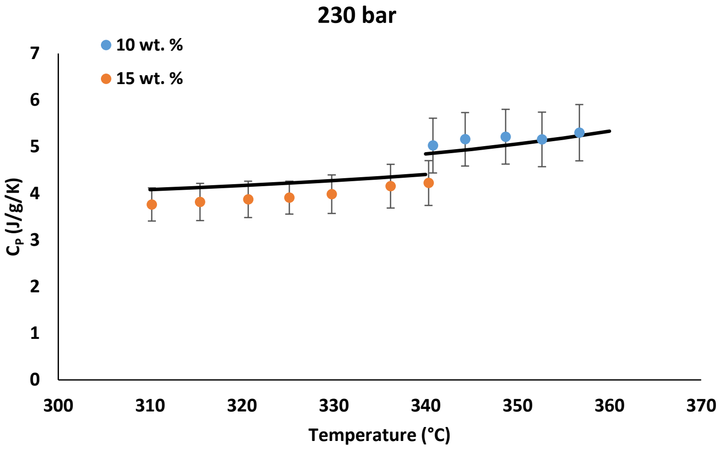

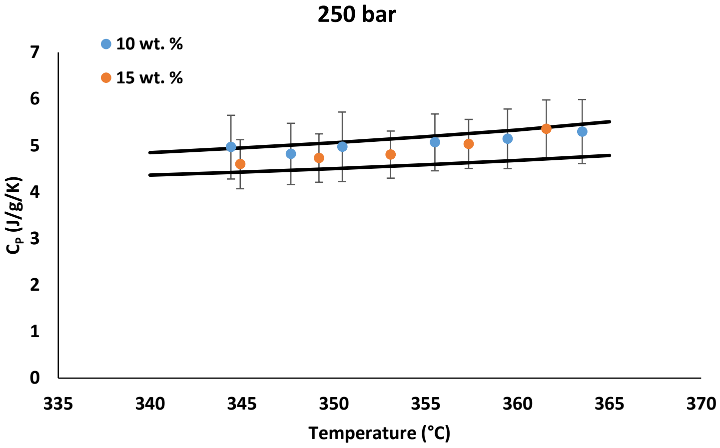

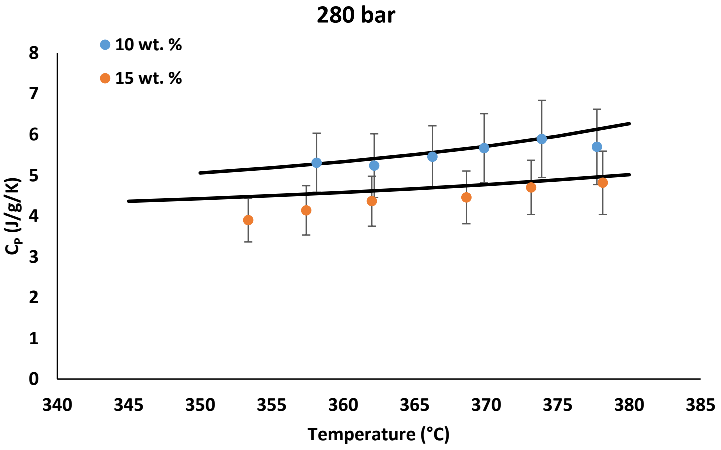

Figure S7: NaCl-H_2O results compared with the specific heat correlation in Driesner [22]. The weight percents shown here are in NaCl.